Liquid-Vapor Phase Transition: Thermomechanical Theory, Entropy Stable Numerical Formulation, and Boiling Simulations

Ju Liu [a,*], Chad M. Landis [a,b], Hector Gomez [c], Thomas J.R. Hughes [a,b]

[a] *Institute for Computational Engineering and Sciences, The University of Texas at Austin,*
201 East 24th Street, 1 University Station C0200, Austin, TX 78712, USA

[b] *Aerospace Engineering and Engineering Mechanics, The University of Texas at Austin,*
210 East 24th Street, 1 University Station C0600, Austin, TX 78712, USA

[c] *Departamento de Métodos Matemáticos, Universidade da Coruña,*
Campus de A Coruña, 15071, A Coruña, Spain.

[*] Corresponding author. *E-mail address:* jliu@ices.utexas.edu

Abstract

We develop a new continuum mechanics modeling framework for liquid-vapor flows, with particular focus on the van der Waals fluid. By invoking microforce theory, the Coleman-Noll procedure is generalized to derive consistent constitutive relations in the presence of non-local effects. A new thermodynamically consistent algorithm for the van der Waals model is designed, using functional entropy variables and a new temporal scheme employing a family of new quadrature rules. We show that the resulting fully discrete scheme is unconditionally stable in entropy and second-order time-accurate. Isogeometric analysis is utilized for spatial discretization. The analytical properties of the formulation are corroborated by benchmark problems. Three sets of application problems are simulated to demonstrate the capability of the model and the algorithm. Our methodology provides a particularly useful predictive tool for boiling flows.

Keywords: Phase-field model, Diffuse interface, Microforce, Coleman-Noll approach, Van der Waals fluid, Non-convex flux, entropy variables, Time integration, Isogeometric analysis, Phase transition, Evaporation, Condensation, Boiling

1 Introduction

1.1 Phase transition and classical modeling techniques

Liquid-vapor two-phase flows are ubiquitous in the natural world as well as in industry. Liquid-vapor phase transitions involve a sharp change of the fluid density. Typical environmental changes include pressure variations and thermal variations. For instance, the local pressure near a rotating propeller may drop below the boiling pressure, and vapor bubbles may generate near blades [40]. This is the phenomenon of cavitation and it is still a limiting factor for ship propeller design. Phase transitions induced by temperature variations can be observed in daily life as boiling, evaporation, and condensation. In industry, liquid-vapor phase transitions take place in steam generators, heat exchangers, and various pipelines. The accompanying thermal effects make multiphase flow a widely-used mechanism for energy transfer.

To date, many modeling techniques have been designed to simulate multiphase flows. Most of them fall into the categories of interface-tracking methods or interface-capturing methods. Interface-tracking methods resolve the interface by aligning the computational mesh along the interface and by updating the mesh accordingly with the fluid flow. This approach gives a sharp and accurate representation of the interface. However, it requires constant re-meshing of the computational domain, and it is typically intractable for topological transitions. Three-dimensional problems with severe topological transitions are notoriously difficult to solve with interface-tracking methods. Interface-capturing methods use additional unknowns to implicitly represent the interface. The interface is typically immersed in the computational domain. Consequently, the interface representation is less accurate than that of the interface-tracking methods. However, the interface-capturing methods enjoy several advantages: they are relatively easy to implement, the mesh updating burden is reduced, and topological transitions are easily handled. Existing instantiations of the interface-capturing methods include the volume-of-fluid (VOF) method [31] and the level-set method [54]. Both methods have been utilized in commercial codes and remain popular subjects in the literature. However, they are not without shortcomings. The VOF method uses a post-processing procedure to construct the interface, which inevitably introduces errors. In level-set methods, the level-set function needs to be reinitialized every few steps. The reinitialization procedure is rather ad hoc and does not maintain the conservation structure of the governing equations.

1.2 Phase-field models

To address the aforementioned modeling difficulties, phase-field models were proposed as an alternative interface-capturing method. The phase-field method uses an order parameter to distinguish different phases. Phase-field models postulate that the interface has finite width and material properties transit across the interfacial region smoothly but sharply. Based on these postulates, van der Waals developed his Nobel Prize-winning theory to calculate the capillarity for liquid-vapor interfaces. Later, Korteweg developed the so-called Korteweg stress formulation and coupled the van der Waals theory with hydrodynamics. The fluid equations based on the van der Waals theory are called the Navier-Stokes-Korteweg equations. This theory is characterized by a non-convex free energy, supplemented with a non-local density gradient term. This non-local term regularizes the singularity introduced by the non-convex free energy function. The non-local term represents the surface energy. In contemporary continuum mechanics, this model falls into the category of the grade-N fluid model [67]. In 1985, Dunn and Serrin studied the thermodynamic consistency of the Navier-Stokes-Korteweg equations and found that for the model to be consistent with the second law, a new term had to be added to the energy equation [17]. They called this term the "interstitial working flux".

Parallel to the development of the Navier-Stokes-Korteweg equations, another branch of phase-field models has been developed focusing on multicomponent systems. The original idea emanates from the work of Cahn and Hilliard [9], in which a fourth-order nonlinear diffusion equation is proposed to mimic the behavior of a two-component mixture. Recently, the Cahn-Hilliard type models have been generalized to more complicated multicomponent systems, such as spinodal decomposition [43], tumor growth [70], fingering effect in porous medium [23], topology optimization [13], etc. Significant progress was made by Gurtin and his collaborators in providing a rational mechanics framework for the Cahn-Hilliard type models [27]. In Gurtin's theory, microforces were introduced to account for the phase dynamics. Later, this theory was applied to construct a plasticity theory of single crystals [28], fracture models [72], alloy models [46], and ferroelectric models [66], to list a few. In Section 2, this theory is adopted as a means to derive constitutive relations for the van der Waals fluid material. Interestingly, the "interstitial working flux" appears naturally in this derivation as the power expenditure of the microstress. This, in part, justifies the work of Dunn and Serrin within the rational thermomechanics framework of [11].

Traditional interface-tracking and interface-capturing methods are designed to follow existing interfaces. When dealing with phase transition phenomena, those methods become intractable. One may need to introduce artificial procedures and empirical assumptions [65] to mimic such phenomena. In contrast, the solid mathematical and thermodynamic foundations of phase-field models allow them to describe these complicated phenomena without resorting to modeling tricks. In this work this advantage will be demonstrated by a suite of boiling simulations. Boiling is regarded to be highly difficult for numerical simulations. Traditional models require empirical knowledge, such as the bubble release rate and bubble departure radius, to describe the boiling process. In this work, two- and three-dimensional boiling simulations are carried out using the van der Waals fluid model. Owing to the thermodynamically consistent nature, the dependency on empirical knowledge is significantly reduced, and there are no ad hoc procedures involved. Our approach provides a unified predictive capability for both nucleate and film boiling

Despite their success, phase-field models face several challenges. The entropy function for phase-field models are always non-convex, which creates difficulty for both mathematical analysis and numerical simulation. Phase-field models usually have a high-order differential term, which necessitates novel numerical discretization techniques, and the interface width for real materials is typically a few nanometers. Therefore, adaptive refinement near the interfacial region is required for real-world simulations.

1.3 Numerical analysis

In the numerical analysis of nonlinear problems, a central issue is stability. One relevant example for the current work is the study of entropy-stable schemes for gas dynamics. It was revealed that the weak form of the compressible Navier-Stokes equations will automatically satisfy the Clausius-Duhem inequality by utilizing entropy variables [34]. In the late 1980s, the space-time formulation was applied to the entropy-variables formulation to construct a fully discrete entropy-stable scheme [63]. Thereafter, the entropy-variables formulation offered a foundation for computing compressible flows. Interested readers are referred to [35] for a detailed review. However, it needs to be pointed out that the stability of this entropy-variables formulation is all contingent upon the convexity of the entropy function. For phase-field problems, the non-convexity of the entropy function precludes the possibility of directly applying this methodology. To overcome the challenges posed by the non-convexity of the entropy, first, the definition of the entropy variables is generalized to the functional setting [44]. Employing functional entropy variables, we derive an alternative statement of the original Navier-Stokes-Korteweg equations. The weighted residual formulation based on this alternative statement leads to a provably entropy-stable semi-discrete formulation. Second, to develop a stable temporal scheme, we adopt the methodology based on special quadrature rules [24, 42, 44]. The new difficulty comes from the discretization of the energy time derivative, since the isothermal Navier-Stokes-Korteweg equations have been well handled, as described in [44]. A new "jump" operator (i.e., discrete time-derivative operator) is devised for the total energy. It is shown that this operator represents a third-order perturbation to the classical "jump" operator. By using perturbed trapezoidal rules repeatedly, it is proven that the temporal approximation based on the new "jump" operator dissipates entropy, and the requirement of convexity is released. It is anticipated that this new temporal discretization technology is applicable to more general problems.

Non-Uniform Rational B-Splines (NURBS), in the setting of isogeometric analysis, are utilized to provide a representation of the geometry as well as an approximation for the spatial discretization [33]. Isogeometric analysis has been shown to enjoy several desirable numerical properties: (1) it retains an exact representation of the geometry; (2) it possesses a unique k-refinement technology, which allows one to generate higher-continuity basis functions without proliferation of degrees of freedom; (3) it exhibits superior robustness [14, 41] and accuracy [18] properties compared with traditional finite elements. The above attributes make isogeometric analysis a particularly effective approach in the approximation of phase-field problems [22, 25]. The NURBS-based initial instantiation of isogeometric analysis has been widely used in both design and analysis [12]. Recent advances of isogeometric analysis include T-splines, divergence-conforming B-splines, and isogeometric collocation methods. T-splines allow one to create complicated engineering designs in a single watertight geometric format [4] and enable local refinement [60]. For incompressible flows, divergence-conforming B-splines guarantee point-wise divergence-free velocity solutions [19, 20, 21]. It is anticipated that such technology may be applied to compressible flow simulations with the hope of attaining well-behaved discretization at the incompressible limit. Isogeometric collocation methods are shown to be an efficient alternative to isogeometric Galerkin methods [58], which offers a potentially powerful alternative for phase-field simulations [26, 56].

1.4 Structure and content of the paper

The body of this work is organized as follows. In Section 2, based on the Gurtin microforce theory, a unified thermomechanical modeling framework is derived. The Navier-Stokes-Korteweg equations, including the interstitial working flux term, are derived within this framework by choosing an appropriate Helmholtz free energy functional. The thermodynamic properties of this model are discussed. In Section 3, a provably entropy-stable, second-order time accurate numerical scheme is designed and analyzed for the Navier-Stokes-Korteweg equations. Our approach is based fundamentally on the concept of functional entropy variables and utilizes newly developed concepts for the derivation of time stepping algorithms appropriate for problems involving non-convex potentials. In Section 4, benchmark problems are studied to verify the theoretical estimates. In Section 5, a suite of application examples, including evaporation, condensation, bubble motion under a temperature gradient, and boiling flows, are numerically investigated using the model and algorithm developed. Conclusions and future research directions are presented in Section 6.

2 The Navier-Stokes-Korteweg equations

2.1 Balance laws

The continuum theory setting is the Euclidean space $\mathbb{R}^3$, with fixed orthonormal basis vectors $\mathbf{e}_i$, $i = 1, 2, 3$. The body under consideration occupies a region $\mathcal{B} \subset \mathbb{R}^3$, which is referred to as the reference configuration. The material point in $\mathcal{B}$ is labeled by $\mathbf{X} = (X_1, X_2, X_3)^T$. The motion that the continuum body undergoes is denoted as $\mathcal{X} : \mathcal{B} \times [0, \infty) \to \mathbb{R}^3$. The image of $\mathcal{B}$ by $\mathcal{X}$ at time t is denoted as $\mathcal{B}_t$, which is referred to as the current configuration. The spatial position of material points $\mathbf{X}$ at time t is given by

$$\mathbf{x} = \mathcal{X}\left(\mathbf{X}, t\right),$$

where $\mathbf{x} = (x_1, x_2, x_3)^T$. We postulate that the map $\mathcal{X}$ is differentiable, one-to-one, and orientation preserving for each time $t \geq 0$. Consider an arbitrary open set Ω of $\mathcal{B}$; its image at time t is denoted as $\Omega_t = \mathcal{X}\left(\Omega, t\right)$. The boundary $\partial\Omega_t$ is oriented with a unit outward normal vector $\mathbf{n}(\mathbf{x})$. We assume that there exists a density field $\rho(\mathbf{x}, t)$ and a velocity field $\mathbf{u}\left(\mathbf{x}, t\right)$ in the current configuration. The spatial velocity field is defined as

$$\mathbf{u}\left(\mathbf{x}, t\right) = \frac{\partial}{\partial t}\mathcal{X}(\mathbf{X}, t) \quad \text{where} \quad \mathbf{x} = \mathcal{X}(\mathbf{X}, t).$$

In the following, we understand D/Dt to be the material time derivative, i.e.,

$$\frac{D}{Dt}\left(\cdot\right) := \frac{\partial}{\partial t}\left(\cdot\right) + \mathbf{u} \cdot \nabla\left(\cdot\right),$$

where ∇ is the spatial gradient operator. We have the following balance laws that govern the behavior of the body.

- **Conservation of Mass**

$$\frac{d}{dt}\int_{\Omega_t} \rho(\mathbf{x}, t) dV_{\mathbf{x}} = 0. \tag{1}$$

- **Balance of Linear Momentum**

$$\frac{d}{dt}\int_{\Omega_t}\rho(\mathbf{x},t)\mathbf{u}(\mathbf{x},t)dV_{\mathbf{x}}=\int_{\partial\Omega_t}\mathbf{t}(\mathbf{x},t)dA_{\mathbf{x}}+\int_{\Omega_t}\rho\mathbf{b}(\mathbf{x},t)dV_{\mathbf{x}}. \tag{2}$$

Here the traction field is given by $\mathbf{t}(\mathbf{x},t)=\mathbf{T}(\mathbf{x},t)\mathbf{n}(\mathbf{x})$, where $\mathbf{T}(\mathbf{x},t)$ is the Cauchy stress tensor; $\mathbf{b}(\mathbf{x},t)$ is the external body force per unit mass.

- **Balance of Angular Momentum**

$$\frac{d}{dt}\int_{\Omega_t}\mathbf{x}\times\rho(\mathbf{x},t)\mathbf{u}(\mathbf{x},t)dV_{\mathbf{x}}=\int_{\partial\Omega_t}\mathbf{x}\times\mathbf{t}(\mathbf{x},t)dA_{\mathbf{x}}+\int_{\Omega_t}\mathbf{x}\times\mathbf{b}(\mathbf{x},t)dV_{\mathbf{x}}. \tag{3}$$

In our work the central modeling subject is the liquid-vapor phase transition. The phase-field order parameter for the change of the state of matter is chosen as the density ρ. Following the ideas of Gurtin [27], we assume that there exists a set of forces that accounts for the kinematics of phase transitions. These forces are called microforces primarily because they are involved with the local transformation of the material, rather than the macroscopic movements. We assume that the kinematics of ρ are associated with the following forces:

$\boldsymbol{\xi}$, the microstress,
χ, the surface microforce,
φ, the internal microforce,
l, the external microforce.

This set of microforces is balanced as stated in the following equation.

- **Balance of Microforce Associated with Density Phase Transition**

$$\int_{\partial\Omega_t}\chi(\mathbf{x},t)dA_{\mathbf{x}}+\int_{\Omega_t}\varphi dV_{\mathbf{x}}+\int_{\Omega_t}l dV_{\mathbf{x}}=0. \tag{4}$$

The surface microforce is given by $\chi(\mathbf{x},t)=\boldsymbol{\xi}(\mathbf{x},t)\cdot\mathbf{n}(\mathbf{x})$.

Remark 1. *The notion of microforce was initially introduced to generalized the Cahn-Hilliard equation [27]. For a comprehensive review, interested readers are referred to [29].*

- **Conservation of Energy**

$$\frac{d}{dt}\int_{\Omega_t}\rho(\mathbf{x},t)E(\mathbf{x},t)dV_{\mathbf{x}} = \int_{\partial\Omega_t}\left(\mathbf{T}(\mathbf{x},t)\mathbf{u}(\mathbf{x},t) + \frac{D}{Dt}\rho(\mathbf{x},t)\boldsymbol{\xi}(\mathbf{x},t) - \mathbf{q}\right)\cdot\mathbf{n}(\mathbf{x})dA_{\mathbf{x}} + \int_{\Omega_t}\mathbf{b}(\mathbf{x},t)\cdot\mathbf{u}(\mathbf{x},t) + l(\mathbf{x},t)\frac{D}{Dt}\rho(\mathbf{x},t) + \rho(\mathbf{x},t)r(\mathbf{x},t)dV_{\mathbf{x}}. \tag{5}$$

In equation (5), the following notations are introduced:

$E(\mathbf{x},t) = \iota(\mathbf{x},t) + \frac{1}{2}|\mathbf{u}(\mathbf{x},t)|^2$, the total energy density per unit mass,
$\iota(\mathbf{x},t)$, the internal energy density per unit mass,
$\mathbf{q}(\mathbf{x},t)$, the heat flux,
$r(\mathbf{x},t)$, the heat source per unit mass.

Besides the traditional working terms of the macroscopic forces and the macroscopic sources, there are non-classical terms contributing to the change of the total energy. These terms are the power expenditures of the microstress $\boldsymbol{\xi}$ and the external microforce l:

$$\int_{\partial\Omega_t}\frac{D}{Dt}\rho(\mathbf{x},t)\boldsymbol{\xi}(\mathbf{x},t)\cdot\mathbf{n}(\mathbf{x})dA_{\mathbf{x}}, \quad \int_{\Omega_t}l(\mathbf{x},t)\frac{D}{Dt}\rho(\mathbf{x},t)dV_{\mathbf{x}}.$$

The internal microforce does not contribute to the energy change. See [27] for a conceptual explanation.

- **Second Law of Thermodynamics**

$$\int_{\Omega_t}\mathcal{D}(\mathbf{x},t)dV_{\mathbf{x}} := \frac{d}{dt}\int_{\Omega_t}\rho(\mathbf{x},t)s(\mathbf{x},t)dV_{\mathbf{x}} + \int_{\partial\Omega_t}\frac{\mathbf{q}(\mathbf{x},t)\cdot\mathbf{n}(\mathbf{x})}{\theta(\mathbf{x},t)}dA_{\mathbf{x}} - \int_{\Omega_t}\frac{\rho(\mathbf{x},t)r(\mathbf{x},t)}{\theta(\mathbf{x},t)}dV_{\mathbf{x}} \geq 0. \tag{6}$$

Here $\mathcal{D}(\mathbf{x},t)$ denotes the total dissipation, $s(\mathbf{x},t)$ denotes the entropy density, and $\theta(\mathbf{x},t)$ is the absolute temperature. This inequality is the second law of thermodynamics, or Clausius-Duhem inequality.

Applying the divergence and the Reynolds' transport theorems, we can obtain the governing equations and the Clausius-Duhem inequality in local forms (omitting the arguments $\mathbf{x}$ and t for simplicity) as

$$\frac{D\rho}{Dt} + \rho\nabla\cdot\mathbf{u} = 0, \tag{7}$$

$$\rho\frac{D\mathbf{u}}{Dt} = \nabla\cdot\mathbf{T} + \rho\mathbf{b}, \tag{8}$$

$$\mathbf{T} = \mathbf{T}^T, \tag{9}$$

$$\nabla \cdot \boldsymbol{\xi} + \varphi + l = 0, \tag{10}$$

$$\rho \frac{DE}{Dt} = \nabla \cdot \left(\mathbf{T}\mathbf{u} + \frac{D\rho}{Dt}\boldsymbol{\xi} - \mathbf{q} \right) + \rho \mathbf{b} \cdot \mathbf{u} + l \frac{D\rho}{Dt} + \rho r, \tag{11}$$

$$\mathcal{D} := \rho \frac{Ds}{Dt} + \nabla \cdot \left(\frac{\mathbf{q}}{\theta} \right) - \frac{\rho r}{\theta} \geq 0. \tag{12}$$

In addition to the governing equations (7)–(12), there is a balance equation for the internal energy ι. The total energy balance equation can be expanded first as

$$\begin{aligned} \rho \frac{D\iota}{Dt} + \rho \mathbf{u} \cdot \frac{D\mathbf{u}}{Dt} =& \nabla \cdot \mathbf{T} \cdot \mathbf{u} + \mathbf{T} : \nabla \mathbf{u} + \nabla \cdot \boldsymbol{\xi} \frac{D\rho}{Dt} + \boldsymbol{\xi} \cdot \nabla \left(\frac{D\rho}{Dt} \right) \\ & - \nabla \cdot \mathbf{q} + \rho \mathbf{b} \cdot \mathbf{u} + l \frac{D\rho}{Dt} + \rho r. \end{aligned} \tag{13}$$

The linear momentum balance equations and the microforce balance equation can be utilized to give the following relations.

$$\rho \mathbf{u} \cdot \frac{D\mathbf{u}}{Dt} = \nabla \cdot \mathbf{T} \cdot \mathbf{u} + \rho \mathbf{b} \cdot \mathbf{u}, \tag{14}$$

$$\nabla \cdot \boldsymbol{\xi} \frac{D\rho}{Dt} + l \frac{D\rho}{Dt} = -\varphi \frac{D\rho}{Dt}. \tag{15}$$

Substituting (14)–(15) into (13), we may obtain a balance equation for the internal energy as follows.

$$\rho \frac{D\iota}{Dt} = \mathbf{T} : \nabla \mathbf{u} - \varphi \frac{D\rho}{Dt} + \boldsymbol{\xi} \cdot \nabla \left(\frac{D\rho}{Dt} \right) - \nabla \cdot \mathbf{q} + \rho r. \tag{16}$$

This equation will be used as a starting point for the derivation of constitutive relations.

2.2 Coleman-Noll type analysis and constitutive relations

To close the model, we still need to provide the constitutive relations for the Cauchy stress, the internal energy density, the entropy density, the heat flux, and the microforces. In this section, we derive the explicit form of the constitutive relations in terms of a thermodynamic potential. In this derivation, the Coleman-Noll argument is applied so that the resulting constitutive relations will be thermodynamically consistent.

2.2.1 Free energy imbalance

The Helmholtz free energy density per unit mass $\Psi(\mathbf{x}, t)$ is defined by

$$\Psi(\mathbf{x}, t) := \iota(\mathbf{x}, t) - \theta(\mathbf{x}, t) s(\mathbf{x}, t).$$

Taking material time derivatives at both sides, we get the relation

$$\frac{D\iota}{Dt} - \theta \frac{Ds}{Dt} = \frac{D\Psi}{Dt} + s \frac{D\theta}{Dt}. \tag{17}$$

Substituting the internal energy balance equation (16) and the second law of thermodynamics (12) into the above relation, we can get an inequality

$$\rho \frac{D\Psi}{Dt} + \rho s \frac{D\theta}{Dt} \leq \mathbf{T} : \nabla \mathbf{u} - \varphi \frac{D\rho}{Dt} + \boldsymbol{\xi} \cdot \nabla \left(\frac{D\rho}{Dt} \right) - \frac{\mathbf{q} \cdot \nabla \theta}{\theta}.$$

Moving the term $\rho s D\theta / Dt$ to the right hand side, we can get a constraint inequality for Ψ as

$$\rho \frac{D\Psi}{Dt} \leq \mathbf{T} : \nabla \mathbf{u} - \varphi \frac{D\rho}{Dt} + \boldsymbol{\xi} \cdot \nabla \left(\frac{D\rho}{Dt} \right) - \frac{\mathbf{q} \cdot \nabla \theta}{\theta} - \rho s \frac{D\theta}{Dt}. \tag{18}$$

The inequality (18) is referred to as the free energy imbalance. It plays an analogous role to (12) in placing restrictions on constitutive relations. In fact, for pure mechanical processes when thermal effects are negligible, the Helmholtz free energy is the thermodynamic potential that characterizes the dissipation behavior of the isothermal system. For an isobaric isothermal process, however, the Gibbs free energy should be chosen as a proper thermodynamic potential [45]. In this work, an isobaric process is not assumed. Hence, the Helmholtz free energy is a valid thermodynamic potential. Before proceeding further, we split the Cauchy stress $\mathbf{T}$ and the velocity gradient $\nabla \mathbf{u}$ into deviatoric and hydrostatic parts.

1. The Cauchy stress $\mathbf{T}$ can be split into deviatoric and hydrostatic parts,

   $$\mathbf{T} = \mathbf{T}^d + \mathbf{T}^h, \tag{19}$$

   where

   $$\mathbf{T}^d = \mathbf{T} - \frac{1}{3} (\mathrm{tr} \mathbf{T}) \mathbf{I}, \tag{20}$$

   $$\mathbf{T}^h = \frac{1}{3} (\mathrm{tr} \mathbf{T}) \mathbf{I}. \tag{21}$$

Here $\mathbf{I}$ is the identity tensor, and $\mathrm{tr}(\cdot)$ is the trace operator.

2. The velocity gradient can be split into three parts,

$$\nabla\mathbf{u} = \mathbf{L}^d + \mathbf{L}^h + \mathbf{W}, \tag{22}$$

wherein

$$\begin{aligned} \mathbf{L}^d &= \frac{1}{2}\left(\nabla\mathbf{u} + \nabla\mathbf{u}^T\right) - \frac{1}{3}\nabla\cdot\mathbf{u}\mathbf{I}, && (23)\\ \mathbf{L}^h &= \frac{1}{3}\nabla\cdot\mathbf{u}\mathbf{I}, && (24)\\ \mathbf{W} &= \frac{1}{2}\left(\nabla\mathbf{u} - \nabla\mathbf{u}^T\right). && (25) \end{aligned}$$

In this split, $\mathbf{L}^d$ and $\mathbf{L}^h$ are the deviatoric and hydrostatic (i.e., dilatational) parts of the rate of strain tensor $\mathbf{L}$; $\mathbf{W}$ is the spin tensor (i.e., vorticity tensor).

Consequently, it is straightforward to make the following observations.

1. According to the mass balance equation (7), we have

$$\nabla\cdot\mathbf{u} = -\frac{D\rho/Dt}{\rho}. \tag{26}$$

2. The gradient of material time derivative $D\rho/Dt$ can be expanded as

$$\nabla\left(\frac{D\rho}{Dt}\right) = \frac{D}{Dt}\left(\nabla\rho\right) + \nabla\mathbf{u}^T\nabla\rho = \frac{D}{Dt}\left(\nabla\rho\right) + \mathbf{L}^d\nabla\rho + \mathbf{W}^T\nabla\rho - \frac{D\rho/Dt}{3\rho}\nabla\rho. \tag{27}$$

3. Making use of the property of deviatoric tensors, the inner product of $\mathbf{T}$ and $\nabla\mathbf{u}$ can be written alternatively as

$$\mathbf{T}:\nabla\mathbf{u} = \mathbf{T}^d:\mathbf{L}^d + \mathbf{T}^h:\mathbf{L}^h = \mathbf{T}^d:\mathbf{L}^d + \frac{1}{3}(\mathrm{tr}\mathbf{T})\nabla\cdot\mathbf{u}. \tag{28}$$

Making use of the above observations, the free energy imbalance (18) relation can be rewritten as

$$\begin{aligned} \rho\frac{D\Psi}{Dt} \le& \mathbf{T}^d:\mathbf{L}^d - \frac{\mathrm{tr}\mathbf{T}}{3\rho}\frac{D\rho}{Dt} - \varphi\frac{D\rho}{Dt} + \boldsymbol{\xi}\cdot\frac{D}{Dt}\left(\nabla\rho\right) + \nabla\rho\cdot\mathbf{L}^d\boldsymbol{\xi} + \nabla\rho\cdot\mathbf{W}\boldsymbol{\xi} - \frac{1}{3\rho}\nabla\rho\cdot\boldsymbol{\xi}\frac{D\rho}{Dt}\\ &- \frac{\mathbf{q}\cdot\nabla\theta}{\theta} - \rho s\frac{D\theta}{Dt}. \end{aligned} \tag{29}$$

2.2.2 Coleman-Noll type analysis

Invoking Truesdell's principle of equipresence [67], we assume that Ψ, s, $\mathbf{T}$, $\boldsymbol{\xi}$, $\mathbf{q}$, ι, and φ are functions depending on ρ, $\nabla\rho$, $D\rho/Dt$, θ, $\nabla\theta$, and $\mathbf{L}^d$. Specifically, the Helmholtz free energy density Ψ can be written as

$$\Psi = \Psi\left(\rho, \nabla\rho, \frac{D\rho}{Dt}, \theta, \nabla\theta, \mathbf{L}^d\right).$$

The material time derivative of Ψ and the chain rule lead to

$$\begin{aligned}\frac{D\Psi}{Dt} =& \frac{\partial\Psi}{\partial\rho}\frac{D\rho}{Dt} + \frac{\partial\Psi}{\partial(\nabla\rho)} \cdot \frac{D\left(\nabla\rho\right)}{Dt} + \frac{\partial\Psi}{\partial\left(D\rho/Dt\right)}\frac{D^2\rho}{Dt^2} + \frac{\partial\Psi}{\partial\theta}\frac{D\theta}{Dt} + \frac{\partial\Psi}{\partial\left(\nabla\theta\right)} \cdot \frac{D\left(\nabla\theta\right)}{Dt} \\ &+ \frac{\partial\Psi}{\partial\mathbf{L}^d} : \frac{D\mathbf{L}^d}{Dt}.\end{aligned} \tag{30}$$

Now substituting (30) into the free energy imbalance (29) and making use of the relations (22)-(28), we can get

$$\begin{aligned}\rho\frac{D\Psi}{Dt} =& \rho\left(\frac{\partial\Psi}{\partial\rho}\frac{D\rho}{Dt} + \frac{\partial\Psi}{\partial(\nabla\rho)} \cdot \frac{D\left(\nabla\rho\right)}{Dt} + \frac{\partial\Psi}{\partial\left(D\rho/Dt\right)}\frac{D^2\rho}{Dt^2} + \frac{\partial\Psi}{\partial\theta}\frac{D\theta}{Dt} + \frac{\partial\Psi}{\partial\left(\nabla\theta\right)} \cdot \frac{D\left(\nabla\theta\right)}{Dt}\right. \\ &\left. + \frac{\partial\Psi}{\partial\mathbf{L}^d} : \frac{D\mathbf{L}^d}{Dt}\right) \leq \mathbf{T}^d : \mathbf{L}^d - \frac{\mathrm{tr}\mathbf{T}}{3\rho}\frac{D\rho}{Dt} - \varphi\frac{D\rho}{Dt} + \boldsymbol{\xi} \cdot \frac{D}{Dt}\left(\nabla\rho\right) + \nabla\rho \cdot \mathbf{L}^d\boldsymbol{\xi} \\ &+ \nabla\rho \cdot \mathbf{W}\boldsymbol{\xi} - \frac{1}{3\rho}\nabla\rho \cdot \boldsymbol{\xi}\frac{D\rho}{Dt} - \frac{\mathbf{q} \cdot \nabla\theta}{\theta} - \rho s\frac{D\theta}{Dt}.\end{aligned} \tag{31}$$

Grouping terms together, the above inequality is reorganized as

$$\begin{aligned}&\left(\rho\frac{\partial\Psi}{\partial\rho} + \frac{\mathrm{tr}\mathbf{T}}{3\rho} + \varphi + \frac{1}{3\rho}\nabla\rho \cdot \boldsymbol{\xi}\right)\frac{D\rho}{Dt} + \left(\rho\frac{\partial\Psi}{\partial\left(\nabla\rho\right)} - \boldsymbol{\xi}\right) \cdot \frac{D}{Dt}\left(\nabla\rho\right) + \rho\frac{\partial\Psi}{\partial\left(D\rho/Dt\right)}\frac{D^2\rho}{Dt^2} \\ &+ \left(\rho\frac{\partial\Psi}{\partial\theta} + \rho s\right)\frac{D\theta}{Dt} + \rho\frac{\partial\Psi}{\partial\left(\nabla\theta\right)} \cdot \frac{D\left(\nabla\theta\right)}{Dt} + \frac{\mathbf{q} \cdot \nabla\theta}{\theta} + \rho\frac{\partial\Psi}{\partial\mathbf{L}^d} : \frac{D\mathbf{L}^d}{Dt} - \mathbf{L}^d : \left(\mathbf{T}^d + \nabla\rho \otimes \boldsymbol{\xi}\right) \\ &- \mathbf{W} : \left(\nabla\rho \otimes \boldsymbol{\xi}\right) \leq 0.\end{aligned} \tag{32}$$

Here we provide an analysis of (32) by invoking the arguments made by Coleman and Noll [11]. We notice that (32) is linear in $D(\nabla\rho)/Dt$, $D^2\rho/Dt^2$, $D\theta/Dt$, $D(\nabla\theta)/Dt$, $D\mathbf{L}^d/Dt$, and $\mathbf{W}$. Through appropriate choices of external forces and external sources, we may have arbitrary levels of the material rates of the state variables and the spin tensor in (32) at a particular time. Hence, in order to satisfy (32), we must have

$$\boldsymbol{\xi} = \rho \frac{\partial \Psi}{\partial \left(\nabla \rho\right)}, \tag{33}$$

$$\frac{\partial \Psi}{\partial \left(D\rho/Dt\right)} = 0, \tag{34}$$

$$s = -\frac{\partial \Psi}{\partial \theta}, \tag{35}$$

$$\frac{\partial \Psi}{\partial \left(\nabla \theta\right)} = \mathbf{0}, \tag{36}$$

$$\frac{\partial \Psi}{\partial \mathbf{L}^d} = -\left(\frac{\partial \Psi}{\partial \mathbf{L}^d}\right)^T, \tag{37}$$

$$\nabla \rho \otimes \boldsymbol{\xi} = \boldsymbol{\xi} \otimes \nabla \rho. \tag{38}$$

Due to the symmetry of $\mathbf{L}^d$, $\partial \Psi / \partial \mathbf{L}^d$ has to be symmetric. This fact together with (37) implies

$$\frac{\partial \Psi}{\partial \mathbf{L}^d} = \mathbf{0}. \tag{39}$$

According to (34), (36), and (39), the Helmholtz free energy density Ψ has to be independent of $D\rho/Dt$, $\nabla\theta$, and $\mathbf{L}^d$. It can be written as

$$\Psi = \Psi\left(\rho, \nabla \rho, \theta\right). \tag{40}$$

The relation (32) is reduced to

$$\left(\rho \frac{\partial \Psi}{\partial \rho} + \frac{\mathrm{tr}\mathbf{T}}{3\rho} + \varphi + \frac{1}{3\rho}\nabla\rho \cdot \boldsymbol{\xi}\right)\frac{D\rho}{Dt} + \frac{\mathbf{q}\cdot\nabla\theta}{\theta} - \mathbf{L}^d : \left(\mathbf{T}^d + \nabla\rho \otimes \boldsymbol{\xi}\right) \le 0. \tag{41}$$

Based on the above inequality, the following choices are made. While these relations are not the most general possible forms that can satisfy (41), we will show that they do suffice to recover the most common physical models.

$$\varphi = -\frac{\mathrm{tr}\mathbf{T}}{3\rho} - \rho\frac{\partial \Psi}{\partial \rho} - \frac{1}{3\rho}\nabla\rho\cdot\boldsymbol{\xi} - B\frac{D\rho}{Dt}, \tag{42}$$

$$\mathbf{q} = -\kappa \nabla \theta, \tag{43}$$

$$\mathbf{T}^d = 2\bar{\mu}\mathbf{L}^d - \frac{1}{2}\left(\nabla\rho\otimes\boldsymbol{\xi} + \boldsymbol{\xi}\otimes\nabla\rho\right) + \frac{1}{3}\nabla\rho\cdot\boldsymbol{\xi}\mathbf{I}, \tag{44}$$

where B, κ, and $\bar{\mu}$ are scalar valued functions.

Remark 2. *The relation* (38) *can be viewed as a result of objectivity. In conjunction with* (33)*, it can be rewritten as*

$$\nabla \rho \otimes \rho \frac{\partial \Psi}{\partial \left(\nabla \rho \right)} = \rho \frac{\partial \Psi}{\partial \left(\nabla \rho \right)} \otimes \nabla \rho. \tag{45}$$

It poses a constraint on how the non-local gradient term $\nabla \rho$ *can enter into the free energy density function* Ψ*. It has been shown in [9] that terms in the form of* $\mathfrak{d} \cdot \nabla \rho$ *or* $\mathfrak{C} : \nabla^2 \rho$ *, with* $\mathfrak{d}$ *being a constant vector and* $\mathfrak{C}$ *being a constant second-order tensor, cannot enter into the free energy density function* Ψ*. This assertion can be easily justified using the constraint relation* (45)*. We will only consider the case with* $\nabla \rho$ *appearing in the free energy density function* Ψ *as* $|\nabla \rho|^2$*. This is in fact the case considered by van der Waals in his seminal work [69]. This special choice for the Helmholtz free energy density function guarantees the satisfaction of the relation* (38)*.*

Remark 3. *It should be pointed out that* (42)*-*(44) *are specific choices made to guarantee the inequality* (41)*. It is feasible to propose more general constitutive relations for* φ*,* $\mathbf{q}$*, and* $\mathbf{T}^d$ *which satisfy the inequality* (41)*. However, discussion of such a general constitutive theory is beyond the scope of this work.*

2.2.3 Constitutive relations

Based on the relations (42)-(44), we can obtain the constitutive relations expressed in terms of Ψ.

Microstress

The relation (33) gives the constitutive relation for the microstress,

$$\boldsymbol{\xi} = \rho \frac{\partial \Psi}{\partial \left(\nabla \rho \right)}. \tag{46}$$

Cauchy stress

From the relations (33), (42), (43), and the microforce balance equation (10), we have the constitutive relation for $\mathrm{tr}\mathbf{T}$ as

$$\frac{\mathrm{tr}\mathbf{T}}{3} = \rho \nabla \cdot \left(\rho \frac{\partial \Psi}{\partial \left(\nabla \rho \right)} \right) - \rho^2 \frac{\partial \Psi}{\partial \rho} - \frac{1}{3} \rho \frac{\partial \Psi}{\partial \left(\nabla \rho \right)} \cdot \nabla \rho + \rho l - B \rho \frac{D\rho}{Dt}. \tag{47}$$

Replacing the microstress $\boldsymbol{\xi}$ by the relations (33), the deviatoric part of the Cauchy stress is given by the choice (44).

$$\mathbf{T}^d = 2\bar{\mu}\mathbf{L}^d - \frac{\rho}{2}\left(\nabla\rho \otimes \frac{\partial\Psi}{\partial\left(\nabla\rho\right)} + \frac{\partial\Psi}{\partial\left(\nabla\rho\right)} \otimes \nabla\rho\right) + \frac{\rho}{3}\nabla\rho \cdot \frac{\partial\Psi}{\partial\left(\nabla\rho\right)}\mathbf{I}. \tag{48}$$

Combining the two parts, the Cauchy stress $\mathbf{T}$ reads

$$\begin{aligned}\mathbf{T} =& \mathbf{T}^d + \frac{\mathrm{tr}\mathbf{T}}{3}\mathbf{I} \\ =& 2\bar{\mu}\mathbf{L}^d - \frac{\rho}{2}\left(\nabla\rho \otimes \frac{\partial\Psi}{\partial\left(\nabla\rho\right)} + \frac{\partial\Psi}{\partial\left(\nabla\rho\right)} \otimes \nabla\rho\right) \\ &+ \left(\rho\nabla\cdot\left(\rho\frac{\partial\Psi}{\partial\left(\nabla\rho\right)}\right) - \rho^2\frac{\partial\Psi}{\partial\rho} + \rho l - B\rho\frac{D\rho}{Dt}\right)\mathbf{I}.\end{aligned} \tag{49}$$

Heat flux

The constitutive relation for the heat flux, given by the choice (43), is the Fourier's law [47].

$$\mathbf{q} = -\kappa\nabla\theta. \tag{50}$$

Entropy

The relation (35) defines the entropy density s as

$$s = -\frac{\partial\Psi}{\partial\theta}. \tag{51}$$

This definition coincides with the classical thermodynamic definition [47]. Consequently, the internal energy density ι is given by

$$\iota = \Psi + \theta s = \Psi - \theta\frac{\partial\Psi}{\partial\theta}. \tag{52}$$

2.3 Dissipation inequalities

In this section, the choices (42)-(44) are validated by analyzing the dissipation of the model. It will be clear how different terms enter into the dissipative mechanisms in isolated and isothermal processes.

Lemma 1. *Given the constitutive relations* (46)–(52), *the dissipation* $\mathcal{D}$ *defined in* (12) *takes* *the form*

$$\mathcal{D}=\frac{1}{\theta}2\bar{\mu}|\mathbf{L}^d|^2+\frac{1}{\theta}B\left(\frac{D\rho}{Dt}\right)^2+\frac{1}{\theta^2}\kappa|\nabla\theta|^2. \tag{53}$$

Proof. We start by considering the internal energy balance equation

$$\rho\frac{D\iota}{Dt}=\mathbf{T}:\nabla\mathbf{u}-\varphi\frac{D\rho}{Dt}+\boldsymbol{\xi}\cdot\nabla\left(\frac{D\rho}{Dt}\right)-\nabla\cdot\mathbf{q}+\rho r. \tag{54}$$

It is known from (28) that

$$\mathbf{T}:\nabla\mathbf{u}=\mathbf{T}^d:\mathbf{L}^d+\frac{1}{3}\left(\mathrm{tr}\mathbf{T}\right)\nabla\cdot\mathbf{u}. \tag{55}$$

Making use of the constitutive relation (48), we have

$$\begin{aligned}\mathbf{T}^d:\mathbf{L}^d=&\mathbf{L}^d:2\bar{\mu}\mathbf{L}^d-\frac{\rho}{2}\left(\nabla\rho\otimes\frac{\partial\Psi}{\partial\left(\nabla\rho\right)}+\frac{\partial\Psi}{\partial\left(\nabla\rho\right)}\otimes\nabla\rho\right):\mathbf{L}^d+\frac{\rho}{3}\nabla\rho\cdot\frac{\partial\Psi}{\partial\left(\nabla\rho\right)}\mathbf{I}:\mathbf{L}^d\\ =&2\bar{\mu}|\mathbf{L}^d|^2-\frac{\rho}{2}\left(\nabla\rho\otimes\frac{\partial\Psi}{\partial\left(\nabla\rho\right)}+\frac{\partial\Psi}{\partial\left(\nabla\rho\right)}\otimes\nabla\rho\right):\mathbf{L}^d.\end{aligned} \tag{56}$$

According to the constitutive relation (47), we have

$$\begin{aligned}\frac{1}{3}\left(\mathrm{tr}\mathbf{T}\right)\nabla\cdot\mathbf{u}=&\rho\nabla\cdot\left(\rho\frac{\partial\Psi}{\partial\left(\nabla\rho\right)}\right)\nabla\cdot\mathbf{u}-\rho^2\frac{\partial\Psi}{\partial\rho}\nabla\cdot\mathbf{u}-\frac{1}{3}\rho\frac{\partial\Psi}{\partial\left(\nabla\rho\right)}\cdot\nabla\rho\nabla\cdot\mathbf{u}\\ &+\rho l\nabla\cdot\mathbf{u}-B\rho\frac{D\rho}{Dt}\nabla\cdot\mathbf{u}\\ =&-\nabla\cdot\left(\rho\frac{\partial\Psi}{\partial\left(\nabla\rho\right)}\right)\frac{D\rho}{Dt}+\rho\frac{\partial\Psi}{\partial\rho}\frac{D\rho}{Dt}+\frac{1}{3}\frac{\partial\Psi}{\partial\left(\nabla\rho\right)}\cdot\nabla\rho\frac{D\rho}{Dt}\\ &-l\frac{D\rho}{Dt}+B\rho^2\left(\nabla\cdot\mathbf{u}\right)^2.\end{aligned} \tag{57}$$

Recalling from the relation (27), we have

$$\begin{aligned}\boldsymbol{\xi}\cdot\nabla\left(\frac{D\rho}{Dt}\right)=&\boldsymbol{\xi}\cdot\left[\frac{D}{Dt}\left(\nabla\rho\right)+\mathbf{L}^d\nabla\rho+\mathbf{W}^T\nabla\rho-\frac{D\rho/Dt}{3\rho}\nabla\rho\right]\\ =&\rho\frac{\partial\Psi}{\partial\left(\nabla\rho\right)}\cdot\left[\frac{D}{Dt}\left(\nabla\rho\right)+\mathbf{L}^d\nabla\rho+\mathbf{W}^T\nabla\rho-\frac{D\rho/Dt}{3\rho}\nabla\rho\right].\end{aligned} \tag{58}$$

The microforce balance equation implies $\varphi=-\nabla\cdot\boldsymbol{\xi}-l$. Consequently, we have

$$\varphi\frac{D\rho}{Dt}=-\nabla\cdot\boldsymbol{\xi}\frac{D\rho}{Dt}-l\frac{D\rho}{dD}. \tag{59}$$

Now substituting (55)-(59) into (54), and using (38) repeatedly, we obtain

$$
\begin{aligned}
\rho\frac{D\iota}{Dt} =&2\bar{\mu}|\mathbf{L}^d|^2 - \frac{\rho}{2}\left(\nabla\rho\otimes\frac{\partial\Psi}{\partial\left(\nabla\rho\right)} + \frac{\partial\Psi}{\partial\left(\nabla\rho\right)}\otimes\nabla\rho\right) : \mathbf{L}^d - \nabla\cdot\left(\rho\frac{\partial\Psi}{\partial\left(\nabla\rho\right)}\right)\frac{D\rho}{Dt} \\
&+ \rho\frac{\partial\Psi}{\partial\rho}\frac{D\rho}{Dt} + \frac{1}{3}\frac{\partial\Psi}{\partial\left(\nabla\rho\right)}\cdot\nabla\rho\frac{D\rho}{Dt} - l\frac{D\rho}{Dt} + B\rho^2\left(\nabla\cdot\mathbf{u}\right)^2 + \nabla\cdot\boldsymbol{\xi}\frac{D\rho}{Dt} + l\frac{D\rho}{Dt} \\
&+ \rho\frac{\partial\Psi}{\partial\left(\nabla\rho\right)}\cdot\left[\frac{D}{Dt}\left(\nabla\rho\right) + \mathbf{L}^d\nabla\rho + \mathbf{W}^T\nabla\rho - \frac{D\rho/Dt}{3\rho}\nabla\rho\right] - \nabla\cdot\mathbf{q} + \rho r \\
&= 2\bar{\mu}|\mathbf{L}^d|^2 + B\rho^2\left(\nabla\cdot\mathbf{u}\right)^2 + \rho\frac{\partial\Psi}{\partial\rho}\frac{D\rho}{Dt} + \rho\frac{\partial\Psi}{\partial\left(\nabla\rho\right)}\cdot\frac{D}{Dt}\left(\nabla\rho\right) - \nabla\cdot\mathbf{q} + \rho r \\
&= 2\bar{\mu}|\mathbf{L}^d|^2 + B\rho^2\left(\nabla\cdot\mathbf{u}\right)^2 + \rho\left(\frac{D\Psi}{Dt} - \frac{\partial\Psi}{\partial\theta}\frac{D\theta}{Dt}\right) - \nabla\cdot\mathbf{q} + \rho r \\
&= 2\bar{\mu}|\mathbf{L}^d|^2 + B\rho^2\left(\nabla\cdot\mathbf{u}\right)^2 + \rho\left(\frac{D\iota}{Dt} - \theta\frac{Ds}{Dt}\right) - \nabla\cdot\mathbf{q} + \rho r.
\end{aligned}
$$

Moving all time derivative terms to the left hand side yields

$$
\rho\frac{Ds}{Dt} = \frac{1}{\theta}\bar{\mu}|\mathbf{L}^d|^2 + \frac{1}{\theta}B\rho^2\left(\nabla\cdot\mathbf{u}\right)^2 - \frac{1}{\theta}\nabla\cdot\mathbf{q} + \frac{1}{\theta}\rho r.
$$

By definition, we have

$$
\begin{aligned}
\mathcal{D} :=&\rho\frac{Ds}{Dt} + \nabla\cdot\left(\frac{\mathbf{q}}{\theta}\right) - \frac{\rho r}{\theta} \\
=&\frac{1}{\theta}2\bar{\mu}|\mathbf{L}^d|^2 + \frac{1}{\theta}B\rho^2\left(\nabla\cdot\mathbf{u}\right)^2 - \frac{\mathbf{q}\cdot\nabla\theta}{\theta^2} \\
=&\frac{1}{\theta}2\bar{\mu}|\mathbf{L}^d|^2 + \frac{1}{\theta}B\rho^2\left(\nabla\cdot\mathbf{u}\right)^2 + \frac{1}{\theta^2}\kappa|\nabla\theta|^2,
\end{aligned}
$$

which completes the proof. □

The dissipation formulation (53) suggests that the model will guarantee the second law of thermodynamics if the material moduli are positive semi-definite, which is summarized in the following theorem.

Theorem 1. *If $\bar{\mu}$, κ, and B are non-negative, the system of balance equations* (7)-(11) *satisfies the second law of thermodynamics in the following sense.*

$$
\mathcal{D} = \frac{1}{\theta}2\bar{\mu}|\mathbf{L}^d|^2 + \frac{1}{\theta}B\rho^2\left(\nabla\cdot\mathbf{u}\right)^2 + \frac{1}{\theta^2}\kappa|\nabla\theta|^2 \geq 0.
$$

The proof of this theorem follows straightforwardly from Lemma 1. The significance of this theorem is that the modeler only needs to design an explicit formulation for the thermodynamic potential. Once it is given, the model is closed with non-negative dissipation. Under isothermal conditions, the entropy dissipation relation will degenerate into an inequality for the summation of the Helmholtz free energy and the kinetic energy.

Lemma 2. *Under the isothermal condition, if* $\mathbf{u} = \mathbf{0}$ *and* $\boldsymbol{\xi} \cdot \mathbf{n} = 0$ *on the boundary* $\partial\Omega_t$*, the following relation holds.*

$$\frac{d}{dt}\int_{\Omega_t} \rho \left(\Psi + \frac{|\mathbf{u}|^2}{2} \right) dV_{\mathbf{x}} = \int_{\Omega_t} \left(\rho \mathbf{b} \cdot \mathbf{u} + l \frac{D\rho}{Dt} - \theta \mathcal{D} \right) dV_{\mathbf{x}}. \tag{60}$$

Proof. Since θ is constant, according to $\Psi = \iota - \theta s$, one has

$$\frac{D\Psi}{Dt} = \frac{D\iota}{Dt} - \theta \frac{Ds}{Dt}.$$

and

$$\Psi + \frac{1}{2}|\mathbf{u}|^2 = \iota + \frac{1}{2}|\mathbf{u}|^2 - \theta s.$$

Multiplying the the above equation with ρ and integrating over Ω_t results in

$$\begin{aligned} \frac{d}{dt}\int_{\Omega_t} \rho \left(\Psi + \frac{1}{2}|\mathbf{u}|^2 \right) dV_{\mathbf{x}} =& \frac{d}{dt}\int_{\Omega_t} \rho \left(\iota + \frac{1}{2}|\mathbf{u}|^2 - \theta s \right) dV_{\mathbf{x}} \\ =& \int_{\partial\Omega_t} \left(\mathbf{T}\mathbf{u} + \frac{D\rho}{Dt}\boldsymbol{\xi} \right) \cdot \mathbf{n} dA_{\mathbf{x}} + \int_{\Omega_t} \left(\rho \mathbf{b} \cdot \mathbf{u} + l \frac{D\rho}{Dt} - \theta \mathcal{D} \right) dV_{\mathbf{x}}. \end{aligned}$$

The boundary integral terms are canceled due to the boundary conditions, and hence

$$\frac{d}{dt}\int_{\Omega_t} \rho \left(\Psi + \frac{1}{2}|\mathbf{u}|^2 \right) dV_{\mathbf{x}} = \int_{\Omega_t} \left(\rho \mathbf{b} \cdot \mathbf{u} + l \frac{D\rho}{Dt} - \theta \mathcal{D} \right) dV_{\mathbf{x}},$$

which completes the proof of the lemma. □

Based on Lemma 2, we may obtain the following stability theorem for isothermal processes.

Theorem 2. *If (1) the system undergoes an isothermal process, (2)* $\mathbf{u} = \mathbf{0}$ *and* $\boldsymbol{\xi} \cdot \mathbf{n} = 0$ *on the boundary* $\partial\Omega_t$*, (3) the forces* $\mathbf{b} = \mathbf{0}$ *and* $l = 0$ *in* Ω_t*, and (4) the material moduli* $\bar{\mu}$ *and* B *are non-negative, the stability of the system is given by the following dissipation relation.*

$$\frac{d}{dt}\int_{\Omega_t} \rho \left(\Psi + \frac{|\mathbf{u}|^2}{2} \right) dV_{\mathbf{x}} = -\int_{\Omega_t} \left(2\bar{\mu}|\mathbf{L}^d|^2 + B\rho^2 \left(\nabla \cdot \mathbf{u} \right)^2 \right) dV_{\mathbf{x}} \le 0.$$

Remark 4. *According to the constitutive relation* (46)*, the boundary condition* $\boldsymbol{\xi} \cdot \mathbf{n} = 0$ *is*

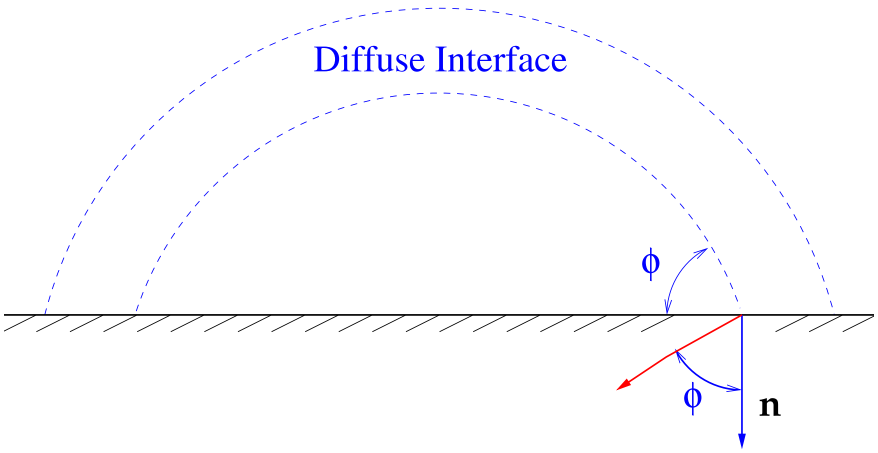

Figure 1: Illustration of the contact angle boundary condition (61). The red arrow points in the direction $-\nabla\rho/\|\nabla\rho\|$.

equivalent to $\nabla\rho\cdot\mathbf{n}=0$*. The general contact-angle boundary condition is*

$$-\frac{\nabla\rho}{\|\nabla\rho\|}\cdot\mathbf{n}=\cos(\phi), \tag{61}$$

wherein

$$\|\nabla\rho\|=\sqrt{\nabla\rho\cdot\nabla\rho},$$

and ϕ *is the contact angle of the diffuse-interface against the wall boundary measured in the vapor phase (see Figure 1). Hence,* $\nabla\rho\cdot\mathbf{n}=0$ *gives the ninety-degree contact angle boundary condition.*

2.4 The van der Waals fluid model

In the preceding section, a general continuum mechanics modeling framework has been established, with the objective of taking non-local effects into account. Theorems 1 and 2 reveal that the model is thermodynamically consistent if the material moduli are positive semi-definite. Thus, the modeling work is principally reduced to a proper design of the thermodynamic potential. This design procedure is primarily based on the consideration of thermodynamics. Our discussion will focus on the van der Waals fluid. The full thermomechanical theory of the van der Waals fluid, initially derived by Dunn and Serrin [17], will be recovered. We will discuss preliminary thermodynamic properties of the system.

2.4.1 Governing equations

Van der Waals' theory [69] is considered well-suited for describing liquid-vapor phase transitions. In thermodynamics, the Helmholtz free energy density for the van der Waals fluid, Ψ, is given by

$$\Psi(\rho, \theta, \nabla\rho) = \Psi_{loc}(\rho, \theta) + \frac{\lambda}{2\rho}|\nabla\rho|^2, \tag{62}$$

$$\Psi_{loc}(\rho, \theta) = -a\rho + R\theta \log\left(\frac{\rho}{b-\rho}\right) - C_v\theta \log\left(\frac{\theta}{\theta_{ref}}\right) + C_v\theta, \tag{63}$$

where a, b are associated with fluid properties whose meanings will be revealed in the coming discussion; $\theta_{ref} > 0$ is the reference temperature for the model; R is the specific gas constant; C_v is the specific heat capacity for the van der Waals fluid; λ is the capillarity coefficient. In this work, we assume λ is a constant. With the Helmholtz free energy given, the constitutive relations can be readily obtained. According to (46), the microstress for the van der Waals fluid is

$$\boldsymbol{\xi} = \rho \frac{\partial \Psi}{\partial\left(\nabla\rho\right)} = \lambda \nabla\rho.$$

Following (49), the Cauchy stress can be written explicitly as

$$\begin{aligned}\mathbf{T} =& 2\bar{\mu}\mathbf{L}^d - \frac{\rho}{2}\left(\nabla\rho \otimes \frac{\partial\Psi}{\partial\left(\nabla\rho\right)} + \frac{\partial\Psi}{\partial\left(\nabla\rho\right)} \otimes \nabla\rho\right) \\ &+ \left(\rho\nabla\cdot\left(\rho\frac{\partial\Psi}{\partial\left(\nabla\rho\right)}\right) - \rho^2\frac{\partial\Psi}{\partial\rho} + \rho l + B\rho^2\nabla\cdot\mathbf{u}\right)\mathbf{I} \\ =& 2\bar{\mu}\mathbf{L}^d - \lambda\nabla\rho\otimes\nabla\rho + \left(\lambda\rho\Delta\rho - \rho^2\frac{\partial\Psi}{\partial\rho} + \rho l + B\rho^2\nabla\cdot\mathbf{u}\right)\mathbf{I}.\end{aligned}$$

For convenience, the Cauchy stress can be split into three parts:

$$\mathbf{T} = \boldsymbol{\tau} + \boldsymbol{\varsigma} - p\mathbf{I}, \tag{64}$$

wherein

$$\boldsymbol{\tau} = 2\bar{\mu}\mathbf{L}^d + B\rho^2\nabla\cdot\mathbf{u}\mathbf{I}, \tag{65}$$

$$\boldsymbol{\varsigma} = -\lambda\rho\nabla\rho\otimes\nabla\rho + \left(\lambda\rho\Delta\rho + \frac{\lambda}{2}|\nabla\rho|^2 + \rho l\right)\mathbf{I}, \tag{66}$$

$$p = \rho^2\frac{\partial\Psi_{loc}}{\partial\rho} = Rb\frac{\rho\theta}{b-\rho} - a\rho^2. \tag{67}$$

Here, $\boldsymbol{\tau}$ represents the viscous shear stress, $\boldsymbol{\varsigma}$ represents the capillarity, and p stands for the thermodynamic pressure. In the subsequent discussion, we assume

$$\begin{aligned} l &= 0, \\ B &= \left(\bar{\lambda} + \frac{2}{3}\bar{\mu}\right)\frac{1}{\rho^2}, \end{aligned}$$

in which $\bar{\mu}$ and $\bar{\lambda}$ are the first and second viscosity coefficients. With these choices,

$$\boldsymbol{\varsigma} = -\lambda\rho\nabla\rho \otimes \nabla\rho + \left(\lambda\rho\Delta\rho + \frac{\lambda}{2}|\nabla\rho|^2\right)\mathbf{I},$$

which is identical to the stress derived by and named after Korteweg [39], and $\boldsymbol{\tau}$ is the viscous stress for Newtonian fluids:

$$\boldsymbol{\tau} = \bar{\mu}\left(\nabla\mathbf{u} + \nabla\mathbf{u}^T\right) + \bar{\lambda}\nabla\cdot\mathbf{u}\mathbf{I}.$$

The entropy density s and the internal energy density ι are

$$\begin{aligned} s &= -R\log\left(\frac{\rho}{b-\rho}\right) + C_v\log\left(\frac{\theta}{\theta_{ref}}\right), \\ \iota &= -a\rho + C_v\theta + \frac{\lambda}{2\rho}|\nabla\rho|^2. \end{aligned}$$

We recall that in the derivation of the constitutive relation for $\mathrm{tr}\mathbf{T}$ in (47), the microforce balance equation is used. Similarly to the angular momentum balance equation, the microforce balance equation (10) is satisfied by the constitutive relations and decoupled from the system. Let us denote the power expenditure of the microstress as

$$\mathbf{\Pi} = \boldsymbol{\xi} D\rho/Dt = \lambda\rho\nabla\cdot\mathbf{u}\nabla\rho.$$

The governing equation for the van der Waals fluid in terms of the conservation variables are

$$\frac{\partial\rho}{\partial t} + \nabla\cdot(\rho\mathbf{u}) = 0, \tag{68}$$

$$\frac{\partial(\rho\mathbf{u})}{\partial t} + \nabla\cdot(\rho\mathbf{u}\otimes\mathbf{u}) + \nabla p - \nabla\cdot\boldsymbol{\tau} - \nabla\cdot\boldsymbol{\varsigma} = \rho\mathbf{b}, \tag{69}$$

$$\frac{\partial(\rho E)}{\partial t} + \nabla\cdot\left(\left(\rho E + p\right)\mathbf{u} - \left(\boldsymbol{\tau} + \boldsymbol{\varsigma}\right)\mathbf{u}\right) + \nabla\cdot\mathbf{q} + \nabla\cdot\mathbf{\Pi} = \rho\mathbf{b}\cdot\mathbf{u} + \rho r. \tag{70}$$

This system of equations is known as the Navier-Stokes-Korteweg equations [17]. According to Lemma 1, the dissipation for the system is

$$\begin{aligned}\mathcal{D} &= \frac{1}{\theta}2\bar{\mu}|\mathbf{L}^d|^2 + \frac{1}{\theta}B\rho^2\left(\nabla\cdot\mathbf{u}\right)^2 + \frac{1}{\theta^2}\kappa|\nabla\theta|^2 \\ &= \frac{1}{\theta}2\bar{\mu}|\mathbf{L}^d|^2 + \frac{1}{\theta}\left(\bar{\lambda}+\frac{2}{3}\bar{\mu}\right)\left(\nabla\cdot\mathbf{u}\right)^2 + \frac{1}{\theta^2}\kappa|\nabla\theta|^2. \qquad (71)\end{aligned}$$

To ensure the second law of thermodynamics, it is sufficient to require that

$$\bar{\mu}\geq 0, \quad \bar{\lambda}+\frac{2}{3}\bar{\mu}\geq 0, \quad \kappa\geq 0.$$

The term $\mathbf{\Pi}$ was initially introduced by Dunn and Serrin to enforce the thermodynamic consistency and was referred to as the “interstitial working flux” [17]. In our framework, $\nabla\cdot\mathbf{\Pi}$ appears naturally as the power expenditure of the microstress $\boldsymbol{\xi}$. The previously mysterious term finds a rational mechanics explanation in the microforce theory [29].

Remark 5. *If we assume that the interface parameter λ is constant, the capillary force term $\nabla\cdot\boldsymbol{\varsigma}$ can be written in the following non-conservative form.*

$$\nabla\cdot\boldsymbol{\varsigma} = \lambda\rho\nabla\left(\Delta\rho\right). \qquad (72)$$

Remark 6. *Choosing the Helmholtz free energy density function as*

$$\Psi = R\theta\log\left(\rho\right) - C_v\theta\log\left(\frac{\theta}{\theta_{ref}}\right) + C_v\theta,$$

the compressible Navier-Stokes equations can be recovered.

2.4.2 Thermodynamic properties

We start the discussion on the thermodynamic properties by defining the critical point. The critical point $(\rho_{crit},\theta_{crit})$ is defined to be the values of density and temperature that satisfy

$$\frac{\partial p}{\partial\rho}(\rho_{crit},\theta_{crit}) = 0, \qquad \frac{\partial^2 p}{\partial\rho^2}(\rho_{crit},\theta_{crit}) = 0.$$

Simple calculations show that the solutions of the above equations are

$$\rho_{crit} = \frac{b}{3}, \qquad \theta_{crit} = \frac{8ab}{27R},$$

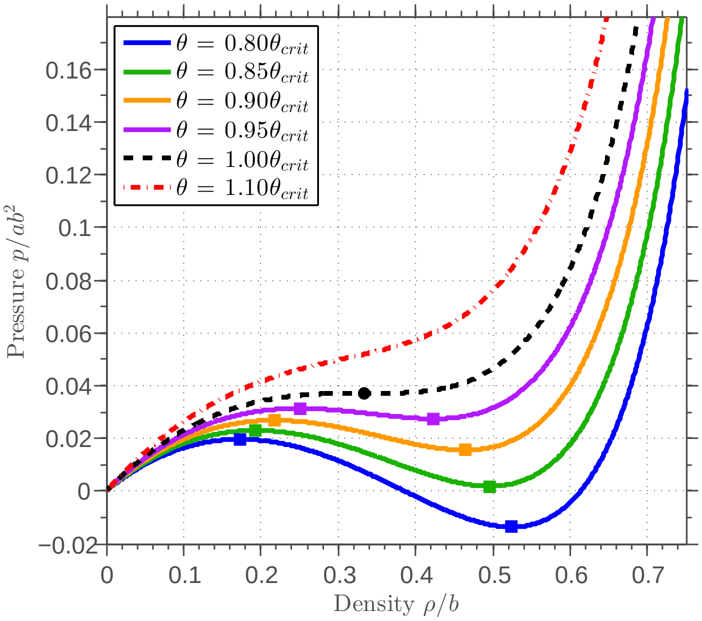

Figure 2: Illustration of the van der Waals pressure p given by (67) at different temperatures. The colored squares delimit the elliptic regions. The critical point is marked by a black circle.

and the critical pressure is $p_{crit} := p(\rho_{crit}, \theta_{crit}) = ab^2/27$. In Figure 2, the van der Waals pressure function is plotted as a function of density by fixing the temperature. It can be observed from the figure that the pressure function is not monotone when the temperature is below the critical temperature, and there is a region in which the pressure drops with the increase of the density. This region is commonly referred to as the elliptic region, since the system of conservation equations is of the first-order elliptic type in the vanishing viscosity-capillarity limit within this region. The approximation property of the van der Waals equation of state is demonstrated by comparing with the data for real fluids. In Figure 3, the van der Waals equation of state is plotted as a function of density at temperature $\theta = 0.85\theta_{crit}$ (blue solid curve). The thermodynamic data for water, carbon dioxide, methane, and propane are downloaded from the NIST database [50] and plotted in the same figure in dimensionless form. As can be seen, the van der Waals model gives a qualitatively accurate description of various fluids in both vapor and liquid states. Considering a binomial expansion

$$\left(1 - \frac{\rho}{b}\right)^{-1} \approx 1 + \frac{\rho}{b} + \frac{\rho^2}{b^2}, \qquad \text{when } \left| \frac{\rho}{b} \right| \ll 1,$$

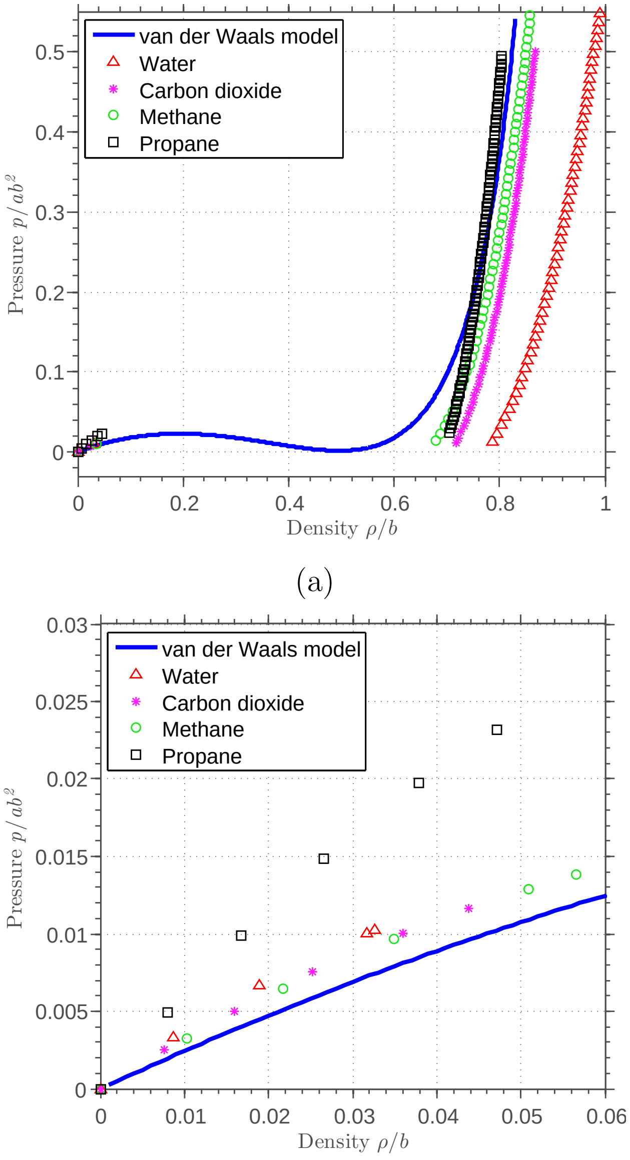

(a)

(b)

Figure 3: Comparison of the van der Waals equation of state with real fluids at temperature $\theta = 0.85\theta_{crit}$. The data for water, carbon dioxide, methane, and propane are obtained from [50] and scaled to dimensionless form. Figure (b) gives a detailed view in the vapor phase.

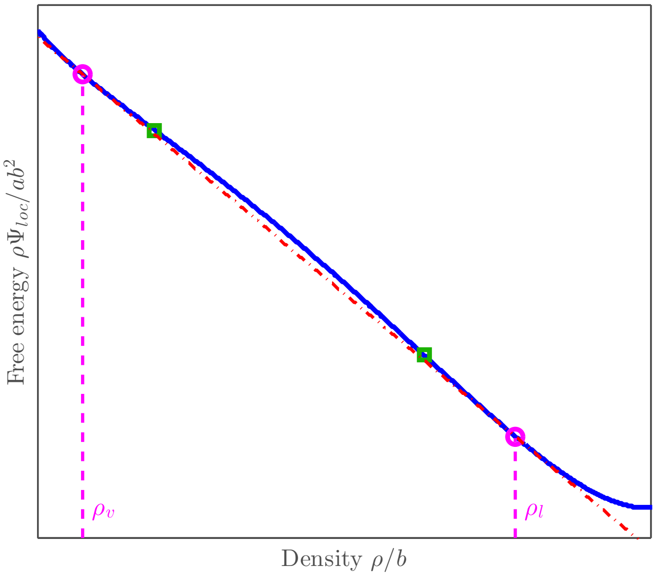

Figure 4: Illustration of the local free energy $\rho\Psi_{loc}$ of the van der Waals fluid given by (63) at temperature $\theta = 0.8\theta_{crit}$. The green squares delimit the elliptic region. The magenta dash-dot-line is the common tangent line passing thorough the Maxwell states, which are marked as the magenta circles.

the thermodynamic pressure can be approximated as

$$p \approx R\theta\rho \left(1 + \left(\frac{1}{b} - \frac{a}{R\theta}\right)\rho^2 + \frac{1}{b^2}\rho^3\right), \tag{73}$$

when the density is small. This suggests that the van der Waals theory can be viewed as a high-order modification of the perfect gas law. Nowadays, modifications of the van der Waals model are introduced by adding more high-order terms to tune the approximation property for specific materials. Examples include the Beattie-Bridgeman equation [6] and the Benedict-Webb-Rubin equation [7]. Another modification was made by Serrin [62], who introduced a new equation of state in the form

$$p^{serrin} = Rb\frac{\rho\theta}{b-\rho} - a\theta^{\hat{s}}\rho^{\hat{r}},$$

wherein $\hat{s} < 1$ and $\hat{r} > 1$ are two parameters. This model was claimed to give very accurate pressures over a large range of temperature.

Next, let us introduce the local electrochemical potential ν_{loc} as

$$\nu_{loc} := \frac{\partial \left(\rho \Psi_{loc}\right)}{\partial \rho}.$$

It does not come from our preceding thermomechanical theory. It is a purely thermodynamic quantity. With the local Helmholtz free energy function given in (63), the electrochemical potential can be written explicitly as

$$\nu_{loc} = -2a\rho + R\theta \log\left(\frac{\rho}{b-\rho}\right) + \frac{R\theta b}{b-\rho} - C_v\theta \log\left(\frac{\theta}{\theta_{ref}}\right) + C_v\theta.$$

The equilibrium state at a given temperature can be determined by constructing a common tangent line passing thorough the free energy curve $\rho\Psi_{loc}$ at two points $(\rho_l, \rho_l\Psi_{loc}(\rho_l))$ and $(\rho_v, \rho_v\Psi_{loc}(\rho_v))$. These two points correspond to the energetically stable liquid and vapor states at the temperature and are usually referred to as the Maxwell states. Mathematically, the common tangent line requires that

$$\frac{\partial(\rho\Psi_{loc})}{\partial\rho}(\rho_v) = \frac{\partial(\rho\Psi_{loc})}{\partial\rho}(\rho_l), \tag{74}$$

$$\rho_v\frac{\partial(\rho\Psi_{loc})}{\partial\rho}(\rho_v) - \rho_v\Psi_{loc}(\rho_v) = \rho_l\frac{\partial(\rho\Psi_{loc})}{\partial\rho}(\rho_l) - \rho_l\Psi_{loc}(\rho_l). \tag{75}$$

The relation (74) implies the local electrochemical potentials ν_{loc} at the two states are identical. The relation (75) can be rewritten as

$$\rho_v^2\frac{\partial\Psi_{loc}}{\partial\rho}(\rho_v) = \rho_l^2\frac{\partial\Psi_{loc}}{\partial\rho}(\rho_l),$$

or, equivalently, $p(\rho_v) = p(\rho_l)$. Therefore, the system is in electrochemical and mechanical equilibrium at the Maxwell states. The Maxwell states together with the common tangent line are illustrated in Figure 4. It can be clearly observed from the figure that the common tangent line lies below the energy curve, which implies the two-phase state is favored against the homogeneous mixture state, according to the minimum energy principle.

The thermodynamic properties of the van der Waals fluid model can be better understood by drawing a θ-ρ phase diagram. In Figure 5, the elliptic region is circumscribed by the dashed spinodal line and is colored in grey. By connecting the Maxwell states, we get the binodal line, which is drawn as the black solid curve in Figure 5. The regions enclosed by the binodal line and the spindoal line are the liquid and vapor metastable regions, which are colored in green and blue respectively. The metastable states are physically accessible

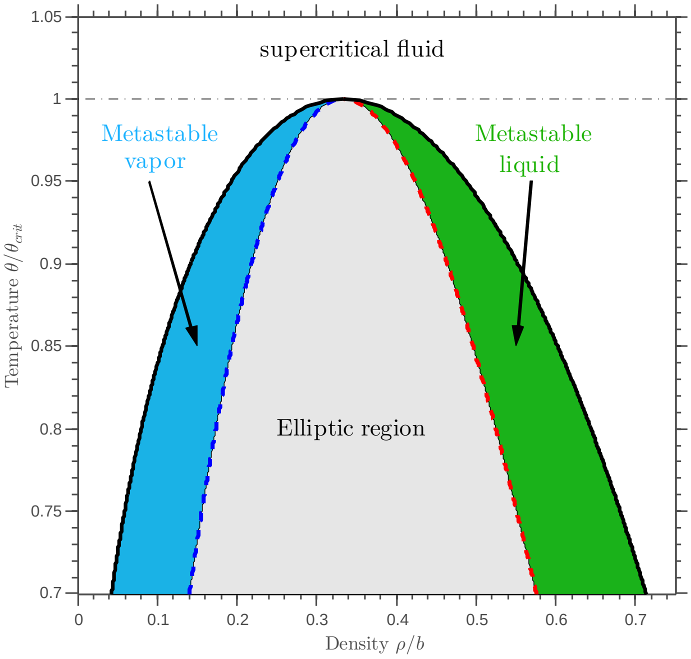

Figure 5: Illustration of the elliptic region, the metastable regions, the spinodal line, and the binodal line for the van der Waals fluid.

but energetically unstable. With enough thermodynamic perturbations, the energy barrier may be overcome and the metastable states may evolve toward a more stable two-phase system. The binodal line and the spinodal line meet at the critical point. Above the critical temperature, the fluid becomes supercritical, and there are no more distinct liquid and vapor states.

3 Numerical analysis

In this section, we focus on the design of numerical schemes for the Navier-Stokes-Korteweg equations that preserve critical structure of the original strong problem.

3.1 Initial-boundary value problem for the Navier-Stokes-Korteweg equations

We consider a fixed, open, connected, and bounded domain $\Omega \subset \mathbb{R}^d$, where d is the number of spatial dimensions. The boundary of Ω is denoted as $\partial\Omega$ and is assumed to be sufficiently smooth. The time interval of interest is denoted $(0, T)$, with $T > 0$. The Navier-Stokes-

Korteweg equations are considered in the space-time domain $\Omega \times (0,T)$ as

$$\frac{\partial \rho}{\partial t} + \nabla \cdot (\rho \mathbf{u}) = 0, \tag{76}$$

$$\frac{\partial (\rho \mathbf{u})}{\partial t} + \nabla \cdot (\rho \mathbf{u} \otimes \mathbf{u} + p\mathbf{I}) - \nabla \cdot \boldsymbol{\tau} - \nabla \cdot \boldsymbol{\varsigma} = \rho \mathbf{b}, \tag{77}$$

$$\frac{\partial (\rho E)}{\partial t} + \nabla \cdot ((\rho E + p)\mathbf{u} - (\boldsymbol{\tau} + \boldsymbol{\varsigma})\mathbf{u}) + \nabla \cdot \mathbf{q} + \nabla \cdot \boldsymbol{\Pi} = \rho \mathbf{b} \cdot \mathbf{u} + \rho r. \tag{78}$$

In this section, we impose periodic boundary conditions for all variables. Therefore, the problem can be regarded to be a periodic flow posed on a d-dimensional torus $\mathbb{T}^d$ in space. Given $\rho_0 : \bar{\Omega} \to (0,b)$, $\mathbf{u}_0 : \bar{\Omega} \to \mathbb{R}^d$, and $\theta_0 : \bar{\Omega} \to \mathbb{R}$ as the initial density, velocity, and temperature, the initial conditions for the strong problem (76)-(78) can be stated as

$$\begin{aligned}
\rho(\mathbf{x},0) =& \rho_0(\mathbf{x}), \\
\mathbf{u}(\mathbf{x},0) =& \mathbf{u}_0(\mathbf{x}), \\
\theta(\mathbf{x},0) =& \theta_0(\mathbf{x}),
\end{aligned}$$

for $\mathbf{x} \in \Omega$. In the above balance equations, $\boldsymbol{\tau}$ is the viscous shear stress; $\boldsymbol{\varsigma}$ is the Korteweg stress; p is the thermodynamic pressure; $\mathbf{q}$ is the heat flux; $\boldsymbol{\Pi}$ is the interstitial working flux or the power expenditure of the microstress; $\mathbf{b} : \Omega \times (0,T) \to \mathbb{R}^d$ is the prescribed body force per unit mass. The constitutive relations for these quantities have been given in Section 2.2.3. For the completeness of this section, we list them here:

$$\begin{aligned}
\boldsymbol{\tau} =& \bar{\mu}\left(\nabla \mathbf{u} + \nabla \mathbf{u}^T\right) + \bar{\lambda} \nabla \cdot \mathbf{u} \mathbf{I}, \\
\boldsymbol{\varsigma} =& \left(\lambda \rho \Delta \rho + \frac{\lambda}{2} |\nabla \rho|^2\right) \mathbf{I} - \lambda \nabla \rho \otimes \nabla \rho, \\
p =& Rb\theta \frac{\rho}{b - \rho} - a\rho^2, \\
\mathbf{q} =& -\kappa \nabla \theta, \\
\boldsymbol{\Pi} =& \lambda \rho \nabla \cdot \mathbf{u} \nabla \rho.
\end{aligned}$$

Remark 7. *In the remainder of this work, the Stokes hypothesis is adopted, i.e.,*

$$\bar{\lambda} = -\frac{2}{3}\bar{\mu}.$$

The total energy can be represented as

$$\rho E = \rho\iota + \frac{1}{2}\rho|\mathbf{u}|^2 = \rho\Psi + \rho\theta s + \frac{1}{2}\rho|\mathbf{u}|^2. \tag{79}$$

The definitions of the thermodynamic state variables are recollected here. The Helmholtz free energy density Ψ, the local Helmholtz free energy density Ψ_{loc}, the local internal energy density ι_{loc}, the internal energy density ι, the entropy density s, and the local electrochemical potential ν_{loc} are defined as

$$\begin{aligned}
\Psi(\rho,\theta,\nabla\rho) =& \Psi_{loc}(\rho,\theta) + \frac{\lambda}{2\rho}|\nabla\rho|^2, && (80)\\
\Psi_{loc}(\rho,\theta) =& -a\rho + R\theta\log\left(\frac{\rho}{b-\rho}\right) - C_v\theta\log\left(\frac{\theta}{\theta_{ref}}\right) + C_v\theta, && (81)\\
\iota =& \iota_{loc} + \frac{\lambda}{2\rho}|\nabla\rho|^2, && (82)\\
\iota_{loc} =& -a\rho + C_v\theta, && (83)\\
s =& -R\log\left(\frac{\rho}{b-\rho}\right) + C_v\log\left(\frac{\theta}{\theta_{ref}}\right), && (84)\\
\nu_{loc} =& -2a\rho + R\theta\log\left(\frac{\rho}{b-\rho}\right) + \frac{R\theta b}{b-\rho} - C_v\theta\log\left(\frac{\theta}{\theta_{ref}}\right) + C_v\theta. && (85)
\end{aligned}$$

3.2 Dimensionless form of the Navier-Stokes-Korteweg equations

In this section, we perform dimensional analysis of the Navier-Stokes-Korteweg equations using the $MLT\Theta$ system. The reference scale of mass, length, time, and temperature are denoted as M_0, L_0, T_0, and θ_0. We may obtain the dimensionless quantities denoted with a superscript $*$:

$$\begin{aligned}
& x = L_0 x^*, \quad t = T_0 t^*, \quad \rho = \frac{M_0}{L_0^3}\rho^*, \quad \theta = \theta_0\theta^*, \quad \mathbf{u} = \frac{L_0}{T_0}\mathbf{u}^*,\\
& p = \frac{M_0}{L_0 T_0^2}p^*, \quad \lambda = \frac{L_0^7}{M_0 T_0^2}\lambda^*, \quad \bar{\mu} = \frac{M_0}{L_0 T_0}\bar{\mu}^*, \quad \boldsymbol{\tau} = \frac{M_0}{T_0^2 L_0}\boldsymbol{\tau}^*,\\
& \boldsymbol{\varsigma} = \frac{M_0}{T_0^2 L_0}\boldsymbol{\varsigma}^*, \quad \mathbf{b} = \frac{L_0}{T_0^2}\mathbf{b}^*, \quad \kappa = \frac{M_0 L_0}{\theta_0 T_0^3}\kappa^*, \quad E = \frac{L_0^2}{T_0^2}E^*,\\
& \mathbf{q} = \frac{M_0}{T_0^3}\mathbf{q}^*, \quad \mathbf{\Pi} = \frac{M_0}{T_0^3}\mathbf{\Pi}^*, \quad r = \frac{L_0^2}{T_0^3}r^*, \quad s = \frac{L_0^2}{T_0^2\theta_0}s^*.
\end{aligned} \tag{86}$$

With the above dimensionless variables, the dimensionless balance equations can be written as

$$
\begin{aligned}
&\frac{M_0}{T_0 L_0^3}\Big(\frac{\partial \rho^*}{\partial t^*} + \nabla^* \cdot (\rho^* \mathbf{u}^*)\Big) = 0,\\
&\frac{M_0}{T_0^2 L_0^2}\Big(\frac{\partial (\rho^* \mathbf{u}^*)}{\partial t^*} + \nabla^* \cdot (\rho^* \mathbf{u}^* \otimes \mathbf{u}^*) + \nabla^* p^* - \nabla^* \cdot \boldsymbol{\tau}^* - \nabla^* \cdot \boldsymbol{\varsigma}^* - \rho^* \mathbf{b}^*\Big) = 0,\\
&\frac{M_0}{T_0^3 L_0}\Big(\frac{\partial (\rho^* E^*)}{\partial t^*} + \nabla^* \cdot ((\rho^* E^* + p^*)\mathbf{u}^* - (\boldsymbol{\tau}^* + \boldsymbol{\varsigma}^*)\mathbf{u}^*) + \nabla^* \cdot \mathbf{q}^* + \nabla^* \cdot \boldsymbol{\Pi}^*\\
&\qquad - \rho^* \mathbf{b}^* \mathbf{u}^* - \rho^* r^*\Big) = 0.
\end{aligned}
$$

The constitutive relations can be rescaled as

$$
\begin{aligned}
p^* &= Rb\frac{L_0 T_0^2 \theta_0 \rho^* \theta^*}{b L_0^3 - M_0 \rho^*} - a\frac{M_0 T_0^2}{L_0^5}\rho^{*2},\\
\boldsymbol{\tau}^* &= \bar{\mu}^* \left(\nabla^* \mathbf{u}^* + \nabla^* \mathbf{u}^{*T}\right) - \frac{2}{3}\bar{\mu}^* \nabla^* \cdot \mathbf{u}^* \mathbf{I},\\
\boldsymbol{\varsigma}^* &= -\lambda^* \nabla^* \rho^* \otimes \nabla^* \rho^* + \left(\lambda^* \rho^* \Delta^* \rho^* + \frac{\lambda^*}{2}|\nabla^* \rho^*|^2\right)\mathbf{I},\\
\mathbf{q}^* &= -\kappa^* \nabla^* \theta^*,\\
s^* &= -\frac{R T_0^2 \theta_0}{L_0^2}\log\left(\frac{M_0 \rho^*}{L_0^3 b - M_0 \rho^*}\right) + \frac{C_v T_0^2 \theta_0}{L_0^2}\log\left(\frac{\theta_0 \theta^*}{\theta_{ref}}\right),\\
\boldsymbol{\Pi}^* &= \lambda^* \rho^* \nabla^* \cdot \mathbf{u}^* \nabla^* \rho^*.
\end{aligned}
$$

The dimensionless viscosity coefficient $\bar{\mu}^* = L_0 T_0 \bar{\mu}/M_0$ measures the ratio of the viscous force to the inertial force; the dimensionless capillarity coefficient $\lambda^* = M_0 T_0^2 \lambda / L_0^7$ measures the ratio of the surface tension to the inertia force. Hence, the two coefficients can be represented in terms of the Reynolds number Re and the Weber number We as

$$
\bar{\mu}^* = \frac{1}{\mathrm{Re}}, \qquad \lambda^* = \frac{1}{\mathrm{We}}.
$$

The capillarity number Ca, which measures the relative effect of the viscous force against the surface tension, is defined as

$$
\mathrm{Ca} = \frac{\mathrm{We}}{\mathrm{Re}}.
$$

The Bond number Bo measures the ratio of the body force to the surface tension and it is defined as

$$\mathrm{Bo} = |\mathbf{b}^*|\,\mathrm{We}\,.$$

There is one standard relation in thermodynamics relating the heat capacity at constant volume C_v and the universal gas constant R:

$$C_v = \frac{R}{\gamma - 1},$$

wherein γ is the heat capacity ratio. Hence, we can denote

$$\frac{C_v}{R} = \frac{1}{\gamma - 1}.$$

Remark 8. *The value of γ is related to the degrees-of-freedom of the gas molecule. For example, γ for water vapor is* 1.33 *[59].*

If the reference scales are chosen as

$$\begin{aligned} \frac{M_0}{L_0^3} &= b, \\ \frac{M_0}{L_0 T_0^2} &= ab^2, \\ \theta_0 = \theta_{crit} &= \frac{8ab}{27R}, \end{aligned}$$

and the reference temperature is selected as

$$\theta_{ref} = \theta_{crit},$$

the dimensionless Navier-Stokes-Korteweg equations can be written as

$$\frac{\partial \rho^*}{\partial t^*} + \nabla^* \cdot (\rho^* \mathbf{u}^*) = 0, \tag{87}$$

$$\frac{\partial (\rho^* \mathbf{u}^*)}{\partial t^*} + \nabla^* \cdot (\rho^* \mathbf{u}^* \otimes \mathbf{u}^*) + \nabla^* p^* - \nabla^* \cdot \boldsymbol{\tau}^* - \nabla^* \cdot \boldsymbol{\varsigma}^* - \rho^* \mathbf{b}^* = 0, \tag{88}$$

$$\begin{aligned} &\frac{\partial (\rho^* E^*)}{\partial t^*} + \nabla^* \cdot ((\rho^* E^* + p^*)\mathbf{u}^* - (\boldsymbol{\tau}^* + \boldsymbol{\varsigma}^*)\mathbf{u}^*) + \nabla^* \cdot \mathbf{q}^* + \nabla^* \cdot \boldsymbol{\Pi}^* \\ &\quad - \rho^* \mathbf{b}^* \mathbf{u}^* - \rho^* r^* = 0, \end{aligned} \tag{89}$$

wherein,

$$p^* = \frac{8\theta^*\rho^*}{27(1-\rho^*)} - \rho^{*2}, \tag{90}$$

$$\boldsymbol{\tau}^* = \frac{1}{\mathrm{Re}}\left(\nabla^*\mathbf{u}^* + \nabla^*\mathbf{u}^{*T} - \frac{2}{3}\nabla^*\cdot\mathbf{u}^*\mathbf{I}\right), \tag{91}$$

$$\boldsymbol{\varsigma}^* = \frac{1}{\mathrm{We}}\left(\left(\rho^*\Delta^*\rho^* + \frac{1}{2}|\nabla^*\rho^*|^2\right)\mathbf{I} - \nabla^*\rho^*\otimes\nabla^*\rho^*\right), \tag{92}$$

$$\mathbf{q}^* = -\kappa^*\nabla^*\theta^*, \tag{93}$$

$$\boldsymbol{\Pi}^* = \frac{1}{\mathrm{We}}\rho^*\nabla^*\cdot\mathbf{u}^*\nabla^*\rho^*, \tag{94}$$

$$\mathrm{Re} = \frac{L_0 b\sqrt{ab}}{\bar{\mu}}, \tag{95}$$

$$\mathrm{We} = \frac{aL_0^2}{\lambda}. \tag{96}$$

Likewise, the thermodynamic state variables (80)-(85) can be rescaled as

$$\Psi^* = \Psi^*_{loc}(\rho,\theta) + \frac{1}{\mathrm{We}}\frac{1}{2\rho^*}|\nabla^*\rho^*|^2, \tag{97}$$

$$\Psi^*_{loc}(\rho,\theta) = -\rho^* + \frac{8}{27}\theta^*\log\left(\frac{\rho^*}{1-\rho^*}\right) - \frac{8}{27(\gamma-1)}\theta^*\log(\theta^*) + \frac{8}{27(\gamma-1)}\theta^*, \tag{98}$$

$$\iota^* = \iota^*_{loc} + \frac{1}{2\,\mathrm{We}\,\rho^*}|\nabla^*\rho^*|^2, \tag{99}$$

$$\iota^*_{loc} = -\rho^* + \frac{8}{27(\gamma-1)}\theta^*, \tag{100}$$

$$\begin{aligned}\nu^*_{loc} = {} & -2\rho^* + \frac{8\theta^*}{27(1-\rho^*)} + \frac{8}{27}\theta^*\log\left(\frac{\rho^*}{1-\rho^*}\right) \\ & - \frac{8}{27(\gamma-1)}\theta^*\log(\theta^*) + \frac{8}{27(\gamma-1)}\theta^*,\end{aligned} \tag{101}$$

$$s^* = -\frac{8}{27}\log\left(\frac{\rho^*}{1-\rho^*}\right) + \frac{8}{27(\gamma-1)}\log\left(\theta^*\right). \tag{102}$$

Henceforth, we will restrict our discussions to the dimensionless form, and the superscript $*$ will be omitted for notational simplicity.

3.3 Functional entropy variables

The mathematical entropy function H is defined to be

$$H := -\rho s = \frac{8}{27}\rho \log\left(\frac{\rho}{1-\rho}\right) - \frac{8}{27(\gamma-1)}\rho \log(\theta). \tag{103}$$

With this definition, the second law of thermodynamics can be written in terms of H as

$$\frac{\partial H}{\partial t} + \nabla \cdot (H\mathbf{u}) - \nabla \cdot \left(\frac{\mathbf{q}}{\theta}\right) + \frac{\rho r}{\theta} = -\frac{1}{\theta}\boldsymbol{\tau} : \nabla \mathbf{u} - \frac{1}{\theta^2}\kappa |\nabla\theta|^2 \le 0.$$

In three dimensions, the conservation variables can be written as

$$\mathbf{U}^T = [U_1, U_2, U_3, U_4, U_5] := [\rho, \rho u_1, \rho u_2, \rho u_3, \rho E].$$

The classical entropy variables for the compressible Navier-Stokes equations are defined as the partial derivatives of the mathematical entropy function H with respect to the conservation variables $\mathbf{U}$. This definition of the entropy variables was understood as an algebraic change-of-variables, since the mathematical entropy function for the compressible Navier-Stokes equation is a function in terms of the conservation variables. In contrast, due to the constitutive relation (99), the temperature θ for the van der Waals fluid model can be expressed in terms of the conservation variables as

$$\theta = \frac{27(\gamma-1)}{8}\left(\frac{U_5}{U_1} - \frac{U_2^2 + U_3^2 + U_4^2}{2U_1^2} - \frac{1}{2\,\mathrm{We}\,U_1}|\nabla U_1|^2 + U_1\right)$$

The above relation includes a non-local gradient-squared term. This fact suggests that when taking derivatives of the temperature with respect to conservation variables, the derivation should be taken in the functional setting. Therefore, for the Navier-Stokes-Korteweg equations, we define the entropy variables $\mathbf{V}$ as the functional derivatives:

$$\mathbf{V} = \frac{\delta H}{\delta \mathbf{U}} = [V_1, V_2, V_3, V_4, V_5]^T = \left[\frac{\delta H}{\delta U_1}, \frac{\delta H}{\delta U_2}, \frac{\delta H}{\delta U_3}, \frac{\delta H}{\delta U_4}, \frac{\delta H}{\delta U_5}\right]^T.$$

Given the test functions $\delta\mathbf{v} = [\delta v_1, \delta v_2, \delta v_3, \delta v_4, \delta v_5]^T$, the entropy variables $\mathbf{V}$ are represented as linear operators acting on the test functions:

$$\begin{aligned} V_1[\delta v_1] = \frac{1}{\theta}\Bigg(&-2\rho + \frac{8}{27}\theta \log\left(\frac{\rho}{1-\rho}\right) - \frac{8}{27(\gamma-1)}\theta\log(\theta) + \frac{8}{27(\gamma-1)}\theta \\ &+ \frac{8\theta}{27(1-\rho)} - \frac{|\mathbf{u}|^2}{2}\Bigg)\delta v_1 + \frac{1}{\mathrm{We}}\frac{1}{\theta}\nabla\rho \cdot \nabla \delta v_1, \end{aligned} \tag{104}$$

$$V_2[\delta v_2] = \frac{u_1}{\theta}\delta v_2, \tag{105}$$

$$V_3[\delta v_3] = \frac{u_2}{\theta}\delta v_3, \tag{106}$$

$$V_4[\delta v_4] = \frac{u_3}{\theta}\delta v_4, \tag{107}$$

$$V_5[\delta v_5] = -\frac{1}{\theta}\delta v_5. \tag{108}$$

Remark 9. *The local Helmholtz free energy $\rho\Psi_{loc}$ can be regarded as a function of ρ and θ. Taking derivatives of $\rho\Psi_{loc}$ gives*

$$\begin{aligned} H =& \frac{\partial(\rho\Psi_{loc})}{\partial\theta}, \\ \nu_{loc} =& \frac{\partial(\rho\Psi_{loc})}{\partial\rho}. \end{aligned}$$

Remark 10. *In Section 2.4.2, we introduced the local electrochemical potential ν_{loc}, defined as:*

$$\nu_{loc} = \frac{\partial(\rho\Psi_{loc})}{\partial\rho} = \Psi_{loc} + \rho\frac{\partial\Psi_{loc}}{\partial\rho}.$$

We define the global electrochemical potential ν by generalizing the partial derivative in the above formula to the functional derivative:

$$\begin{aligned} \nu[\delta v_1] &:= \Psi[\delta v_1] + \rho\frac{\delta\Psi}{\delta\rho}[\delta v_1] \\ &= \left(-2\rho + \frac{8}{27}\theta\log\left(\frac{\rho}{1-\rho}\right) - \frac{8}{27(\gamma-1)}\theta\log(\theta) + \frac{8}{27(\gamma-1)}\theta \right. \\ &\left. + \frac{8\theta}{27(1-\rho)}\right)\delta v_1 + \frac{1}{\mathrm{We}}\nabla\rho\cdot\nabla\delta v_1, \\ &= \nu_{loc}\delta v_1 + \frac{1}{\mathrm{We}}\nabla\rho\cdot\nabla\delta v_1. \end{aligned}$$

Interestingly, with this definition, the entropy variable V_1 can be written as

$$V_1[\delta v_1] = \frac{1}{\theta}\left(\nu - \frac{|\mathbf{u}|^2}{2}\right)[\delta v_1].$$

Consequently, the entropy variables $\mathbf{V}$ *can be compactly represented as*

$$\mathbf{V} = \frac{1}{\theta}\begin{bmatrix} \nu - \dfrac{|\mathbf{u}|^2}{2} \\ u_1 \\ u_2 \\ u_3 \\ -1 \end{bmatrix}. \tag{109}$$

The expression (109) *formally coincides with the definition of the entropy variables for the perfect gas model. However, the entropy variables here should be understood as linear operators in the dual spaces of the conservation variables. The expression* (109) *also hints that the formulation of the entropy variables is invariant under different choices of the Helmholtz free energy functional.*

Theorem 3. *The action of entropy variables* $\mathbf{V}$ *on the Navier-Stokes-Korteweg equations recovers the Clausius-Duhem inequality.*

Proof. Testing the entropy variables $\mathbf{V}$ with the time derivative terms leads to

$$\mathbf{V}\left[\frac{\partial \mathbf{U}}{\partial t}\right] = \frac{\delta H}{\delta \mathbf{U}}\left[\frac{\partial \mathbf{U}}{\partial t}\right] = \frac{\partial H}{\partial t} \tag{110}$$

Choosing the test functions as the advective fluxes results in

$$\begin{aligned} \mathbf{V}\begin{bmatrix} \nabla\cdot(\rho\mathbf{u}) \\ \nabla\cdot(\rho\mathbf{u}\otimes\mathbf{u}) + \nabla p \\ \nabla\cdot(\rho E\mathbf{u} + p\mathbf{u}) \end{bmatrix} &= \nabla\cdot(H\mathbf{u}) \\ &+ \frac{1}{\mathrm{We}\,\theta}\left(\nabla\mathbf{u} : \nabla\rho\otimes\nabla\rho + \frac{1}{2}|\nabla\rho|^2\nabla\cdot\mathbf{u} + \rho\nabla\rho\cdot\nabla(\nabla\cdot\mathbf{u})\right). \end{aligned} \tag{111}$$

We emphasize that the notation $\mathbf{V}[\,]$ denotes the action of the differential operator $\mathbf{V}$ on the term in square brackets. Taking the test functions as the terms related to the capillarity leads to

$$\mathbf{V}\begin{bmatrix} 0 \\ -\nabla\cdot\boldsymbol{\varsigma} \\ -\nabla\cdot(\boldsymbol{\varsigma}\mathbf{u})+\nabla\cdot\boldsymbol{\Pi} \end{bmatrix}$$

$$= -\frac{1}{\mathrm{We}\,\theta}\left(\nabla\mathbf{u}:\nabla\rho\otimes\nabla\rho+\frac{1}{2}|\nabla\rho|^2\nabla\cdot\mathbf{u}+\rho\nabla\rho\cdot\nabla(\nabla\cdot\mathbf{u})\right). \qquad (112)$$

Combing (111)-(112) yields

$$\mathbf{V}\begin{bmatrix} \nabla\cdot(\rho\mathbf{u}) \\ \nabla\cdot(\rho\mathbf{u}\otimes\mathbf{u})+\nabla p-\nabla\cdot\boldsymbol{\varsigma} \\ \nabla\cdot(\rho E\mathbf{u}+p\mathbf{u})-\nabla\cdot(\boldsymbol{\varsigma}\mathbf{u})+\nabla\cdot\boldsymbol{\Pi} \end{bmatrix} = \nabla\cdot(H\mathbf{u}). \qquad (113)$$

Testing the entropy variables against the viscous flux gives

$$\mathbf{V}\begin{bmatrix} 0 \\ -\nabla\cdot\boldsymbol{\tau} \\ -\nabla\cdot(\boldsymbol{\tau}\mathbf{u}) \end{bmatrix} = \frac{1}{\theta}\boldsymbol{\tau}:\nabla\mathbf{u}. \qquad (114)$$

The action of entropy variables on the heat flux, the heat source, and the body force yields

$$\mathbf{V}\begin{bmatrix} 0 \\ -\rho\mathbf{b} \\ \nabla\cdot\mathbf{q}-\rho\mathbf{u}\cdot\mathbf{b}-\rho r \end{bmatrix} = -\nabla\cdot\left(\frac{\mathbf{q}}{\theta}\right)+\frac{\rho r}{\theta}+\frac{1}{\theta^2}\kappa|\nabla\theta|^2. \qquad (115)$$

Combing the relations (110), (113), (114), and (115) leads to

$$\frac{\partial H}{\partial t}+\nabla\cdot(H\mathbf{u})-\nabla\cdot\left(\frac{\mathbf{q}}{\theta}\right)+\frac{\rho r}{\theta} = -\frac{1}{\theta^2}\kappa|\nabla\theta|^2-\frac{1}{\theta}\boldsymbol{\tau}:\nabla\mathbf{u},$$

or equivalently,

$$\frac{\partial(\rho s)}{\partial t}+\nabla\cdot(\rho s\mathbf{u})+\nabla\cdot\left(\frac{\mathbf{q}}{\theta}\right)-\frac{\rho r}{\theta} = \frac{1}{\theta^2}\kappa|\nabla\theta|^2+\frac{1}{\theta}\boldsymbol{\tau}:\nabla\mathbf{u}.$$

This is exactly the dissipation relation for the Navier-Stokes-Korteweg equations. □

3.4 An alternative statement of the strong form of the problem

Theorem 3 suggests that a weak formulation for the Navier-Stokes-Korteweg equations will satisfy the Clausius-Duhem inequality weakly as long as the entropy variables $\mathbf{V}$ are in the test function spaces. For the compressible Navier-Stokes equations, one may rewrite the equation in terms of the entropy variables $\mathbf{V}$, since the mapping between $\mathbf{U}$ and $\mathbf{V}$ is purely algebraic. By using the Bubnov-Galerkin method, the entropy variables are enforced in the test function spaces, and consequently one can prove the entropy stability for the finite element formulation [34]. This approach has been adopted for constructing entropy stable finite element formulations for a variety of problems [3, 8, 10, 34, 35]. However, for the van der Waals fluid, there is an additional difficulty coming from the differential relation in the definition of V_1 in (104). The classical approach becomes nonviable, since there is a second-order differential operator in the definition of V_1, and inverting a differential operator is not a straightforward task. Inspired from the form of V_1, we introduce a new independent variable and couple it with the conservation laws by replacing the pressure. Hence, we may derive a new system of equations, which is a consistent statement of the original strong problem. In doing so, the definition of the entropy variable V_1 is weakly enforced for the mass balance equation, and we can prove entropy stability for the weak problem. To derive the alternative statement of the Navier-Stokes-Korteweg equations, we introduce the auxiliary variable V here as

$$V := \frac{1}{\theta}\left(\nu_{loc} - \frac{|\mathbf{u}|^2}{2}\right) - \frac{1}{\mathrm{We}}\nabla \cdot \left(\frac{\nabla\rho}{\theta}\right). \tag{116}$$

Recall that the local electrochemical potential is related to the thermodynamic pressure by

$$\nu_{loc} = \frac{p}{\rho} + \Psi_{loc}.$$

Hence, the auxiliary variable V can be rewritten as

$$V = \frac{1}{\theta}\left(\frac{p}{\rho} + \Psi_{loc} - \frac{|\mathbf{u}|^2}{2}\right) - \frac{1}{\mathrm{We}}\nabla \cdot \left(\frac{\nabla\rho}{\theta}\right).$$

Rearranging terms in the above relation yields

$$p = \rho V\theta - \rho\Psi_{loc} + \frac{\rho|\mathbf{u}|^2}{2} + \frac{1}{\mathrm{We}}\rho\theta\nabla \cdot \left(\frac{\nabla\rho}{\theta}\right). \tag{117}$$

The above relation is an equivalent expression of the van der Waals equation of state (67) in terms of the newly introduced auxiliary variable V. Taking gradient of both sides of (117), we have

$$\begin{aligned}
\nabla p =& \nabla \left(\rho V \theta + \frac{\rho |\mathbf{u}|^2}{2} + \frac{1}{\mathrm{We}} \rho \theta \nabla \cdot \left(\frac{\nabla \rho}{\theta} \right) \right) - \nabla \left(\rho \Psi_{loc} \right) \\
=& \nabla \left(\rho V \theta + \frac{\rho |\mathbf{u}|^2}{2} + \frac{1}{\mathrm{We}} \rho \theta \nabla \cdot \left(\frac{\nabla \rho}{\theta} \right) \right) - \frac{\partial \left(\rho \Psi_{loc} \right)}{\partial \rho} \nabla \rho - \frac{\partial \left(\rho \Psi_{loc} \right)}{\partial \theta} \nabla \theta \\
=& \nabla \left(\rho V \theta + \frac{\rho |\mathbf{u}|^2}{2} + \frac{1}{\mathrm{We}} \rho \theta \nabla \cdot \left(\frac{\nabla \rho}{\theta} \right) \right) - \nu_{loc} \nabla \rho - H \nabla \theta \\
=& \nabla \left(\rho V \theta + \frac{\rho |\mathbf{u}|^2}{2} + \frac{1}{\mathrm{We}} \rho \theta \nabla \cdot \left(\frac{\nabla \rho}{\theta} \right) \right) \\
& - \left(V \theta + \frac{|\mathbf{u}|^2}{2} + \frac{1}{\mathrm{We}} \theta \nabla \cdot \left(\frac{\nabla \rho}{\theta} \right) \right) \nabla \rho - H \nabla \theta. \qquad (118)
\end{aligned}$$

Using (117), the term $\rho E + p$ can be reorganized as

$$\begin{aligned}
\rho E + p =& \rho \Psi_{loc} - \theta H + \frac{1}{2\,\mathrm{We}} |\nabla \rho|^2 + \frac{1}{2} \rho |\mathbf{u}|^2 \\
& + \rho V \theta + \frac{1}{2} \rho |\mathbf{u}|^2 - \rho \Psi_{loc} + \frac{1}{\mathrm{We}} \rho \theta \nabla \cdot \left(\frac{\nabla \rho}{\theta} \right) \\
=& \rho V \theta - \theta H + \frac{1}{2\,\mathrm{We}} |\nabla \rho|^2 + \rho |\mathbf{u}|^2 + \frac{1}{\mathrm{We}} \rho \theta \nabla \cdot \left(\frac{\nabla \rho}{\theta} \right). \qquad (119)
\end{aligned}$$

Making use of (118) and (119), the pressure force ∇p and the power expenditure of pressure $\nabla \cdot (p\mathbf{u})$ can be consistently represented in terms of V. Then the original strong problem (87)-(89) can be rewritten as

$$\frac{\partial \rho}{\partial t} + \nabla \cdot (\rho \mathbf{u}) = 0, \qquad (120)$$

$$\begin{aligned}
& \frac{\partial (\rho \mathbf{u})}{\partial t} + \nabla \cdot (\rho \mathbf{u} \otimes \mathbf{u}) + \nabla \left(\rho V \theta + \frac{\rho |\mathbf{u}|^2}{2} + \frac{1}{\mathrm{We}} \rho \theta \nabla \cdot \left(\frac{\nabla \rho}{\theta} \right) \right) \\
& - \left(V \theta + \frac{|\mathbf{u}|^2}{2} + \frac{1}{\mathrm{We}} \theta \nabla \cdot \left(\frac{\nabla \rho}{\theta} \right) \right) \nabla \rho - H \nabla \theta - \nabla \cdot \boldsymbol{\tau} - \nabla \cdot \boldsymbol{\varsigma} = \rho \mathbf{b}, \qquad (121)
\end{aligned}$$

$$\begin{aligned}
& \frac{\partial (\rho E)}{\partial t} + \nabla \cdot \left(\left(\rho V \theta - \theta H + \frac{1}{2\,\mathrm{We}} |\nabla \rho|^2 + \rho |\mathbf{u}|^2 + \frac{1}{\mathrm{We}} \rho \theta \nabla \cdot \left(\frac{\nabla \rho}{\theta} \right) \right) \mathbf{u} \right) \\
& - \nabla \cdot \left(\left(\boldsymbol{\tau} + \boldsymbol{\varsigma} \right) \mathbf{u} \right) + \nabla \cdot \mathbf{q} + \nabla \cdot \mathbf{\Pi} = \rho \mathbf{b} \cdot \mathbf{u} + \rho r, \qquad (122)
\end{aligned}$$

$$V = \frac{1}{\theta} \left(\nu_{loc} - \frac{|\mathbf{u}|^2}{2} \right) - \frac{1}{\mathrm{We}} \nabla \cdot \left(\frac{\nabla \rho}{\theta} \right). \qquad (123)$$

The equation (123) defines the auxiliary variable V. Based on our derivation, the new balance equations (120)-(122), together with the auxiliary variable (123), is equivalent to the original Navier-Stokes-Korteweg equations.

3.5 Weak formulation

In this section, we construct a weak formulation based on the alternative statement (120)-(123). In the weak formulation, we solve for six unknowns in three dimensions. The set of variables is denoted as

$$\mathbf{Y} = \begin{bmatrix} Y_1 \\ Y_2 \\ Y_3 \\ Y_4 \\ Y_5 \\ Y_6 \end{bmatrix} := \begin{bmatrix} \rho \\ \frac{u_1}{\theta} \\ \frac{u_2}{\theta} \\ \frac{u_3}{\theta} \\ -\frac{1}{\theta} \\ V \end{bmatrix}. \tag{124}$$

Let $\mathcal{V}_1$ be the trial solution space for $Y_1 = \rho$ and $Y_6 = V$; $\mathcal{V}_2$ be the trial solution space for $Y_{i+1} = u_i/\theta$, $i = 1, 2, 3$; $\mathcal{V}_3$ be the trial solution space for $Y_5 = -1/\theta$. The test function spaces are taken to be identical to the corresponding trial solution spaces. The weak formulation can be stated as follows. Find $Y_1(t) = \rho(t) \in L^2(0,T;\mathcal{V}_1) \cap H^1(0,T;L^2(\Omega))$, $Y_{i+1}(t) = u_i(t)/\theta(t) \in L^2(0,T;\mathcal{V}_2) \cap H^1(0,T;L^2(\Omega))$ for $i = 1, 2, 3$, $Y_5(t) = -1/\theta(t) \in L^2(0,T;\mathcal{V}_3) \cap H^1(0,T;L^2(\Omega))$, and $Y_6(t) = V \in L^2(0,T;\mathcal{V}_1)$, such that

$$\left(w_1, \frac{\partial \rho}{\partial t}\right)_\Omega - \left(\nabla w_1, \rho \mathbf{u}\right)_\Omega = 0, \qquad \forall w_1 \in \mathcal{V}_1, \tag{125}$$

$$\begin{aligned} &\left(\mathbf{w}, \frac{\partial (\rho \mathbf{u})}{\partial t}\right)_\Omega - \left(\nabla \mathbf{w}, \rho \mathbf{u} \otimes \mathbf{u}\right)_\Omega - \left(\nabla \cdot \mathbf{w}, \rho V \theta + \frac{1}{2}\rho |\mathbf{u}|^2 + \frac{1}{\mathrm{We}} \rho \theta \nabla \cdot \left(\frac{\nabla \rho}{\theta}\right)\right)_\Omega \\ &- \left(\mathbf{w}, \left(V\theta + \frac{|\mathbf{u}|^2}{2} + \frac{1}{\mathrm{We}} \theta \nabla \cdot \left(\frac{\nabla \rho}{\theta}\right)\right) \nabla \rho\right)_\Omega - \left(\mathbf{w}, H \nabla \theta\right)_\Omega + \left(\nabla \mathbf{w}, \boldsymbol{\tau}\right)_\Omega + \left(\nabla \mathbf{w}, \boldsymbol{\varsigma}\right)_\Omega \\ &= \left(\mathbf{w}, \rho \mathbf{b}\right)_\Omega, \qquad \forall \mathbf{w} = (w_2; w_3; w_4)^T \in (\mathcal{V}_2)^3, \end{aligned} \tag{126}$$

$$\left(w_5, \frac{\partial(\rho E)}{\partial t}\right)_\Omega - \left(\nabla w_5, \left(\rho V\theta - \theta H + \frac{1}{2\,\mathrm{We}}|\nabla\rho|^2 + \rho|\mathbf{u}|^2 + \frac{1}{\mathrm{We}}\rho\theta\nabla\cdot\left(\frac{\nabla\rho}{\theta}\right)\right)\mathbf{u}\right)_\Omega$$
$$+ (\nabla w_5, \boldsymbol{\tau}\mathbf{u})_\Omega + (\nabla w_5, \varsigma\mathbf{u})_\Omega - (\nabla w_5, \mathbf{q})_\Omega - (\nabla w_5, \mathbf{\Pi})_\Omega$$
$$= (w_5, \rho\mathbf{b}\cdot\mathbf{u})_\Omega + (w_5, \rho r)_\Omega\,, \quad \forall w_5 \in \mathcal{V}_3, \tag{127}$$

$$(w_6, V)_\Omega = \left(w_6, \frac{1}{\theta}\left(\nu_{loc} - \frac{|\mathbf{u}|^2}{2}\right)\right)_\Omega + \left(\nabla w_6, \frac{1}{\mathrm{We}\,\theta}\nabla\rho\right)_\Omega, \forall w_6 \in \mathcal{V}_1, \tag{128}$$

with $\rho(0) = \rho_0$, $\mathbf{u}(0)/\theta(0) = \mathbf{u}_0/\theta_0$, and $-1/\theta(0) = -1/\theta_0$ in Ω.

Comparing (128) with (104), one may find that the auxiliary variable V is identical to the entropy variable V_1 in the weak formulation. Therefore, in the set of variables (124), we are actually solving for the entropy variables $\mathbf{V}$ together with density ρ, which is the conjugate variable to $V_1 = V$. By choosing the test function and trial solution spaces identical for the equations (120) and (123), the entropy variable V_1 is weakly enforced to be in the test function space for the mass balance equation. This is a key ingredient in the proof of the following theorem.

Theorem 4. *Sufficiently smooth weak solutions of the problem* (125)-(128) *verify the second law of thermodynamics, i.e.,*

$$\int_\Omega \left(\frac{\partial H}{\partial t} + \nabla\cdot(H\mathbf{u}) - \nabla\cdot\left(\frac{\mathbf{q}}{\theta}\right) + \frac{\rho r}{\theta}\right) dV_{\mathbf{x}} = -\int_\Omega \frac{1}{\theta}\boldsymbol{\tau} : \nabla\mathbf{u} dV_{\mathbf{x}} - \int_\Omega \frac{\kappa|\nabla\theta|^2}{\theta^2} dV_{\mathbf{x}}. \tag{129}$$

Proof. Choosing $w_1 = V$ in (125) and $w_6 = \partial\rho/\partial t$ in (128) yields

$$\left(V, \frac{\partial\rho}{\partial t}\right)_\Omega - (\nabla V, \rho\mathbf{u})_\Omega = 0,$$
$$\left(\frac{\partial\rho}{\partial t}, V\right)_\Omega = \left(\frac{\partial\rho}{\partial t}, \frac{1}{\theta}\left(\nu_{loc} - \frac{|\mathbf{u}|^2}{2}\right)\right)_\Omega + \left(\nabla\left(\frac{\partial\rho}{\partial t}\right), \frac{1}{\mathrm{We}\,\theta}\nabla\rho\right)_\Omega.$$

Combing the above two relations leads to

$$\int_\Omega \frac{\delta H}{\delta\rho}\left[\frac{\partial\rho}{\partial t}\right] dV_{\mathbf{x}} = \left(\frac{\partial\rho}{\partial t}, \frac{1}{\theta}\left(\nu_{loc} - \frac{|\mathbf{u}|^2}{2}\right)\right)_\Omega + \left(\nabla\left(\frac{\partial\rho}{\partial t}\right), \frac{1}{\mathrm{We}\,\theta}\nabla\rho\right)_\Omega$$
$$= (\nabla V, \rho\mathbf{u})_\Omega\,. \tag{130}$$

Taking $\mathbf{w} = \mathbf{u}/\theta$ in (126) results in

$$\int_\Omega \frac{\delta H}{\delta(\rho\mathbf{u})}\left[\frac{\partial(\rho\mathbf{u})}{\partial t}\right] dV_{\mathbf{x}} = \left(\frac{\mathbf{u}}{\theta}, \frac{\partial(\rho\mathbf{u})}{\partial t}\right)_\Omega = \left(\nabla\left(\frac{\mathbf{u}}{\theta}\right), \rho\mathbf{u}\otimes\mathbf{u}\right)_\Omega$$

$$
\begin{aligned}
&+\left(\nabla\cdot\left(\frac{\mathbf{u}}{\theta}\right),\rho V\theta+\frac{1}{2}\rho|\mathbf{u}|^2+\frac{1}{\mathrm{We}}\rho\theta\nabla\cdot\left(\frac{\nabla\rho}{\theta}\right)\right)_\Omega\\
&+\left(\frac{\mathbf{u}}{\theta},\left(V\theta+\frac{|\mathbf{u}|^2}{2}+\frac{1}{\mathrm{We}}\theta\nabla\cdot\left(\frac{\nabla\rho}{\theta}\right)\right)\nabla\rho\right)_\Omega\\
&+\left(\frac{\mathbf{u}}{\theta},H\nabla\theta\right)_\Omega-\left(\nabla\left(\frac{\mathbf{u}}{\theta}\right),\boldsymbol{\tau}\right)_\Omega-\left(\nabla\left(\frac{\mathbf{u}}{\theta}\right),\boldsymbol{\varsigma}\right)_\Omega\\
&+\left(\frac{\mathbf{u}}{\theta},\rho\mathbf{b}\right)_\Omega.
\end{aligned}
\tag{131}
$$

Choosing $w_5=-1/\theta$ in (127) yields

$$
\begin{aligned}
\int_\Omega\frac{\delta H}{\delta(\rho E)}\left[\frac{\partial(\rho E)}{\partial t}\right]dV_{\mathbf{x}}=\left(-\frac{1}{\theta},\frac{\partial(\rho E)}{\partial t}\right)_\Omega=-\Bigg(\nabla\left(\frac{1}{\theta}\right),\Bigg(&\rho V\theta-\theta H\\
&+\frac{1}{2\,\mathrm{We}}|\nabla\rho|^2+\rho|\mathbf{u}|^2+\frac{1}{\mathrm{We}}\rho\theta\nabla\cdot\left(\frac{\nabla\rho}{\theta}\right)\Bigg)\mathbf{u}\Bigg)_\Omega\\
&+\left(\nabla\left(\frac{1}{\theta}\right),\boldsymbol{\tau}\mathbf{u}\right)_\Omega+\left(\nabla\left(\frac{1}{\theta}\right),\boldsymbol{\varsigma}\mathbf{u}\right)_\Omega\\
&+\left(\frac{1}{\theta},\nabla\cdot\mathbf{q}\right)_\Omega-\left(\nabla\left(\frac{1}{\theta}\right),\boldsymbol{\Pi}\right)_\Omega-\left(\frac{1}{\theta},\rho\mathbf{b}\cdot\mathbf{u}\right)_\Omega\\
&-\left(\frac{1}{\theta},\rho r\right)_\Omega.
\end{aligned}
\tag{132}
$$

Grouping all terms in (130)-(132) involving V, one has

$$
\begin{aligned}
&(\nabla V,\rho\mathbf{u})_\Omega+\left(\nabla\cdot\left(\frac{\mathbf{u}}{\theta}\right),\rho V\theta\right)_\Omega+\left(\frac{\mathbf{u}}{\theta},V\theta\nabla\rho\right)_\Omega-\left(\nabla\left(\frac{1}{\theta}\right),V\theta\rho\mathbf{u}\right)_\Omega\\
&=\int_\Omega\nabla\cdot(\rho V\mathbf{u})\,dV_{\mathbf{x}}=\int_{\partial\Omega}\rho V\mathbf{u}\cdot\mathbf{n}dA_{\mathbf{x}}=0.
\end{aligned}
\tag{133}
$$

Summing all terms in (130)-(132) involving H yields

$$
\begin{aligned}
&\left(\frac{\mathbf{u}}{\theta},H\nabla\theta\right)_\Omega+\left(\nabla\left(\frac{1}{\theta}\right),\theta H\mathbf{u}\right)_\Omega=\left(\frac{\mathbf{u}}{\theta},H\nabla\theta\right)_\Omega-\left(\frac{1}{\theta},\nabla\left(\theta H\mathbf{u}\right)\right)_\Omega\\
&=-\int_\Omega\nabla\cdot(H\mathbf{u})\,dV_{\mathbf{x}}.
\end{aligned}
\tag{134}
$$

Next, collecting all terms in (130)-(132) explicitly involving We, we have

$$\begin{aligned}
&\left(\nabla\cdot\left(\frac{\mathbf{u}}{\theta}\right),\frac{1}{\mathrm{We}}\rho\theta\nabla\cdot\left(\frac{\nabla\rho}{\theta}\right)\right)_\Omega+\left(\frac{\mathbf{u}}{\theta},\frac{1}{\mathrm{We}}\theta\nabla\cdot\left(\frac{\nabla\rho}{\theta}\right)\nabla\rho\right)_\Omega\\
&-\left(\nabla\left(\frac{1}{\theta}\right),\frac{1}{\mathrm{We}}\rho\theta\nabla\cdot\left(\frac{\nabla\rho}{\theta}\right)\mathbf{u}\right)_\Omega-\left(\nabla\left(\frac{1}{\theta}\right),\frac{1}{2\,\mathrm{We}}|\nabla\rho|^2\mathbf{u}\right)_\Omega\\
=&\int_\Omega\frac{1}{\mathrm{We}}\nabla\cdot(\rho\mathbf{u})\,\nabla\cdot\left(\frac{\nabla\rho}{\theta}\right)-\frac{1}{2\,\mathrm{We}}\nabla\left(\frac{1}{\theta}\right)\cdot\mathbf{u}|\nabla\rho|^2dV_{\mathbf{x}}\\
=&-\int_\Omega\frac{1}{\mathrm{We}\theta}\nabla\left(\nabla\cdot(\rho\mathbf{u})\right)\cdot\nabla\rho+\frac{1}{2\,\mathrm{We}\theta}\nabla\cdot\left(\mathbf{u}|\nabla\rho|^2\right)dV_{\mathbf{x}}\\
=&\int_\Omega\frac{-1}{\mathrm{We}\,\theta}\left(\frac{1}{2}|\nabla\rho|^2\nabla\cdot\mathbf{u}+\nabla\rho\otimes\nabla\rho:\nabla\mathbf{u}+\rho\nabla\rho\cdot\nabla\left(\nabla\cdot\mathbf{u}\right)\right)dV_{\mathbf{x}}. \qquad (135)
\end{aligned}$$

Combing all the terms in (130)-(132) including the Korteweg stress $\boldsymbol{\varsigma}$ and the interstitial working, we have

$$\begin{aligned}
&-\left(\nabla\left(\frac{\mathbf{u}}{\theta}\right),\boldsymbol{\varsigma}\right)_\Omega+\left(\nabla\left(\frac{1}{\theta}\right),\boldsymbol{\varsigma}\mathbf{u}\right)_\Omega-\left(\nabla\left(\frac{1}{\theta}\right),\mathbf{\Pi}\right)_\Omega\\
=&-\left(\frac{1}{\theta},\nabla\mathbf{u}:\boldsymbol{\varsigma}\right)_\Omega+\left(\frac{1}{\theta},\nabla\cdot\mathbf{\Pi}\right)_\Omega\\
=&\int_\Omega\frac{1}{\mathrm{We}\,\theta}\left(\frac{1}{2}|\nabla\rho|^2\nabla\cdot\mathbf{u}+\nabla\rho\otimes\nabla\rho:\nabla\mathbf{u}+\rho\nabla\rho\cdot\nabla\left(\nabla\cdot\mathbf{u}\right)\right)dV_{\mathbf{x}}. \qquad (136)
\end{aligned}$$

Making use of (133)-(136), the summation of (130)-(132) gives

$$\begin{aligned}
&\int_\Omega\frac{\delta H}{\delta\rho}\left[\frac{\partial\rho}{\partial t}\right]+\frac{\delta H}{\delta(\rho\mathbf{u})}\left[\frac{\partial(\rho\mathbf{u})}{\partial t}\right]+\frac{\delta H}{\delta(\rho E)}\left[\frac{\partial(\rho E)}{\partial t}\right]dV_{\mathbf{x}}\\
=&-\int_\Omega\nabla\cdot(H\mathbf{u})\,dV_{\mathbf{x}}-\left(\nabla\left(\frac{\mathbf{u}}{\theta}\right),\boldsymbol{\tau}\right)_\Omega+\left(\nabla\left(\frac{1}{\theta}\right),\boldsymbol{\tau}\mathbf{u}\right)_\Omega+\left(\frac{1}{\theta},\rho\mathbf{b}\cdot\mathbf{u}\right)_\Omega\\
&-\left(\frac{1}{\theta},\rho\mathbf{b}\cdot\mathbf{u}\right)_\Omega+\left(\frac{1}{\theta},\nabla\cdot\mathbf{q}\right)_\Omega-\left(\frac{1}{\theta},\rho r\right)_\Omega\\
=&-\int_\Omega\nabla\cdot(H\mathbf{u})\,dV_{\mathbf{x}}-\int_\Omega\frac{1}{\theta}\boldsymbol{\tau}:\nabla\mathbf{u}dV_{\mathbf{x}}+\left(\frac{1}{\theta},\nabla\cdot\mathbf{q}\right)_\Omega-\left(\frac{1}{\theta},\rho r\right)_\Omega\\
=&-\int_\Omega\nabla\cdot(H\mathbf{u})\,dV_{\mathbf{x}}-\int_\Omega\frac{1}{\theta}\boldsymbol{\tau}:\nabla\mathbf{u}dV_{\mathbf{x}}+\int_\Omega\nabla\cdot\left(\frac{\mathbf{q}}{\theta}\right)+\frac{\mathbf{q}\cdot\nabla\theta}{\theta^2}-\frac{\rho r}{\theta}dV_{\mathbf{x}}.
\end{aligned}$$

The above equation implies

$$\int_\Omega\left(\frac{\partial H}{\partial t}+\nabla\cdot(H\mathbf{u})-\nabla\cdot\left(\frac{\mathbf{q}}{\theta}\right)+\frac{\rho r}{\theta}\right)dV_{\mathbf{x}}=-\int_\Omega\frac{1}{\theta}\boldsymbol{\tau}:\nabla\mathbf{u}dV_{\mathbf{x}}-\int_\Omega\frac{\kappa|\nabla\theta|^2}{\theta^2}dV_{\mathbf{x}},$$

which completes the proof of this theorem. $\square$

Remark 11. *In our discussion, we assumed periodic boundary conditions. For periodic boundary conditions, the divergence terms in* (129) *are canceled out and the statement can be simplified as*

$$\int_\Omega \left(\frac{\partial H}{\partial t} + \frac{\rho r}{\theta} \right) dV_{\mathbf{x}} = - \int_\Omega \frac{1}{\theta} \boldsymbol{\tau} : \nabla \mathbf{u} dV_{\mathbf{x}} - \int_\Omega \frac{\kappa |\nabla \theta|^2}{\theta^2} dV_{\mathbf{x}}.$$

Even though we proved the case with periodic boundary conditions, the proof of Theorem 4 can proceed with other boundary conditions, such as no-slip boundary conditions for the velocity field and the heat flux boundary condition for the temperature field. A difficulty emanates from inhomogeneous essential boundary conditions. If there are non-zero functions built in the trial solution spaces, the test functions cannot be chosen as the entropy variables and the preceding proof is no longer valid. The same issue arises for the compressible Navier-Stokes equations [63]. This suggests that the strong imposition of inhomogeneous Dirichlet boundary conditions is not necessarily entropy-dissipative. The weak imposition methodology [5] may provide a framework to more easily establish the entropy inequality.

3.6 Semi-discrete formulation

We perform spatial discretization of (120)-(123) by invoking the Galerkin method [32]. Let $\mathcal{V}_1^h \subset \mathcal{V}_1$, $\mathcal{V}_2^h \subset \mathcal{V}_2$, and $\mathcal{V}_3^h \subset \mathcal{V}_3$ be finite-dimensional function spaces, in which the superscript h denotes a mesh parameter. Then the spatial discretization of (120)-(123) can be stated as follows.

Find $Y_1^h(t) = \rho^h(t) \in L^2(0,T;\mathcal{V}_1^h) \cap H^1(0,T;L^2(\Omega))$, $Y_{i+1}^h(t) = u_i^h(t)/\theta^h(t) \in L^2(0,T;\mathcal{V}_2^h) \cap H^1(0,T;L^2(\Omega))$ for $i = 1,2,3$, $Y_5^h(t) = -1/\theta^h(t) \in L^2(0,T;\mathcal{V}_3^h) \cap H^1(0,T;L^2(\Omega))$, and $Y_6^h = V^h \in L^2(0,T;\mathcal{V}_1^h)$, such that

$$\left(w_1^h, \frac{\partial \rho^h}{\partial t} \right)_\Omega - \left(\nabla w_1^h, \rho \mathbf{u}^h \right)_\Omega = 0, \qquad \forall w_1^h \in \mathcal{V}_1^h, \tag{137}$$

$$\begin{aligned}
&\left(\mathbf{w}^h, \frac{\partial (\rho^h \mathbf{u}^h)}{\partial t} \right)_\Omega - \left(\nabla \mathbf{w}^h, \rho^h \mathbf{u}^h \otimes \mathbf{u}^h \right)_\Omega \\
&- \left(\nabla \cdot \mathbf{w}^h, \rho^h V^h \theta^h + \frac{1}{2} \rho^h |\mathbf{u}^h|^2 + \frac{1}{\mathrm{We}} \rho^h \theta^h \nabla \cdot \left(\frac{\nabla \rho^h}{\theta^h} \right) \right)_\Omega \\
&- \left(\mathbf{w}^h, \left(V^h \theta^h + \frac{|\mathbf{u}^h|^2}{2} + \frac{1}{\mathrm{We}} \theta^h \nabla \cdot \left(\frac{\nabla \rho^h}{\theta^h} \right) \right) \nabla \rho^h \right)_\Omega - \left(\mathbf{w}^h, H^h \nabla \theta^h \right)_\Omega \\
&+ \left(\nabla \mathbf{w}^h, \boldsymbol{\tau}^h \right)_\Omega + \left(\nabla \mathbf{w}^h, \boldsymbol{\varsigma}^h \right)_\Omega = \left(\mathbf{w}^h, \rho^h \mathbf{b} \right)_\Omega, \qquad \forall \mathbf{w}^h = (w_2^h; w_3^h; w_4^h)^T \in \left(\mathcal{V}_2^h \right)^3,
\end{aligned} \tag{138}$$

$$
\begin{aligned}
&\left(w_5^h, \frac{\partial(\rho^h E^h)}{\partial t}\right)_\Omega - \Bigg(\nabla w_5^h, \Bigg(\rho^h V^h \theta^h - \theta^h H^h + \frac{1}{2\,\mathrm{We}}|\nabla\rho^h|^2 + \rho^h|\mathbf{u}^h|^2 \\
&+\frac{1}{\mathrm{We}}\rho^h\theta^h\nabla\cdot\left(\frac{\nabla\rho^h}{\theta^h}\right)\Bigg)\mathbf{u}^h\Bigg)_\Omega + \left(\nabla w_5^h, \boldsymbol{\tau}^h\mathbf{u}^h\right)_\Omega + \left(\nabla w_5^h, \boldsymbol{\varsigma}^h\mathbf{u}^h\right)_\Omega \\
&-\left(\nabla w_5^h, \mathbf{q}^h\right)_\Omega - \left(\nabla w_5^h, \boldsymbol{\Pi}^h\right)_\Omega = \left(w_5^h, \rho^h\mathbf{b}\cdot\mathbf{u}^h\right)_\Omega + \left(w_5^h,\rho^h r\right)_\Omega, \qquad \forall w_5^h\in\mathcal{V}_3^h, \qquad (139)
\end{aligned}
$$

$$
\left(w_6^h, V^h\right)_\Omega = \left(w_6^h, \frac{1}{\theta^h}\left(\nu_{loc}^h - \frac{|\mathbf{u}^h|^2}{2}\right)\right)_\Omega + \left(\nabla w_6^h, \frac{1}{\mathrm{We}\,\theta^h}\nabla\rho^h\right)_\Omega, \qquad \forall w_6^h\in\mathcal{V}_1^h, \qquad (140)
$$

with $\rho^h(0)=\rho_0^h$, $\mathbf{u}^h(0)/\theta^h(0)=\mathbf{u}_0^h/\theta_0^h$, and $-1/\theta^h(0)=-1/\theta_0^h$ in Ω.

In the above formulation, ρ_0^h, $\mathbf{u}_0^h/\theta_0^h$, and $-1/\theta_0^h$ are L^2-projections of $\rho_0(\mathbf{x})$, $\mathbf{u}_0(\mathbf{x})/\theta_0(\mathbf{x})$, and $-1/\theta_0(\mathbf{x})$ onto $\mathcal{V}_1^h$, $\mathcal{V}_2^h$, and $\mathcal{V}_3^h$ respectively. Employing the same techniques used in the proof of Theorem 4, we can obtain the following theorem, which implies that the spatial discretization (137)-(140) is entropy dissipative.

Theorem 5. *The solutions of the semi-discrete formulation* (137)-(140) *satisfy the second law of thermodynamics in the following sense.*

$$
\begin{aligned}
\int_\Omega \left(\frac{\partial H(\rho^h,\theta^h)}{\partial t} + \nabla\cdot\left(H(\rho^h,\theta^h)\mathbf{u}^h\right) - \nabla\cdot\left(\frac{\mathbf{q}^h}{\theta^h}\right) + \frac{\rho^h r}{\theta^h}\right) dV_{\mathbf{x}} \\
= -\int_\Omega \frac{1}{\theta^h}\boldsymbol{\tau}^h : \nabla\mathbf{u}^h dV_{\mathbf{x}} - \int_\Omega \frac{\kappa|\nabla\theta^h|^2}{\left(\theta^h\right)^2} dV_{\mathbf{x}}.
\end{aligned}
$$

Remark 12. *In our implementation, the same discrete space $\mathcal{V}^h$, up to the prescription of the boundary conditions, is used to approximate $\mathcal{V}_1$, $\mathcal{V}_2$, and $\mathcal{V}_3$. Specifically, the Non-Uniform Rational B-Spline (NURBS) basis functions are used to define $\mathcal{V}^h$ as well as the geometry of the computational domain. Consequently, this approach may be considered as isogeometric analysis method [33].*

3.7 The fully discrete formulation

In the preceding section, we have constructed an entropy-dissipative semi-discrete formulation. It remains to design discretizations of the time derivatives such that the dissipation property can be inherited in the time direction. In our previous work [44], we have successfully developed a suite of temporal schemes for the isothermal Navier-Stokes-Korteweg equations. For the thermal case, the difficulty comes from the term $\partial(\rho E)/\partial t$. If one uses the traditional jump operator to approximate the time derivative, it is difficult to estimate the dissipation of the resulting scheme. In this work, the total energy ρE is split into four parts:

$$\rho E = \rho \Psi_{loc} - \theta H + \frac{1}{2}\rho |\mathbf{u}|^2 + \frac{1}{2\,\mathrm{We}}|\nabla \rho|^2, \tag{141}$$

and the time approximation for each of the four parts will be carefully designed to ensure consistency and temporal dissipation. It is noteworthy that, in the design of the discrete scheme, the special quadrature rules developed in [24, 44] will be used repeatedly as a key technique. In the following, we will first state the fully discrete scheme in Section 3.7.1. Following that, five preliminary lemmas will be given in Section 3.7.2. The main results about the entropy-dissipation property and time accuracy are proven in Section 3.7.3.

3.7.1 The fully discrete scheme

To discretize the semi-discrete formulation, the time interval $\mathcal{I} = (0, T)$ is divided into N_{ts} subintervals $\mathcal{I}_n = (t_n, t_{n+1})$, $n = 0, \cdots, N_{ts} - 1$, of size $\Delta t_n = t_{n+1} - t_n$. We use the notation

$$\mathbf{Y}_n^h := \left[\rho_n^h; \frac{u_{1,n}^h}{\theta_n^h}; \frac{u_{2,n}^h}{\theta_n^h}; \frac{u_{3,n}^h}{\theta_n^h}; \frac{-1}{\theta_n^h}; V_n^h\right]^T \tag{142}$$

to denote the fully discrete solutions at the time level n. The fully discrete primitive variables at the same time level can be represented in terms of $\mathbf{Y}_n^h$ as

$$\begin{aligned} \rho_n^h &= \rho^h(\mathbf{Y}_n^h) = Y_{1,n}^h, \\ u_{i,n}^h &= u_i^h(\mathbf{Y}_n^h) = -Y_{i+1,n}^h / Y_{5,n}^h, \quad i = 1, 2, 3, \\ \theta_n^h &= \theta^h(\mathbf{Y}_n^h) = -1/Y_{5,n}^h. \end{aligned}$$

We define the jump of density, linear momentum, and total energy over each time step as

$$[\![\rho_n^h]\!] := \rho_{n+1}^h - \rho_n^h, \tag{143}$$

$$[\![\rho_n^h \mathbf{u}_n^h]\!] := \rho_{n+1}^h \mathbf{u}_{n+1}^h - \rho_n^h \mathbf{u}_n^h, \tag{144}$$

$$\begin{aligned}[\rho_n^h E(\rho_n^h, \mathbf{u}_n^h, \theta_n^h)] :=& (\rho\Psi_{loc})(\rho_{n+\frac{1}{2}}^h, \theta_{n+1}^h) - (\rho\Psi_{loc})(\rho_{n+\frac{1}{2}}^h, \theta_n^h) \\ &+ (\rho\Psi_{loc})(\rho_{n+1}^h, \theta_{n+\frac{1}{2}}^h) - (\rho\Psi_{loc})(\rho_n^h, \theta_{n+\frac{1}{2}}^h) \\ &- \theta_{n+\frac{1}{2}}^h \left(H(\rho_{n+1}^h, \theta_{n+1}^h) - H(\rho_n^h, \theta_n^h) \right) \\ &- \frac{\theta_{n+1}^h - \theta_n^h}{2} \left(H(\rho_{n+\frac{1}{2}}^h, \theta_{n+1}^h) + H(\rho_{n+\frac{1}{2}}^h, \theta_n^h) \right) \\ &+ \frac{(\theta_{n+1}^h - \theta_n^h)^3}{12} \frac{\partial^2 H}{\partial \theta^2}(\rho_{n+\frac{1}{2}}^h, \theta_{n+1}^h) \\ &+ \frac{1}{2} \left(\rho_{n+1}^h |\mathbf{u}_{n+1}^h|^2 - \rho_n^h |\mathbf{u}_n^h|^2 \right) \\ &+ \frac{1}{2\,\mathrm{We}} \left(|\nabla \rho_{n+1}^h|^2 - |\nabla \rho_n^h|^2 \right). \end{aligned} \tag{145}$$

Remark 13. *According to the energy split* (141)*, the definition* (145) *can be rewritten as a summation of four jumps:*

$$[\rho_n^h E(\rho_n^h, \mathbf{u}_n^h, \theta_n^h)] = [\rho_n^h \Psi_{loc}(\rho_n^h, \theta_n^h)] - [\theta_n^h H(\rho_n^h, \theta_n^h)] + [\![\frac{\rho_n^h}{2} |\mathbf{u}_n^h|^2]\!] + [\![\frac{1}{2\,\mathrm{We}} |\nabla \rho_n^h|^2]\!], \tag{146}$$

wherein,

$$\begin{aligned}[\rho_n^h \Psi_{loc}(\rho_n^h, \theta_n^h)] :=& (\rho\Psi_{loc})(\rho_{n+\frac{1}{2}}^h, \theta_{n+1}^h) - (\rho\Psi_{loc})(\rho_{n+\frac{1}{2}}^h, \theta_n^h) \\ &+ (\rho\Psi_{loc})(\rho_{n+1}^h, \theta_{n+\frac{1}{2}}^h) - (\rho\Psi_{loc})(\rho_n^h, \theta_{n+\frac{1}{2}}^h), \end{aligned} \tag{147}$$

$$\begin{aligned}[\theta_n^h H(\rho_n^h, \theta_n^h)] :=& \theta_{n+\frac{1}{2}}^h \left(H(\rho_{n+1}^h, \theta_{n+1}^h) - H(\rho_n^h, \theta_n^h) \right) \\ &+ \frac{\theta_{n+1}^h - \theta_n^h}{2} \left(H(\rho_{n+\frac{1}{2}}^h, \theta_{n+1}^h) + H(\rho_{n+\frac{1}{2}}^h, \theta_n^h) \right) \\ &- \frac{(\theta_{n+1}^h - \theta_n^h)^3}{12} \frac{\partial^2 H}{\partial \theta^2}(\rho_{n+\frac{1}{2}}^h, \theta_{n+1}^h), \end{aligned} \tag{148}$$

$$[\![\frac{\rho_n^h}{2} |\mathbf{u}_n^h|^2]\!] := \frac{1}{2} \left(\rho_{n+1}^h |\mathbf{u}_{n+1}^h|^2 - \rho_n^h |\mathbf{u}_n^h|^2 \right), \tag{149}$$

$$[\![\frac{1}{2\,\mathrm{We}} |\nabla \rho_n^h|^2]\!] := \frac{1}{2\,\mathrm{We}} \left(|\nabla \rho_{n+1}^h|^2 - |\nabla \rho_n^h|^2 \right). \tag{150}$$

The definitions (147) *and* (148) *are inspired by the fact that the summation of first-order partial derivatives approximates the total derivative. In* (148)*, there is an additional third-order perturbation term, whose role will be described in Lemma 6. The jump operators for the kinetic energy and the surface energy follow the classical definition. In the following text, we define* $[\![\theta_n^h]\!] := \theta_{n+1}^h - \theta_n^h$ *to simplify notations.*

With the jump operators defined above, the fully discrete scheme is stated as follows. In each time step, given $\mathbf{Y}_n^h$ and the time step Δt_n, find $\mathbf{Y}_{n+1}^h$ such that for all $w_1^h \in \mathcal{V}^h$,

$\mathbf{w}^h = (w_2^h; w_3^h; w_4^h)^T \in \left(\mathcal{V}^h\right)^3$, $w_5^h \in \mathcal{V}^h$, and $w_6^h \in \mathcal{V}^h$,

$$\mathbf{B}^M(w_1^h; \mathbf{Y}_{n+1}^h) := \left(w_1^h, \frac{[\![\rho_n^h]\!]}{\Delta t_n}\right)_\Omega - \left(\nabla w_1^h, \rho_{n+\frac{1}{2}}^h \mathbf{u}_{n+\frac{1}{2}}^h\right)_\Omega = 0, \tag{151}$$

$$\begin{aligned}
&\mathbf{B}^U(\mathbf{w}^h; \mathbf{Y}_{n+1}^h) := \left(\mathbf{w}^h, \frac{[\![\rho_n^h \mathbf{u}_n^h]\!]}{\Delta t_n}\right)_\Omega - \left(\nabla \mathbf{w}^h, \rho_{n+\frac{1}{2}}^h \mathbf{u}_{n+\frac{1}{2}}^h \otimes \mathbf{u}_{n+\frac{1}{2}}^h\right)_\Omega \\
&- \left(\nabla \cdot \mathbf{w}^h, \rho_{n+\frac{1}{2}}^h V_{n+\frac{1}{2}}^h \theta_{n+\frac{1}{2}}^h + \frac{1}{2}\rho_{n+\frac{1}{2}}^h |\mathbf{u}_{n+\frac{1}{2}}^h|^2 + \frac{1}{\mathrm{We}}\rho_{n+\frac{1}{2}}^h \theta_{n+\frac{1}{2}}^h \nabla \cdot \left(\frac{\nabla \rho_{n+\frac{1}{2}}^h}{\theta_{n+\frac{1}{2}}^h}\right)\right)_\Omega \\
&- \left(\mathbf{w}^h, \left(V_{n+\frac{1}{2}}^h \theta_{n+\frac{1}{2}}^h + \frac{|\mathbf{u}_{n+\frac{1}{2}}^h|^2}{2} + \frac{1}{\mathrm{We}}\theta_{n+\frac{1}{2}}^h \nabla \cdot \left(\frac{\nabla \rho_{n+\frac{1}{2}}^h}{\theta_{n+\frac{1}{2}}^h}\right)\right) \nabla \rho_{n+\frac{1}{2}}^h\right)_\Omega \\
&- \left(\mathbf{w}^h, H_{n+\frac{1}{2}}^h \nabla \theta_{n+\frac{1}{2}}^h\right)_\Omega + \left(\nabla \mathbf{w}^h, \boldsymbol{\tau}_{n+\frac{1}{2}}^h\right)_\Omega + \left(\nabla \mathbf{w}^h, \boldsymbol{\varsigma}_{n+\frac{1}{2}}^h\right)_\Omega - \left(\mathbf{w}^h, \rho_{n+\frac{1}{2}}^h \mathbf{b}\right)_\Omega = 0,
\end{aligned} \tag{152}$$

$$\begin{aligned}
&\mathbf{B}^E(w_5^h; \mathbf{Y}_{n+1}^h) := \left(w_5^h, \frac{[\rho_n^h E(\rho_n^h, \mathbf{u}_n^h, \theta_n^h)]}{\Delta t_n}\right)_\Omega - \left(\nabla w_5^h, \left(\rho_{n+\frac{1}{2}}^h V_{n+\frac{1}{2}}^h \theta_{n+\frac{1}{2}}^h\right.\right. \\
&\left.\left.- \theta_{n+\frac{1}{2}}^h H_{n+\frac{1}{2}}^h + \frac{1}{2\,\mathrm{We}}|\nabla \rho_{n+\frac{1}{2}}^h|^2 + \frac{1}{\mathrm{We}}\rho_{n+\frac{1}{2}}^h \theta_{n+\frac{1}{2}}^h \nabla \cdot \left(\frac{\nabla \rho_{n+\frac{1}{2}}^h}{\theta_{n+\frac{1}{2}}^h}\right) + \rho_{n+\frac{1}{2}}^h |\mathbf{u}_{n+\frac{1}{2}}^h|^2\right) \mathbf{u}_{n+\frac{1}{2}}^h\right)_\Omega \\
&+ \left(\nabla w_5^h, \boldsymbol{\tau}_{n+\frac{1}{2}}^h \mathbf{u}_{n+\frac{1}{2}}^h\right)_\Omega + \left(\nabla w_5^h, \boldsymbol{\varsigma}_{n+\frac{1}{2}}^h \mathbf{u}_{n+\frac{1}{2}}^h\right)_\Omega - \left(\nabla w_5^h, \mathbf{q}_{n+\frac{1}{2}}^h\right)_\Omega - \left(\nabla w_5^h, \boldsymbol{\Pi}_{n+\frac{1}{2}}^h\right)_\Omega \\
&- \left(w_5^h, \rho_{n+\frac{1}{2}}^h \mathbf{b} \cdot \mathbf{u}_{n+\frac{1}{2}}^h\right)_\Omega - \left(w_5^h, \rho_{n+\frac{1}{2}}^h r\right)_\Omega = 0,
\end{aligned} \tag{153}$$

$$\begin{aligned}
&\mathbf{B}^A(w_6^h; \mathbf{Y}_{n+1}^h) := \left(w_6^h, V_{n+\frac{1}{2}}^h\right)_\Omega - \left(w_6^h, \frac{1}{\theta_{n+\frac{1}{2}}^h}\left(\frac{1}{2}\left(\nu_{loc}(\rho_n^h, \theta_{n+\frac{1}{2}}^h) + \nu_{loc}(\rho_{n+1}^h, \theta_{n+\frac{1}{2}}^h)\right)\right.\right. \\
&\left.\left.- \frac{[\![\rho_n^h]\!]^2}{12}\frac{\partial^2 \nu_{loc}}{\partial \rho^2}(\rho_n^h, \theta_{n+\frac{1}{2}}^h)\right)\right)_\Omega + \left(w_6^h, \frac{1}{\theta_{n+\frac{1}{2}}^h}\frac{\mathbf{u}_n^h \cdot \mathbf{u}_{n+1}^h}{2}\right)_\Omega - \left(\nabla w_6^h, \frac{\nabla \rho_{n+\frac{1}{2}}^h}{\mathrm{We}\,\theta_{n+\frac{1}{2}}^h}\right)_\Omega = 0,
\end{aligned} \tag{154}$$

wherein

$$\mathbf{Y}_{n+\frac{1}{2}}^h := \frac{1}{2}\left(\mathbf{Y}_n^h + \mathbf{Y}_{n+1}^h\right), \tag{155}$$

$$\rho_{n+\frac{1}{2}}^h := \rho^h(\mathbf{Y}_{n+\frac{1}{2}}^h), \tag{156}$$

$$\mathbf{u}_{n+\frac{1}{2}}^h := \mathbf{u}^h(\mathbf{Y}_{n+\frac{1}{2}}^h), \tag{157}$$

$$\theta_{n+\frac{1}{2}}^h := \theta^h(\mathbf{Y}_{n+\frac{1}{2}}^h), \tag{158}$$

$$\boldsymbol{\tau}_{n+\frac{1}{2}}^h := \frac{1}{\mathrm{Re}}\left(\nabla \mathbf{u}_{n+\frac{1}{2}}^h + \left(\nabla \mathbf{u}_{n+\frac{1}{2}}^h\right)^T - \frac{2}{3}\nabla \cdot \mathbf{u}_{n+\frac{1}{2}}^h \mathbf{I}\right), \tag{159}$$

$$\boldsymbol{\varsigma}_{n+\frac{1}{2}}^h := \frac{1}{\mathrm{We}}\left(\left(\rho_{n+\frac{1}{2}}^h \Delta \rho_{n+\frac{1}{2}}^h + \frac{1}{2}|\nabla \rho_{n+\frac{1}{2}}^h|^2\right)\mathbf{I} - \nabla \rho_{n+\frac{1}{2}}^h \otimes \nabla \rho_{n+\frac{1}{2}}^h\right), \tag{160}$$

$$\mathbf{q}_{n+\frac{1}{2}}^h := -\kappa \nabla \theta_{n+\frac{1}{2}}^h, \tag{161}$$

$$\mathbf{\Pi} := \frac{1}{\mathrm{We}} \rho^h_{n+\frac{1}{2}} \nabla \cdot \mathbf{u}^h_{n+\frac{1}{2}} \nabla \rho^h_{n+\frac{1}{2}}, \tag{162}$$

$$H^h_{n+\frac{1}{2}} := \frac{8}{27} \rho^h_{n+\frac{1}{2}} \left(\log \left(\frac{\rho^h_{n+\frac{1}{2}}}{1 - \rho^h_{n+\frac{1}{2}}} \right) - \frac{1}{\gamma - 1} \log(\theta^h_{n+\frac{1}{2}}) \right). \tag{163}$$

3.7.2 Preliminary lemmas

We state and prove five lemmas in this section, which will be applied to prove the final results in Section 3.7.3.

Lemma 3. *The mathematical entropy function* $H(\rho, \theta)$ *given by* (103) *satisfies*

$$\frac{\partial^3 H}{\partial \theta^3} < 0. \tag{164}$$

Proof. Straightforward calculations lead to

$$\frac{\partial^3 H}{\partial \theta^3} = -\frac{16}{27(\gamma - 1)} \frac{\rho}{\theta^3}.$$

The dimensionless temperature θ is always positive and the heat capacity ratio γ is always greater than 1. Hence,

$$\frac{\partial^3 H}{\partial \theta^3} < 0.$$

□

Lemma 4. *The local electrochemical potential* $\nu_{loc}(\rho, \theta)$ *given by* (101) *satisfies*

$$\frac{\partial^3 \nu_{loc}}{\partial \rho^3} > 0. \tag{165}$$

Proof. Direct calculations yield

$$\frac{\partial^3 \nu_{loc}}{\partial \rho^3} = \frac{16\theta}{27} \frac{6\rho^2 - 4\rho + 1}{\rho^3 (1 - \rho)^4}.$$

It is known that $\theta > 0$ and $6\rho^2 - 4\rho + 1 \geq 1/3$. Therefore, one has

$$\frac{\partial^3 \nu_{loc}}{\partial \rho^3} > 0.$$

□

Lemma 5. *(Perturbed trapezoidal rules) For a function $f \in C^3([m,n])$, where $m, n \in \mathbb{R}$, there exist $\xi_1, \xi_2 \in (m,n)$ such that the following quadrature formulas hold true.*

$$\int_m^n f(x)dx = \frac{n-m}{2}\left(f(m)+f(n)\right) - \frac{(n-m)^3}{12} f^{''}(m) - \frac{(n-m)^4}{24} f^{'''}(\xi_1), \tag{166}$$

$$\int_m^n f(x)dx = \frac{n-m}{2}\left(f(m)+f(n)\right) - \frac{(n-m)^3}{12} f^{''}(n) + \frac{(n-m)^4}{24} f^{'''}(\xi_2). \tag{167}$$

The proof for this lemma can be found in the appendix of [24]. There are two other suites of quadrature formulas – the rectangular quadrature rules and the perturbed mid-point rules. Interested readers are referred to [44, 42] for details about these formulas and applications. A common feature of these formulas is that each pair contains *opposite* signs in the asymptotic residual terms. This allows one to perform a split of the target function and construct a discrete scheme with a controllable residual. This technique will be demonstrated in the following lemma.

Lemma 6. *Given $[\![\rho_n^h]\!]$, $[\![\rho_n^h \mathbf{u}_n^h]\!]$, and $[\rho_n^h E(\rho_n^h, \mathbf{u}_n^h, \theta_n^h)]$ defined in (143)-(145), the following relation holds for $\xi_1, \xi_2 \in (0,1)$.*

$$\begin{aligned}
&\left(\frac{[\![\rho_n^h]\!]}{\Delta t_n}, \frac{1}{\theta^h_{n+\frac{1}{2}}} \left(\frac{1}{2}\left(\nu_{loc}(\rho_n^h, \theta^h_{n+\frac{1}{2}}) + \nu_{loc}(\rho^h_{n+1}, \theta^h_{n+\frac{1}{2}}) \right) - \frac{[\![\rho_n^h]\!]^2}{12} \frac{\partial^2 \nu_{loc}}{\partial \rho^2}(\rho_n^h, \theta^h_{n+\frac{1}{2}}) \right) \right)_\Omega \\
&- \left(\frac{[\![\rho_n^h]\!]}{\Delta t_n}, \frac{\mathbf{u}^h_{n+1} \cdot \mathbf{u}^h_n}{2\theta^h_{n+\frac{1}{2}}} \right)_\Omega + \left(\nabla \frac{[\![\rho_n^h]\!]}{\Delta t_n}, \frac{1}{\mathrm{We}\, \theta^h_{n+\frac{1}{2}}} \nabla \rho^h_{n+\frac{1}{2}} \right)_\Omega + \left(\frac{\mathbf{u}^h_{n+\frac{1}{2}}}{\theta^h_{n+\frac{1}{2}}}, \frac{[\![\rho_n^h \mathbf{u}_n^h]\!]}{\Delta t_n} \right)_\Omega \\
&- \left(\frac{1}{\theta^h_{n+\frac{1}{2}}}, \frac{[\rho_n^h E(\rho_n^h, \mathbf{u}_n^h, \theta_n^h)]}{\Delta t_n} \right)_\Omega \\
= &\int_\Omega \frac{H(\rho^h_{n+1}, \theta^h_{n+1}) - H(\rho^h_n, \theta^h_n)}{\Delta t_n} dV_{\mathbf{x}} + \left(\frac{1}{\theta^h_{n+\frac{1}{2}} \Delta t_n}, \frac{[\![\rho_n^h]\!]^4}{24} \frac{\partial^3 \nu_{loc}}{\partial \rho^{h3}}(\rho^h_{n+\xi_1}, \theta^h_{n+\frac{1}{2}}) \right)_\Omega \\
&- \left(\frac{1}{\theta^h_{n+\frac{1}{2}} \Delta t_n}, \frac{[\![\theta_n^h]\!]^4}{24} \frac{\partial^3 H}{\partial \theta^{h3}}(\rho^h_{n+\frac{1}{2}}, \theta^h_{n+\xi_2}) \right)_\Omega .
\end{aligned} \tag{168}$$

Proof. Direct calculations can shown that

$$\left(\nabla \frac{[\![\rho_n^h]\!]}{\Delta t_n}, \frac{1}{\mathrm{We}\, \theta^h_{n+\frac{1}{2}}} \nabla \rho^h_{n+\frac{1}{2}} \right)_\Omega = \int_\Omega \frac{|\nabla \rho^h_{n+1}|^2 - |\nabla \rho^h_n|^2}{2\,\mathrm{We}\, \theta^h_{n+\frac{1}{2}} \Delta t_n} dV_{\mathbf{x}},$$

and

$$\left(\mathbf{u}^h_{n+\frac{1}{2}}, \llbracket \rho^h_n \mathbf{u}^h_n \rrbracket\right)_\Omega - \left(\llbracket \rho^h_n \rrbracket, \frac{1}{2}\mathbf{u}^h_{n+1} \cdot \mathbf{u}^h_n\right)_\Omega = \int_\Omega \frac{1}{2}\left(\rho^h_{n+1}|\mathbf{u}^h_{n+1}|^2 - \rho^h_n|\mathbf{u}^h_n|^2\right) dV_{\mathbf{x}}.$$

Making use of the above two relations, one can get

$$\begin{aligned}
&\left(\frac{\llbracket \rho^h_n \rrbracket}{\Delta t_n}, \frac{1}{\theta^h_{n+\frac{1}{2}}}\left(\frac{1}{2}\left(\nu_{loc}(\rho^h_n, \theta^h_{n+\frac{1}{2}}) + \nu_{loc}(\rho^h_{n+1}, \theta^h_{n+\frac{1}{2}})\right) - \frac{\llbracket \rho^h_n \rrbracket^2}{12}\frac{\partial^2 \nu_{loc}}{\partial \rho^{h2}}(\rho^h_n, \theta^h_{n+\frac{1}{2}})\right)\right)_\Omega \\
&- \left(\frac{\llbracket \rho^h_n \rrbracket}{\Delta t_n}, \frac{\mathbf{u}^h_{n+1} \cdot \mathbf{u}^h_n}{2\theta^h_{n+\frac{1}{2}}}\right)_\Omega + \left(\nabla \frac{\llbracket \rho^h_n \rrbracket}{\Delta t_n}, \frac{1}{\mathrm{We}\,\theta^h_{n+\frac{1}{2}}}\nabla \rho^h_{n+\frac{1}{2}}\right)_\Omega + \left(\frac{\mathbf{u}^h_{n+\frac{1}{2}}}{\theta^h_{n+\frac{1}{2}}}, \frac{\llbracket \rho^h_n \mathbf{u}^h_n \rrbracket}{\Delta t_n}\right)_\Omega \\
&- \left(\frac{1}{\theta^h_{n+\frac{1}{2}}}, \frac{[\rho^h_n E(\rho^h_n, \mathbf{u}^h_n, \theta^h_n)]}{\Delta t_n}\right)_\Omega \\
=&\left(\frac{\llbracket \rho^h_n \rrbracket}{\Delta t_n}, \frac{1}{\theta^h_{n+\frac{1}{2}}}\left(\frac{1}{2}\left(\nu_{loc}(\rho^h_n, \theta^h_{n+\frac{1}{2}}) + \nu_{loc}(\rho^h_{n+1}, \theta^h_{n+\frac{1}{2}})\right) - \frac{\llbracket \rho^h_n \rrbracket^2}{12}\frac{\partial^2 \nu_{loc}}{\partial \rho^2}(\rho^h_n, \theta^h_{n+\frac{1}{2}})\right)\right)_\Omega \\
&- \left(\frac{1}{\theta^h_{n+\frac{1}{2}}\Delta t_n}, (\rho\Psi_{loc})(\rho^h_{n+\frac{1}{2}}, \theta^h_{n+1}) - (\rho\Psi_{loc})(\rho^h_{n+\frac{1}{2}}, \theta^h_n) + (\rho\Psi_{loc})(\rho^h_{n+1}, \theta^h_{n+\frac{1}{2}})\right. \\
&- (\rho\Psi_{loc})(\rho^h_n, \theta^h_{n+\frac{1}{2}}) - \theta^h_{n+\frac{1}{2}}\left(H(\rho^h_{n+1}, \theta^h_{n+1}) - H(\rho^h_n, \theta^h_n)\right) \\
&\left.- \frac{\llbracket \theta^h_n \rrbracket}{2}\left(H(\rho^h_{n+\frac{1}{2}}, \theta^h_{n+1}) + H(\rho^h_{n+\frac{1}{2}}, \theta^h_n)\right) + \frac{\llbracket \theta^h_n \rrbracket^3}{12}\frac{\partial^2 H}{\partial \theta^2}(\rho^h_{n+\frac{1}{2}}, \theta^h_{n+1})\right)_\Omega.
\end{aligned} \tag{169}$$

Applying the perturbed trapezoidal rule (166) to

$$\nu_{loc} = \frac{\partial(\rho\Psi_{loc})}{\partial \rho},$$

one can get

$$\begin{aligned}
&(\rho\Psi_{loc})(\rho^h_{n+1}, \theta^h_{n+\frac{1}{2}}) - (\rho\Psi_{loc})(\rho^h_n, \theta^h_{n+\frac{1}{2}}) = \int_{\rho^h_n}^{\rho^h_{n+1}} \frac{\partial(\rho\Psi_{loc})}{\partial \rho} d\rho = \int_{\rho^h_n}^{\rho^h_{n+1}} \nu_{loc} d\rho \\
=&\frac{\llbracket \rho^h_n \rrbracket}{2}\left(\nu_{loc}(\rho^h_n, \theta^h_{n+\frac{1}{2}}) + \nu_{loc}(\rho^h_{n+1}, \theta^h_{n+\frac{1}{2}})\right) - \frac{\llbracket \rho^h_n \rrbracket^3}{12}\frac{\partial^2 \nu_{loc}}{\partial \rho^2}(\rho^h_n, \theta^h_{n+\frac{1}{2}}) - \frac{\llbracket \rho^h_n \rrbracket^4}{24}\frac{\partial^3 \nu_{loc}}{\partial \rho^3}(\rho^h_{n+\xi_1}, \theta^h_{n+\frac{1}{2}}),
\end{aligned}$$

for $\xi_1 \in (0,1)$. Consequently, the relation (169) can be rewritten as

$$\begin{aligned}
&\left(\frac{[\![\rho_n^h]\!]}{\Delta t_n}, \frac{1}{\theta_{n+\frac{1}{2}}^h}\left(\frac{1}{2}\left(\nu_{loc}(\rho_n^h, \theta_{n+\frac{1}{2}}^h) + \nu_{loc}(\rho_{n+1}^h, \theta_{n+\frac{1}{2}}^h)\right) - \frac{[\![\rho_n^h]\!]^2}{12}\frac{\partial^2 \nu_{loc}}{\partial \rho^2}(\rho_n^h, \theta_{n+\frac{1}{2}}^h)\right)\right)_\Omega \\
&- \left(\frac{[\![\rho_n^h]\!]}{\Delta t_n}, \frac{\mathbf{u}_{n+1}^h \cdot \mathbf{u}_n^h}{2\theta_{n+\frac{1}{2}}^h}\right)_\Omega + \left(\nabla \frac{[\![\rho_n^h]\!]}{\Delta t_n}, \frac{1}{\mathrm{We}\,\theta_{n+\frac{1}{2}}^h}\nabla \rho_{n+\frac{1}{2}}^h\right)_\Omega + \left(\frac{\mathbf{u}_{n+\frac{1}{2}}^h}{\theta_{n+\frac{1}{2}}^h}, \frac{[\![\rho_n^h \mathbf{u}_n^h]\!]}{\Delta t_n}\right)_\Omega \\
&- \left(\frac{1}{\theta_{n+\frac{1}{2}}^h}, \frac{[\rho_n^h E(\rho_n^h, \mathbf{u}_n^h, \theta_n^h)]}{\Delta t_n}\right)_\Omega \\
=&\left(\frac{1}{\Delta t_n \theta_{n+\frac{1}{2}}^h}, \frac{[\![\rho_n^h]\!]^4}{24}\frac{\partial^3 \nu_{loc}}{\partial \rho^3}(\rho_{n+\xi_1}^h, \theta_{n+\frac{1}{2}}^h)\right)_\Omega - \left(\frac{1}{\theta_{n+\frac{1}{2}}^h \Delta t_n}, (\rho\Psi_{loc})(\rho_{n+\frac{1}{2}}^h, \theta_{n+1}^h)\right. \\
&- (\rho\Psi_{loc})(\rho_{n+\frac{1}{2}}^h, \theta_n^h) - \theta_{n+\frac{1}{2}}^h\left(H(\rho_{n+1}^h, \theta_{n+1}^h) - H(\rho_n^h, \theta_n^h)\right) \\
&\left. - \frac{[\![\theta_n^h]\!]}{2}\left(H(\rho_{n+\frac{1}{2}}^h, \theta_{n+1}^h) + H(\rho_{n+\frac{1}{2}}^h, \theta_n^h)\right) + \frac{[\![\theta_n^h]\!]^3}{12}\frac{\partial^2 H}{\partial \theta^2}(\rho_{n+\frac{1}{2}}^h, \theta_{n+1}^h)\right)_\Omega. \qquad (170)
\end{aligned}$$

Next, applying the perturbed trapezoidal rule (167) to

$$H = \frac{\partial(\rho\Psi_{loc})}{\partial\theta}$$

leads to

$$\begin{aligned}
&(\rho\Psi_{loc})(\rho_{n+\frac{1}{2}}^h, \theta_{n+1}^h) - (\rho\Psi_{loc})(\rho_{n+\frac{1}{2}}^h, \theta_n^h) = \int_{\theta_n^h}^{\theta_{n+1}^h} \frac{\partial(\rho\Psi_{loc})}{\partial\theta} d\theta = \int_{\theta_n^h}^{\theta_{n+1}^h} H d\theta \\
=&\frac{[\![\theta_n^h]\!]}{2}\left(H(\rho_{n+\frac{1}{2}}^h, \theta_{n+1}^h) + H(\rho_{n+\frac{1}{2}}^h, \theta_n^h)\right) - \frac{[\![\theta_n^h]\!]^3}{12}\frac{\partial^2 H}{\partial\theta^2}(\rho_{n+\frac{1}{2}}^h, \theta_{n+1}^h) + \frac{[\![\theta_n^h]\!]^4}{24}\frac{\partial^3 H}{\partial\theta^3}(\rho_{n+\frac{1}{2}}^h, \theta_{n+\xi_2}^h),
\end{aligned}$$

for $\xi_2 \in (0,1)$. Using the above relation, relation (170) can be further rewritten as

$$\begin{aligned}
&\left(\frac{[\![\rho_n^h]\!]}{\Delta t_n}, \frac{1}{\theta_{n+\frac{1}{2}}^h}\left(\frac{1}{2}\left(\nu_{loc}(\rho_n^h, \theta_{n+\frac{1}{2}}^h) + \nu_{loc}(\rho_{n+1}^h, \theta_{n+\frac{1}{2}}^h)\right) - \frac{[\![\rho_n^h]\!]^2}{12}\frac{\partial^2 \nu_{loc}}{\partial \rho^2}(\rho_n^h, \theta_{n+\frac{1}{2}}^h)\right)\right)_\Omega \\
&- \left(\frac{[\![\rho_n^h]\!]}{\Delta t_n}, \frac{\mathbf{u}_{n+1}^h \cdot \mathbf{u}_n^h}{2\theta_{n+\frac{1}{2}}^h}\right)_\Omega + \left(\nabla \frac{[\![\rho_n^h]\!]}{\Delta t_n}, \frac{1}{\mathrm{We}\,\theta_{n+\frac{1}{2}}^h}\nabla \rho_{n+\frac{1}{2}}^h\right)_\Omega + \left(\frac{\mathbf{u}_{n+\frac{1}{2}}^h}{\theta_{n+\frac{1}{2}}^h}, \frac{[\![\rho_n^h \mathbf{u}_n^h]\!]}{\Delta t_n}\right)_\Omega \\
&- \left(\frac{1}{\theta_{n+\frac{1}{2}}^h}, \frac{[\rho_n^h E(\rho_n^h, \mathbf{u}_n^h, \theta_n^h)]}{\Delta t_n}\right)_\Omega \\
=&\left(\frac{1}{\Delta t_n \theta_{n+\frac{1}{2}}^h}, \frac{[\![\rho_n^h]\!]^4}{24}\frac{\partial^3 \nu_{loc}}{\partial \rho^3}(\rho_{n+\xi_1}^h, \theta_{n+\frac{1}{2}}^h)\right)_\Omega + \left(\frac{1}{\Delta t_n}, \left(H(\rho_{n+1}^h, \theta_{n+1}^h) - H(\rho_n^h, \theta_n^h)\right)\right)_\Omega
\end{aligned}$$

$$
\begin{aligned}
&-\left(\frac{1}{\theta^h_{n+\frac{1}{2}}\Delta t_n}, \frac{[\![\theta^h_n]\!]^4}{24}\frac{\partial^3 H}{\partial \theta^3}(\rho^h_{n+\frac{1}{2}}, \theta^h_{n+\xi_2})\right)_\Omega \\
=&\int_\Omega \frac{H(\rho^h_{n+1}, \theta^h_{n+1}) - H(\rho^h_n, \theta^h_n)}{\Delta t_n} dV_{\mathbf{x}} + \left(\frac{1}{\theta^h_{n+\frac{1}{2}}\Delta t_n}, \frac{[\![\rho^h_n]\!]^4}{24}\frac{\partial^3 \nu_{loc}}{\partial \rho^3}(\rho^h_{n+\xi_1}, \theta^h_{n+\frac{1}{2}})\right)_\Omega \\
&-\left(\frac{1}{\theta^h_{n+\frac{1}{2}}\Delta t_n}, \frac{[\![\theta^h_n]\!]^4}{24}\frac{\partial^3 H}{\partial \theta^3}(\rho^h_{n+\frac{1}{2}}, \theta^h_{n+\xi_2})\right)_\Omega .
\end{aligned}
$$

This completes the proof of Lemma 6. ☐

Remark 14. *Based on Lemmas 3 and 4, one can show that the last two terms in* (168) *satisfy*

$$
\begin{aligned}
\left(\frac{1}{\theta^h_{n+\frac{1}{2}}\Delta t_n}, \frac{[\![\rho^h_n]\!]^4}{24}\frac{\partial^3 \nu_{loc}}{\partial \rho^3}(\rho^h_{n+\xi_1}, \theta^h_{n+\frac{1}{2}})\right)_\Omega &\geq 0, \\
\left(\frac{1}{\theta^h_{n+\frac{1}{2}}\Delta t_n}, \frac{[\![\theta^h_n]\!]^4}{24}\frac{\partial^3 H}{\partial \theta^3}(\rho^h_{n+\frac{1}{2}}, \theta^h_{n+\xi_2})\right)_\Omega &\leq 0.
\end{aligned}
$$

The two terms represent the numerical dissipation introduced by the approximation of time derivatives.

Remark 15. *In the proof of Lemma 6, it is clear that the novel jump operator* (145) *is designed based on the perturbed trapezoidal formulas* (166) *and* (167)*. It should be pointed out that one may construct different discrete jump operators for $\partial(\rho E)/\partial t$ by using the perturbed mid-point rules or the rectangular quadrature rules proposed in [44]. The resulting schemes can be shown to guarantee the dissipation property, but the amount of numerical dissipation will be slightly different.*

Lemma 7. *Replacing ρ^h_n, $\mathbf{u}^h_n$, and θ^h_n in the definition* (145) *with corresponding time continuous functions $\rho^h(t_n)$, $\mathbf{u}^h(t_n)$, and $\theta^h(t_n)$ and assuming sufficient smoothness in the time direction, one has*

$$
\begin{aligned}
&[\rho^h(t_n)E(\rho^h(t_n), \mathbf{u}^h(t_n), \theta^h(t_n))] \\
=&\Big(\rho^h(t_{n+1})E(\rho^h(t_{n+1}), \mathbf{u}^h(t_{n+1}), \theta^h(t_{n+1})) - \rho^h(t_n)E(\rho^h(t_n), \mathbf{u}^h(t_n), \theta^h(t_n))\Big) + \mathcal{O}(\Delta t^3).
\end{aligned}
$$

Proof. Recalling the relations (146)-(150), we only need to analyze the non-classical jump operators (147) and (148). We consider the jump operator (147) first. Taylor expansions lead to

$$\begin{aligned}
(\rho\Psi_{loc})(\rho^h(t_{n+1}),\theta^h(t_{n+1})) &= (\rho\Psi_{loc})(\rho^h(t_{n+\frac{1}{2}}),\theta^h(t_{n+\frac{1}{2}})) \\
&+ \frac{\partial(\rho\Psi_{loc})}{\partial\rho}(\rho^h(t_{n+\frac{1}{2}}),\theta^h(t_{n+\frac{1}{2}}))\left(\rho^h(t_{n+1})-\rho^h(t_{n+\frac{1}{2}})\right) \\
&+ \frac{\partial(\rho\Psi_{loc})}{\partial\theta}(\rho^h(t_{n+\frac{1}{2}}),\theta^h(t_{n+\frac{1}{2}}))\left(\theta^h(t_{n+1})-\theta^h(t_{n+\frac{1}{2}})\right) \\
&+ \frac{1}{2}\frac{\partial^2(\rho\Psi_{loc})}{\partial\rho^2}(\rho^h(t_{n+\frac{1}{2}}),\theta^h(t_{n+\frac{1}{2}}))\left(\rho^h(t_{n+1})-\rho^h(t_{n+\frac{1}{2}})\right)^2 \\
&+ \frac{1}{2}\frac{\partial^2(\rho\Psi_{loc})}{\partial\theta^2}(\rho^h(t_{n+\frac{1}{2}}),\theta^h(t_{n+\frac{1}{2}}))\left(\theta^h(t_{n+1})-\theta^h(t_{n+\frac{1}{2}})\right)^2 \\
&+ \frac{\partial^2(\rho\Psi_{loc})}{\partial\rho\partial\theta}(\rho^h(t_{n+\frac{1}{2}}),\theta^h(t_{n+\frac{1}{2}}))\left(\rho^h(t_{n+1})-\rho^h(t_{n+\frac{1}{2}})\right) \\
&\left(\theta^h(t_{n+1})-\theta^h(t_{n+\frac{1}{2}})\right) \\
&+ \mathcal{O}(\Delta t^3), \qquad (171)
\end{aligned}$$

$$\begin{aligned}
(\rho\Psi_{loc})(\rho^h(t_n),\theta^h(t_n)) &= (\rho\Psi_{loc})(\rho^h(t_{n+\frac{1}{2}}),\theta^h(t_{n+\frac{1}{2}})) \\
&+ \frac{\partial(\rho\Psi_{loc})}{\partial\rho}(\rho^h(t_{n+\frac{1}{2}}),\theta^h(t_{n+\frac{1}{2}}))\left(\rho^h(t_n)-\rho^h(t_{n+\frac{1}{2}})\right) \\
&+ \frac{\partial(\rho\Psi_{loc})}{\partial\theta}(\rho^h(t_{n+\frac{1}{2}}),\theta^h(t_{n+\frac{1}{2}}))\left(\theta^h(t_n)-\theta^h(t_{n+\frac{1}{2}})\right) \\
&+ \frac{1}{2}\frac{\partial^2(\rho\Psi_{loc})}{\partial\rho^2}(\rho^h(t_{n+\frac{1}{2}}),\theta^h(t_{n+\frac{1}{2}}))\left(\rho^h(t_n)-\rho^h(t_{n+\frac{1}{2}})\right)^2 \\
&+ \frac{1}{2}\frac{\partial^2(\rho\Psi_{loc})}{\partial\theta^2}(\rho^h(t_{n+\frac{1}{2}}),\theta^h(t_{n+\frac{1}{2}}))\left(\theta^h(t_n)-\theta^h(t_{n+\frac{1}{2}})\right)^2 \\
&+ \frac{\partial^2(\rho\Psi_{loc})}{\partial\rho\partial\theta}(\rho^h(t_{n+\frac{1}{2}}),\theta^h(t_{n+\frac{1}{2}}))\left(\rho^h(t_n)-\rho^h(t_{n+\frac{1}{2}})\right) \\
&\left(\theta^h(t_n)-\theta^h(t_{n+\frac{1}{2}})\right) \\
&+ \mathcal{O}(\Delta t^3), \qquad (172)
\end{aligned}$$

$$\begin{aligned}
(\rho\Psi_{loc})(\rho^h(t_{n+\frac{1}{2}}),\theta^h(t_{n+1})) &= (\rho\Psi_{loc})(\rho^h(t_{n+\frac{1}{2}}),\theta^h(t_{n+\frac{1}{2}})) \\
&+ \frac{\partial(\rho\Psi_{loc})}{\partial\theta}(\rho^h(t_{n+\frac{1}{2}}),\theta^h(t_{n+\frac{1}{2}}))\left(\theta^h(t_{n+1})-\theta^h(t_{n+\frac{1}{2}})\right) \\
&+ \frac{1}{2}\frac{\partial^2(\rho\Psi_{loc})}{\partial\theta^2}(\rho^h(t_{n+\frac{1}{2}}),\theta^h(t_{n+\frac{1}{2}}))\left(\theta^h(t_{n+1})-\theta^h(t_{n+\frac{1}{2}})\right)^2 \\
&+ \mathcal{O}(\Delta t^3), \qquad (173)
\end{aligned}$$

$$\begin{aligned}
(\rho\Psi_{loc})(\rho^h(t_{n+\frac{1}{2}}),\theta^h(t_n)) &= (\rho\Psi_{loc})(\rho^h(t_{n+\frac{1}{2}}),\theta^h(t_{n+\frac{1}{2}})) \\
&+ \frac{\partial(\rho\Psi_{loc})}{\partial\theta}(\rho^h(t_{n+\frac{1}{2}}),\theta^h(t_{n+\frac{1}{2}}))\left(\theta^h(t_n)-\theta^h(t_{n+\frac{1}{2}})\right)
\end{aligned}$$

$$
\begin{aligned}
&+ \frac{1}{2}\frac{\partial^2(\rho\Psi_{loc})}{\partial\theta^2}(\rho^h(t_{n+\frac{1}{2}}),\theta^h(t_{n+\frac{1}{2}}))\left(\theta^h(t_n)-\theta^h(t_{n+\frac{1}{2}})\right)^2 \\
&+ \mathcal{O}(\Delta t^3),
\end{aligned} \tag{174}
$$

$$
\begin{aligned}
(\rho\Psi_{loc})(\rho^h(t_{n+1}),\theta^h(t_{n+\frac{1}{2}})) &= (\rho\Psi_{loc})(\rho^h(t_{n+\frac{1}{2}}),\theta^h(t_{n+\frac{1}{2}})) \\
&+ \frac{\partial(\rho\Psi_{loc})}{\partial\rho}(\rho^h(t_{n+\frac{1}{2}}),\theta^h(t_{n+\frac{1}{2}}))\left(\rho^h(t_{n+1})-\rho^h(t_{n+\frac{1}{2}})\right) \\
&+ \frac{1}{2}\frac{\partial^2(\rho\Psi_{loc})}{\partial\rho^2}(\rho^h(t_{n+\frac{1}{2}}),\theta^h(t_{n+\frac{1}{2}}))\left(\rho^h(t_{n+1})-\rho^h(t_{n+\frac{1}{2}})\right)^2 \\
&+ \mathcal{O}(\Delta t^3),
\end{aligned} \tag{175}
$$

$$
\begin{aligned}
(\rho\Psi_{loc})(\rho^h(t_n),\theta^h(t_{n+\frac{1}{2}})) &= (\rho\Psi_{loc})(\rho^h(t_{n+\frac{1}{2}}),\theta^h(t_{n+\frac{1}{2}})) \\
&+ \frac{\partial(\rho\Psi_{loc})}{\partial\rho}(\rho^h(t_{n+\frac{1}{2}}),\theta^h(t_{n+\frac{1}{2}}))\left(\rho^h(t_n)-\rho^h(t_{n+\frac{1}{2}})\right) \\
&+ \frac{\partial^2(\rho\Psi_{loc})}{\partial\rho^2}(\rho^h(t_{n+\frac{1}{2}}),\theta^h(t_{n+\frac{1}{2}}))\left(\rho^h(t_n)-\rho^h(t_{n+\frac{1}{2}})\right)^2 \\
&+ \mathcal{O}(\Delta t^3).
\end{aligned} \tag{176}
$$

Combining the above Taylor expansions leads to

$$
\begin{aligned}
&\Big((\rho\Psi_{loc})(\rho^h(t_{n+1}),\theta^h(t_{n+1}))-(\rho\Psi_{loc})(\rho^h(t_n),\theta^h(t_n))\Big) \\
&-\Big((\rho\Psi_{loc})(\rho^h(t_{n+\frac{1}{2}}),\theta^h(t_{n+1}))-(\rho\Psi_{loc})(\rho^h(t_{n+\frac{1}{2}}),\theta^h(t_n)) \\
&+(\rho\Psi_{loc})(\rho^h(t_{n+1}),\theta^h(t_{n+\frac{1}{2}}))-(\rho\Psi_{loc})(\rho^h(t_n),\theta^h(t_{n+\frac{1}{2}}))\Big) = \mathcal{O}(\Delta t^3).
\end{aligned}
$$

Next, we analyze the term (148).

$$
\begin{aligned}
&\Big(\theta^h(t_{n+1})H(\rho^h(t_{n+1}),\theta^h(t_{n+1}))-\theta^h(t_n)H(\rho^h(t_n),\theta^h(t_n))\Big) \\
&-\Bigg(\theta^h(t_{n+\frac{1}{2}})\Big(H(\rho^h(t_{n+1}),\theta^h(t_{n+1}))-H(\rho^h(t_n),\theta^h(t_n))\Big) \\
&+\frac{\theta^h(t_{n+1})-\theta^h(t_n)}{2}\Big(H(\rho^h(t_{n+\frac{1}{2}}),\theta^h(t_{n+1}))+H(\rho^h(t_{n+\frac{1}{2}}),\theta^h(t_n))\Big)\Bigg) \\
=&\frac{\theta^h(t_{n+1})-\theta^h(t_n)}{2}\Big(H(\rho^h(t_{n+1}),\theta^h(t_{n+1}))+H(\rho^h(t_n),\theta^h(t_n)) \\
&-H(\rho^h(t_{n+\frac{1}{2}}),\theta^h(t_{n+1}))-H(\rho^h(t_{n+\frac{1}{2}}),\theta^h(t_n))\Big)+\mathcal{O}(\Delta t^3) \\
=&\frac{(\theta^h(t_{n+1})-\theta^h(t_n))}{2}\Bigg(\frac{\partial H}{\partial\rho}(\rho^h(t_{n+\frac{1}{2}}),\theta^h(t_{n+1}))\left(\rho^h(t_{n+1})-\rho^h(t_{n+\frac{1}{2}})\right)
\end{aligned}
$$

$$
\begin{aligned}
&- \frac{\partial H}{\partial \rho}(\rho^h(t_{n+\frac{1}{2}}), \theta^h(t_n)) \left(\rho^h(t_n) - \rho^h(t_{n+\frac{1}{2}})\right) \Bigg) + \mathcal{O}(\Delta t^3) \\
=&\mathcal{O}(\Delta t^3).
\end{aligned} \tag{177}
$$

According to (171) and (177), it can be concluded that

$$
\begin{aligned}
&[\rho^h(t_n) E(\rho^h(t_n), \mathbf{u}^h(t_n), \theta^h(t_n))] \\
&- \left(\rho^h(t_{n+1}) E(\rho^h(t_{n+1}), \mathbf{u}^h(t_{n+1}), \theta^h(t_{n+1})) - \rho^h(t_n) E(\rho^h(t_n), \mathbf{u}^h(t_n), \theta^h(t_n))\right) \\
=&\mathcal{O}(\Delta t^3) + \frac{(\theta^h(t_{n+1}) - \theta^h(t_n))^3}{12} \frac{\partial^2 H}{\partial \theta^2}(\rho^h(t_{n+\frac{1}{2}}), \theta^h(t_{n+1})) \\
=&\mathcal{O}(\Delta t^3).
\end{aligned}
$$

This completes the proof of the lemma. □

This lemma reveals that the jump operator we defined in (145) is in fact a third-order perturbation to the classical energy jump. Using this fact, we can prove the second-order accuracy of our numerical scheme.

3.7.3 Numerical dissipation and accuracy

With the above five lemmas, we are ready to state and prove the main results of the fully discrete scheme (151)-(154).

Theorem 6. *The solutions of the fully discrete scheme* (151)-(154) *satisfy*

$$
\begin{aligned}
&\int_\Omega \Bigg(\frac{H(\rho^h_{n+1}, \theta^h_{n+1}) - H(\rho^h_n, \theta^h_n)}{\Delta t_n} + \nabla \cdot \left(H(\rho^h_{n+\frac{1}{2}}, \theta^h_{n+\frac{1}{2}}) \mathbf{u}^h_{n+\frac{1}{2}} \right) - \nabla \cdot \left(\frac{\mathbf{q}^h_{n+\frac{1}{2}}}{\theta^h_{n+\frac{1}{2}}} \right) \\
&\qquad + \frac{\rho^h_{n+\frac{1}{2}} r}{\theta^h_{n+\frac{1}{2}}} \Bigg) dV_{\mathbf{x}} \\
=& - \int_\Omega \frac{1}{\theta^h_{n+\frac{1}{2}}} \boldsymbol{\tau}^h_{n+\frac{1}{2}} : \nabla \mathbf{u}^h_{n+\frac{1}{2}} dV_{\mathbf{x}} - \int_\Omega \frac{\kappa |\nabla \theta^h_{n+\frac{1}{2}}|^2}{\left(\theta^h_{n+\frac{1}{2}}\right)^2} dV_{\mathbf{x}} \\
&- \int_\Omega \frac{1}{\theta^h_{n+\frac{1}{2}} \Delta t_n} \frac{[\![\rho^h_n]\!]^4}{24} \frac{\partial^3 \nu_{loc}}{\partial \rho^3}(\rho^h_{n+\xi_1}, \theta^h_{n+\frac{1}{2}}) dV_{\mathbf{x}} + \int_\Omega \frac{1}{\theta^h_{n+\frac{1}{2}} \Delta t_n} \frac{[\![\theta^h_n]\!]^4}{24} \frac{\partial^3 H}{\partial \theta^3}(\rho^h_{n+\frac{1}{2}}, \theta^h_{n+\xi_2}) dV_{\mathbf{x}} \\
\leq& 0.
\end{aligned} \tag{178}
$$

Proof. Taking $w^h_1 = V^h_{n+\frac{1}{2}}$ in (151), $\mathbf{w}^h = \mathbf{u}^h_{n+\frac{1}{2}} / \theta^h_{n+\frac{1}{2}}$ in (152), $w^h_5 = -1/\theta^h_{n+\frac{1}{2}}$ in (153), $w^h_6 = [\![\rho^h_n]\!]/\Delta t_n$ in (154), combing the three equations, and following the proof of Theorem

4, one can show that

$$
\begin{aligned}
&\mathbf{B}^M(V^h_{n+\frac{1}{2}};\mathbf{Y}^h_{n+1}) + \mathbf{B}^U(\frac{\mathbf{u}^h_{n+\frac{1}{2}}}{\theta^h_{n+\frac{1}{2}}};\mathbf{Y}^h_{n+1}) + \mathbf{B}^E(-\frac{1}{\theta_{n+\frac{1}{2}}};\mathbf{Y}^h_{n+1}) - \mathbf{B}^A(\frac{[\![\rho^h_n]\!]}{\Delta t_n};\mathbf{Y}^h_{n+1}) \\
=&\left(\frac{[\![\rho^h_n]\!]}{\Delta t_n}, \frac{1}{\theta^h_{n+\frac{1}{2}}}\left(\frac{1}{2}\left(\nu_{loc}(\rho^h_n,\theta^h_{n+\frac{1}{2}}) + \nu_{loc}(\rho^h_{n+1},\theta^h_{n+\frac{1}{2}})\right) - \frac{[\![\rho^h_n]\!]^2}{12}\frac{\partial^2 \nu_{loc}}{\partial \rho^2}(\rho^h_n,\theta^h_{n+\frac{1}{2}})\right)\right)_\Omega \\
&-\left(\frac{[\![\rho^h_n]\!]}{\Delta t_n}, \frac{\mathbf{u}^h_{n+1}\cdot\mathbf{u}^h_n}{2\theta^h_{n+\frac{1}{2}}}\right)_\Omega + \left(\nabla\frac{[\![\rho^h_n]\!]}{\Delta t_n}, \frac{1}{\mathrm{We}\,\theta^h_{n+\frac{1}{2}}}\nabla\rho^h_{n+\frac{1}{2}}\right)_\Omega + \left(\frac{\mathbf{u}^h_{n+\frac{1}{2}}}{\theta^h_{n+\frac{1}{2}}}, \frac{[\![\rho^h_n\mathbf{u}^h_n]\!]}{\Delta t_n}\right)_\Omega \\
&-\left(\frac{1}{\theta^h_{n+\frac{1}{2}}}, \frac{[\rho^h_n E(\rho^h_n,\mathbf{u}^h_n,\theta^h_n)]}{\Delta t_n}\right)_\Omega + \int_\Omega \nabla\cdot\left(H(\rho^h_{n+\frac{1}{2}},\theta^h_{n+\frac{1}{2}})\mathbf{u}^h_{n+\frac{1}{2}}\right)dV_{\mathbf{x}} \\
&+\int_\Omega \nabla\cdot\left(\frac{\mathbf{q}^h_{n+\frac{1}{2}}}{\theta^h_{n+\frac{1}{2}}}\right) - \frac{\rho^h_{n+\frac{1}{2}}r}{\theta_{n+\frac{1}{2}}}dV_{\mathbf{x}} + \int_\Omega \frac{1}{\theta^h_{n+\frac{1}{2}}}\boldsymbol{\tau}^h_{n+\frac{1}{2}} : \nabla\mathbf{u}^h_{n+\frac{1}{2}}dV_{\mathbf{x}} + \int_\Omega \frac{\kappa|\nabla\theta^h_{n+\frac{1}{2}}|^2}{\left(\theta^h_{n+\frac{1}{2}}\right)^2}dV_{\mathbf{x}} \\
&= 0.
\end{aligned}
$$

According to Lemma 6, the above relation can be reorganized as

$$
\begin{aligned}
&\int_\Omega \left(\frac{H(\rho^h_{n+1},\theta^h_{n+1}) - H(\rho^h_n,\theta^h_n)}{\Delta t_n} + \nabla\cdot\left(H(\rho^h_{n+\frac{1}{2}},\theta^h_{n+\frac{1}{2}})\mathbf{u}^h_{n+\frac{1}{2}}\right) - \nabla\cdot\left(\frac{\mathbf{q}^h_{n+\frac{1}{2}}}{\theta^h_{n+\frac{1}{2}}}\right)\right. \\
&\qquad\left. + \frac{\rho^h_{n+\frac{1}{2}}r}{\theta^h_{n+\frac{1}{2}}}\right)dV_{\mathbf{x}} \\
=&-\int_\Omega \frac{1}{\theta^h_{n+\frac{1}{2}}}\boldsymbol{\tau}^h_{n+\frac{1}{2}} : \nabla\mathbf{u}^h_{n+\frac{1}{2}}dV_{\mathbf{x}} - \int_\Omega \frac{\kappa|\nabla\theta^h_{n+\frac{1}{2}}|^2}{\left(\theta^h_{n+\frac{1}{2}}\right)^2}dV_{\mathbf{x}} \\
&-\int_\Omega \frac{1}{\theta^h_{n+\frac{1}{2}}\Delta t_n}\frac{[\![\rho^h_n]\!]^4}{24}\frac{\partial^3\nu_{loc}}{\partial\rho^3}(\rho^h_{n+\xi_1},\theta^h_{n+\frac{1}{2}})dV_{\mathbf{x}} + \int_\Omega \frac{1}{\theta^h_{n+\frac{1}{2}}\Delta t_n}\frac{[\![\theta^h_n]\!]^4}{24}\frac{\partial^3 H}{\partial\theta^3}(\rho^h_{n+\frac{1}{2}},\theta^h_{n+\xi_2})dV_{\mathbf{x}} \\
\le& 0.
\end{aligned}
$$

The last inequality is due to Lemmas 3 and 4. □

Remark 16. *This theorem implies that the fully discrete solutions respect the second law of thermodynamics. The amount of dissipation in* (178) *consists of two parts: the physical dissipation and the numerical dissipation. From our analysis, the numerical dissipation exclusively comes from the temporal scheme, and it will vanish if the time step approaches zero.*

Theorem 7. *The local truncation error in time $\tau(t)$ can be bounded by $|\tau(t)| \leq K\Delta t_n^2$ for all $t_n \in [0,T]$, where K is a constant independent of Δt_n.*

Proof. We start by considering the mid-point rule applied to the semi-discrete formulation (137)-(140). The fully discrete scheme reads

$$
\begin{aligned}
&\mathbf{B}^{M}_{mid}(w^h_1;\mathbf{Y}^h_{n+1}) := \left(w^h_1, \frac{[\![\rho^h_n]\!]}{\Delta t_n}\right)_\Omega - \left(\nabla w^h_1, \rho^h_{n+\frac{1}{2}}\mathbf{u}^h_{n+\frac{1}{2}}\right)_\Omega = 0,\\
&\mathbf{B}^{U}_{mid}(\mathbf{w}^h;\mathbf{Y}^h_{n+1}) := \left(\mathbf{w}^h, \frac{[\![\rho^h_n\mathbf{u}^h_n]\!]}{\Delta t_n}\right)_\Omega - \left(\nabla \mathbf{w}^h, \rho^h_{n+\frac{1}{2}}\mathbf{u}^h_{n+\frac{1}{2}}\otimes\mathbf{u}^h_{n+\frac{1}{2}}\right)_\Omega\\
&-\left(\nabla\cdot\mathbf{w}^h, \rho^h_{n+\frac{1}{2}}V^h_{mid}\theta^h_{n+\frac{1}{2}} + \frac{1}{2}\rho^h_{n+\frac{1}{2}}|\mathbf{u}^h_{n+\frac{1}{2}}|^2 + \frac{1}{\mathrm{We}}\rho^h_{n+\frac{1}{2}}\theta^h_{n+\frac{1}{2}}\nabla\cdot\left(\frac{\nabla\rho^h_{n+\frac{1}{2}}}{\theta^h_{n+\frac{1}{2}}}\right)\right)_\Omega\\
&-\left(\mathbf{w}^h, \left(V^h_{mid}\theta^h_{n+\frac{1}{2}} + \frac{|\mathbf{u}^h_{n+\frac{1}{2}}|^2}{2} + \frac{1}{\mathrm{We}}\theta^h_{n+\frac{1}{2}}\nabla\cdot\left(\frac{\nabla\rho^h_{n+\frac{1}{2}}}{\theta^h_{n+\frac{1}{2}}}\right)\right)\nabla\rho^h_{n+\frac{1}{2}}\right)_\Omega\\
&-\left(\mathbf{w}^h, H^h_{n+\frac{1}{2}}\nabla\theta^h_{n+\frac{1}{2}}\right)_\Omega + \left(\nabla\mathbf{w}^h, \boldsymbol{\tau}^h_{n+\frac{1}{2}}\right)_\Omega + \left(\nabla\mathbf{w}^h_{n+\frac{1}{2}}, \boldsymbol{\varsigma}^h_{n+\frac{1}{2}}\right)_\Omega - \left(\mathbf{w}^h, \rho^h_{n+\frac{1}{2}}\mathbf{b}\right)_\Omega = \mathbf{0},\\
&\mathbf{B}^{E}_{mid}(w^h_5;\mathbf{Y}^h_{n+1}) := \left(w^h_5, \frac{\rho^h_{n+1}E(\rho^h_{n+1},\mathbf{u}^h_{n+1},\theta^h_{n+1}) - \rho^h_nE(\rho^h_n,\mathbf{u}^h_n,\theta^h_n)}{\Delta t_n}\right)_\Omega\\
&-\left(\nabla w^h_5, \left(\rho^hV^h_{mid}\theta^h_{n+\frac{1}{2}} - \theta^h_{n+\frac{1}{2}}H^h_{n+\frac{1}{2}} + \frac{1}{2\,\mathrm{We}}|\nabla\rho^h_{n+\frac{1}{2}}|^2 + \rho^h|\mathbf{u}^h_{n+\frac{1}{2}}|^2\right.\right.\\
&\left.\left.+\frac{1}{\mathrm{We}}\rho^h_{n+\frac{1}{2}}\theta^h_{n+\frac{1}{2}}\nabla\cdot\left(\frac{\nabla\rho^h_{n+\frac{1}{2}}}{\theta^h_{n+\frac{1}{2}}}\right)\right)\mathbf{u}^h_{n+\frac{1}{2}}\right)_\Omega + \left(\nabla w^h_5, \boldsymbol{\tau}^h_{n+\frac{1}{2}}\mathbf{u}^h_{n+\frac{1}{2}}\right)_\Omega + \left(\nabla w^h_5, \boldsymbol{\varsigma}^h_{n+\frac{1}{2}}\mathbf{u}^h_{n+\frac{1}{2}}\right)_\Omega\\
&-\left(\nabla w^h_5, \mathbf{q}^h_{n+\frac{1}{2}}\right)_\Omega - \left(\nabla w^h_5, \boldsymbol{\Pi}^h_{n+\frac{1}{2}}\right)_\Omega - \left(w^h_5, \rho^h_{n+\frac{1}{2}}\mathbf{b}\cdot\mathbf{u}^h_{n+\frac{1}{2}}\right)_\Omega - \left(w^h_5, \rho^h_{n+\frac{1}{2}}r\right)_\Omega = 0,\\
&\mathbf{B}^{A}_{mid}(w^h_6;\mathbf{Y}^h_{n+1}) := \left(w^h_6, V^h_{mid}\right)_\Omega - \left(w^h_6, \frac{1}{\theta^h_{n+\frac{1}{2}}}\left(\nu_{loc}(\rho^h_{n+\frac{1}{2}},\theta^h_{n+\frac{1}{2}}) - \frac{|\mathbf{u}^h_{n+\frac{1}{2}}|^2}{2}\right)\right)_\Omega\\
&-\left(\nabla w^h_6, \frac{1}{\mathrm{We}\,\theta^h_{n+\frac{1}{2}}}\nabla\rho^h_{n+\frac{1}{2}}\right)_\Omega = 0.
\end{aligned}
$$

The local truncation errors associated with the mid-point rule can be obtained by replacing the time discrete solutions with the corresponding exact time continuous solution:

$$
\begin{aligned}
\mathbf{B}^{M}_{mid}(w^h_1;\mathbf{Y}^h(t)) &= \left(w^h_1, \Theta^{mid}_{\rho}\right)_\Omega,\\
\mathbf{B}^{U}_{mid}(\mathbf{w}^h;\mathbf{Y}^h(t)) &= \left(\mathbf{w}^h, \Theta^{mid}_{\mathbf{u}}\right)_\Omega,\\
\mathbf{B}^{E}_{mid}(w^h_5;\mathbf{Y}^h(t)) &= \left(w^h_5, \Theta^{mid}_{E}\right)_\Omega,\\
\mathbf{B}^{A}_{mid}(w^h_6;\mathbf{Y}^h(t)) &= \left(w^h_6, \Theta^{mid}_{A}\right)_\Omega.
\end{aligned}
$$

Assuming sufficient smoothness for the time continuous solutions, one can show that

$$\begin{aligned}
\Theta_\rho^{mid} &= \mathcal{O}(\Delta t_n^2), \quad \Theta_{\mathbf{u}}^{mid} = \mathcal{O}(\Delta t_n^2)\mathbf{1}, \\
\Theta_E^{mid} &= \mathcal{O}(\Delta t_n^2), \quad \Theta_A^{mid} = \mathcal{O}(\Delta t_n^2).
\end{aligned}$$

Now replacing the time discrete solutions with corresponding time continuous solutions in the fully discrete formulation (151)-(154):

$$\begin{aligned}
\mathbf{B}^M(w_1^h; \mathbf{Y}^h(t)) &= \left(w_1^h, \Theta_\rho\right)_\Omega, \\
\mathbf{B}^U(\mathbf{w}^h; \mathbf{Y}^h(t)) &= \left(\mathbf{w}^h, \Theta_{\mathbf{u}}\right)_\Omega, \\
\mathbf{B}^E(w_5^h; \mathbf{Y}^h(t)) &= \left(w_5^h, \Theta_E\right)_\Omega, \\
\mathbf{B}^A(w_6^h; \mathbf{Y}^h(t)) &= \left(w_6^h, \Theta_A\right)_\Omega.
\end{aligned}$$

Taylor expansions lead to

$$\begin{aligned}
\frac{1}{2}\left(\nu_{loc}(\rho^h(t_n), \theta^h(t_{n+\frac{1}{2}})) + \nu_{loc}(\rho^h(t_{n+1}), \theta^h(t_{n+\frac{1}{2}})\right) &= \nu_{loc}(\rho^h(t_{n+\frac{1}{2}}), \theta^h(t_{n+\frac{1}{2}})) + \mathcal{O}(\Delta t_n^2), \\
\frac{[\![\rho^h(t_n)]\!]^2}{12}\frac{\partial^2 \nu_{loc}}{\partial \rho^2}(\rho^h(t_n), \theta^h(t_{n+\frac{1}{2}})) &= \mathcal{O}(\Delta t_n^2), \\
2|\mathbf{u}^h(t_{n+\frac{1}{2}})|^2 - \frac{1}{2}(|\mathbf{u}^h(t_n)|^2 + |\mathbf{u}^h(t_{n+1})|^2) &= |\mathbf{u}^h(t_{n+\frac{1}{2}})|^2 + \mathcal{O}(\Delta t_n^2).
\end{aligned}$$

Due to Lemma 7, one has

$$\frac{\rho_{n+1}^h E(\rho_{n+1}^h, \mathbf{u}_{n+1}^h, \theta_{n+1}^h) - \rho_n^h E(\rho_n^h, \mathbf{u}_n^h, \theta_n^h)}{\Delta t_n} - \frac{[\rho_n^h E(\rho_n^h, \mathbf{u}_n^h, \theta_n^h)]}{\Delta t_n} = \mathcal{O}(\Delta t_n^2).$$

Combing the above results gives us

$$\begin{aligned}
\left(w_1^h, \Theta_\rho\right)_\Omega &= \left(w_1^h, \Theta_\rho^{mid}\right)_\Omega + \mathcal{O}(\Delta t_n^2) = \mathcal{O}(\Delta t_n^2), \\
\left(\mathbf{w}^h, \Theta_{\mathbf{u}}\right)_\Omega &= \left(\mathbf{w}^h, \Theta_{\mathbf{u}}^{mid}\right)_\Omega + \mathcal{O}(\Delta t_n^2)\mathbf{1} = \mathcal{O}(\Delta t_n^2)\mathbf{1}, \\
\left(w_5^h, \Theta_E\right)_\Omega &= \left(w_5^h, \Theta_E^{mid}\right)_\Omega + \mathcal{O}(\Delta t_n) = \mathcal{O}(\Delta t_n^2), \\
\left(w_6^h, \Theta_A\right)_\Omega &= \left(w_6^h, \Theta_A^{mid}\right)_\Omega + \mathcal{O}(\Delta t_n^2) = \mathcal{O}(\Delta t_n^2).
\end{aligned}$$

This completes the proof. □

Remark 17. *According to the proof of Theorem 7, we can see that the fully discrete scheme* (151)-(154) *is a second-order perturbation of the mid-point scheme. This perturbation guarantees the entropy dissipation* (178).

4 Benchmark problems

In this section, we use a suite of benchmark problems to verify the theoretical estimates we made in Section 3.

Table 1: One-dimensional manufactured solution for the thermal Navier-Stokes-Korteweg equations: Temporal convergence rates at $t = 0.5$.

Temporal errors in L^2 norm with polynomial degree $k = 2$

Δt	1.0×10^{-1}	5.0×10^{-2}	1.0×10^{-2}	5.0×10^{-3}	1.0×10^{-3}
$\|Y_1 - Y_1^h\|_{L^2(\Omega)}$	8.00×10^{-4}	1.99×10^{-4}	7.96×10^{-6}	1.99×10^{-6}	7.93×10^{-8}
order	-	2.01	2.00	2.00	2.00
$\|Y_2 - Y_2^h\|_{L^2(\Omega)}$	1.50×10^{-2}	3.77×10^{-3}	1.49×10^{-4}	3.72×10^{-5}	1.48×10^{-6}
order	-	1.99	2.01	2.00	2.00
$\|Y_3 - Y_3^h\|_{L^2(\Omega)}$	6.23×10^{-3}	1.52×10^{-3}	5.95×10^{-5}	1.49×10^{-5}	5.94×10^{-7}
order	-	2.04	2.01	2.00	2.00

Temporal errors in H^1 semi-norm with polynomial degree $k = 3$

Δt	1.0×10^{-1}	5.0×10^{-2}	1.0×10^{-2}	5.0×10^{-3}	1.0×10^{-3}
$\lvert Y_1 - Y_1^h\rvert_{H^1(\Omega)}$	5.03×10^{-3}	1.25×10^{-3}	5.00×10^{-5}	1.25×10^{-5}	5.00×10^{-7}
order	-	2.01	2.00	2.00	2.00
$\lvert Y_2 - Y_2^h\rvert_{H^1(\Omega)}$	9.59×10^{-2}	2.58×10^{-2}	9.84×10^{-4}	2.46×10^{-4}	9.84×10^{-6}
order	-	1.89	2.03	2.00	2.00
$\lvert Y_3 - Y_3^h\rvert_{H^1(\Omega)}$	3.04×10^{-2}	7.70×10^{-3}	2.78×10^{-4}	6.95×10^{-5}	2.78×10^{-6}
order	-	1.98	2.06	2.00	2.00

4.1 Manufactured solutions

As first examples, we construct one-dimensional manufactured solutions for the Navier-Stokes-Korteweg equations to corroborate the time accuracy estimate given in Theorem 7. The computations are restricted to $\Omega = (0, 1)$; the exact density, velocity, and temperature for this problem are chosen as

$$\begin{aligned} \rho(x,t) &= 0.5 + 0.1\sin(\pi t)\cos(2\pi x), \\ \mathbf{u}(x,t) &= \sin(\pi t)\cos(2\pi x), \\ \theta(x,t) &= 0.85 + 0.1\sin(\pi t)\sin(4\pi x). \end{aligned}$$

The forcing terms for the balance equations are obtained by substituting the above exact solutions into the original strong problem (87)-(89). The $\mathbf{Y}$ variables can be obtained as

$$\begin{aligned} Y_1 &= \rho = 0.5 + 0.1 \sin(\pi t) \cos(2\pi x), \\ Y_2 &= \frac{\mathbf{u}}{\theta} = \frac{\sin(\pi t)\cos(2\pi x)}{0.85 + 0.1\sin(\pi t)\sin(4\pi x)}, \\ Y_3 &= -\frac{1}{\theta} = -\frac{1}{0.85 + 0.1\sin(\pi t)\sin(4\pi x)}. \end{aligned}$$

The dimensionless numbers for this verification problem are fixed to be Re = 1.0, We = 1.0, and $\gamma = 1.333$. The dimensionless thermal conductivity is chosen as $\kappa = 1.0$. Periodic boundary conditions are enforced for all variables. The problem is computed with spatial mesh size $\Delta x = 1.0 \times 10^{-3}$ for polynomial degrees $k = 2$ and 3. The time step sizes are taken as 1.0×10^{-1}, 5.0×10^{-2}, 1.0×10^{-2}, 5.0×10^{-3}, and 5.0×10^{-4}. In Table 1, the errors in L^2-norm for the quadratic NURBS solutions and the errors in H^1 semi-norm for the cubic NURBS solutions are summarized. It can be observed that the temporal errors converge like $\mathcal{O}(\Delta t^2)$ in both cases. This confirms the time accuracy estimate given in Theorem 7.

4.2 Coalescence of two vapor bubbles

In this example, we consider a one-dimensional problem with zero sources (i.e., $\mathbf{b} = \mathbf{0}$ and $r = 0$) to verify the entropy dissipation estimate given in Theorem 6. The computational domain is set to be $\Omega = (0, 1)$. The initial conditions consist of two static vapor bubbles with centers at points $C_1 = 0.39$ and $C_2 = 0.61$. The radii of the bubbles are set to be $R_1 = R_2 = 0.1$. The initial density is given by the following hyperbolic tangent function.

$$\begin{aligned} \rho_0(\mathbf{x}) &= 0.1 + 0.25 \left[\tanh\left(\frac{d_1(\mathbf{x}) - R_1}{2} \sqrt{\mathrm{We}} \right) + \tanh\left(\frac{d_2(\mathbf{x}) - R_2}{2} \sqrt{\mathrm{We}} \right) \right], \\ d_i(\mathbf{x}) &= |\mathbf{x} - C_i|, \quad \text{for } i = 1, 2. \end{aligned}$$

The initial velocity is zero and the initial temperature is $\theta_0 = 0.95$. Periodic boundary conditions are applied for all variables. The dimensionless numbers are taken as Re $= 4.0 \times 10^2$, We $= 1.6 \times 10^5$, and $\gamma = 1.333$; the dimensionless thermal conductivity is taken as $\kappa = 1.0$. The spatial mesh consists of 10^4 quadratic NURBS functions. The problem is integrated up to $T = 10.0$ with time step sizes $\Delta t = 1.0 \times 10^{-2}$, 5.0×10^{-3}, 2.0×10^{-3}, and 1.0×10^{-5}.

The two vapor bubbles will merge together to minimize the surface energy. At the temperature $\theta = 0.95$, the energetically stable liquid and vapor densities are 0.487 and 0.193

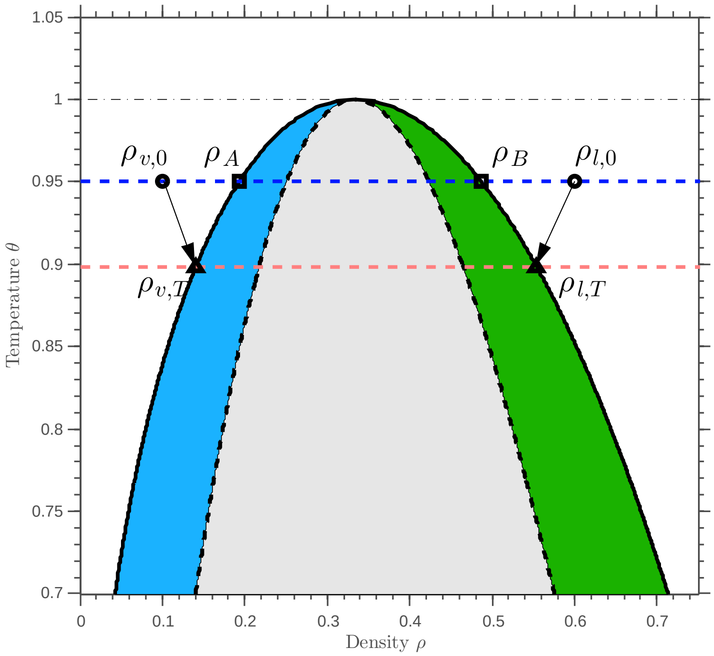

Figure 6: Illustration of the thermal bubble dynamics. $\rho_{v,0}$ and $\rho_{l,0}$ are the initial vapor and liquid densities; ρ_A and ρ_B are the Maxwell state at the initial temperature; $\rho_{v,T}$ and $\rho_{l,T}$ are the vapor and liquid densities at time $T = 10.0$.

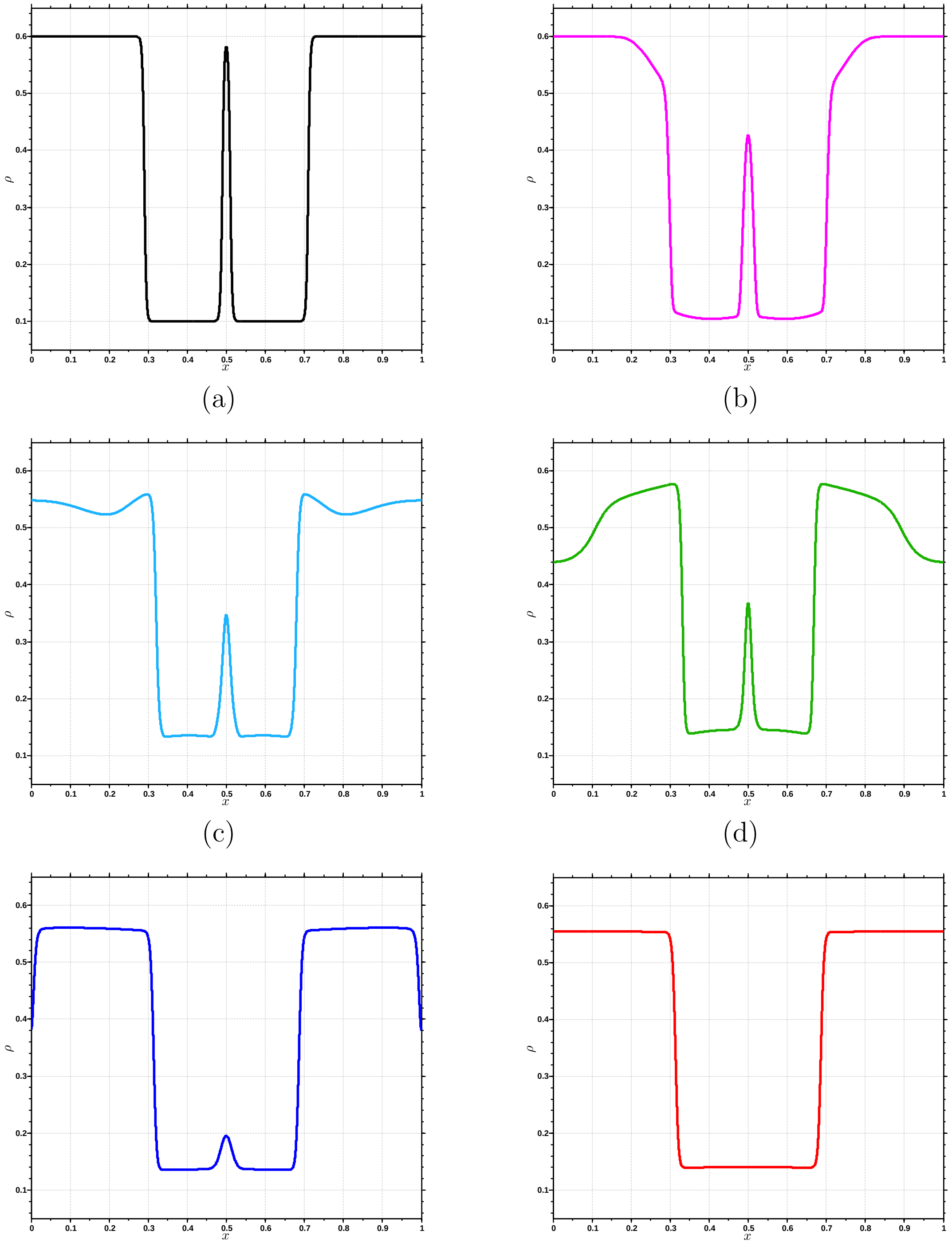

(a) (b)

(c) (d)

(e) (f)

Figure 7: Coalescence of two bubbles for the one-dimensional thermal Navier-Stokes-Korteweg equations: density profiles at (a) $t = 0.0$, (b) $t = 0.1$, (c) $t = 0.5$, (d) $t = 1.0$, (e) $t = 2.0$, and (f) $t = 10.0$.

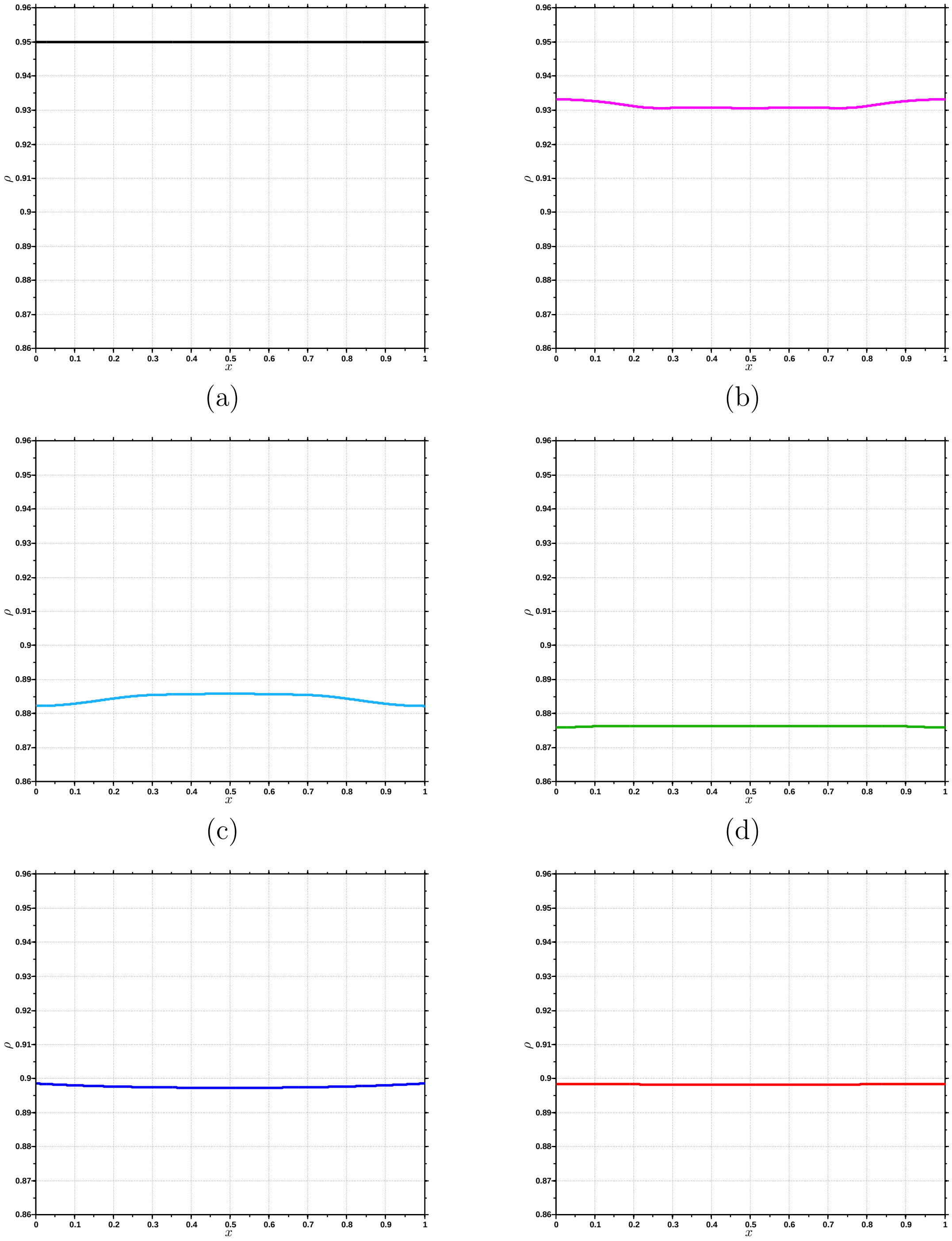

(a) (b) (c) (d) (e) (f)

Figure 8: Coalescence of two bubbles for the one-dimensional thermal Navier-Stokes-Korteweg equations: temperature profiles at (a) $t = 0.0$, (b) $t = 0.1$, (c) $t = 0.5$, (d) $t = 1.0$, (e) $t = 2.0$, and (f) $t = 10.0$.

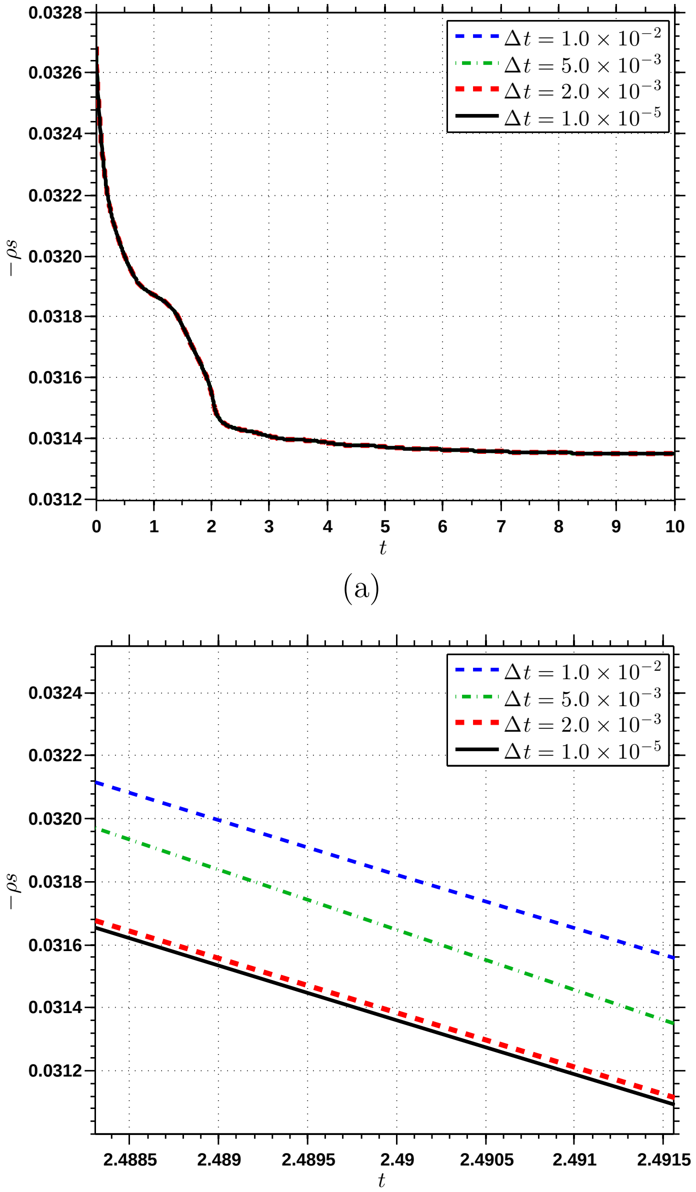

(a)

(b)

Figure 9: Coalescence of two bubbles for the one-dimensional thermal Navier-Stokes-Korteweg equations: Evolution of the discrete entropy. (a) Global view; (b) Detailed view in the vicinity of $t = 2.49$.

respectively; the initial vapor and liquid densities are $\rho_{v,0} = 0.1$ and $\rho_{l,0} = 0.6$. Hence, the vapor phase will become denser and the liquid phase will become lighter to minimize the free energy. In the meantime, the phase transition is accompanied with latent heat release and absorption, which will change the local temperature distribution. Consequently, the shape of the free energy and the Maxwell states are changed. This coupled process will eventually reach an equilibrium state. This dynamic process is illustrated in a density-temperature phase diagram in Figure 6. In Figures 7 and 8, snapshots of the density and the temperature are depicted at times $t = 0.0$, 0.1, 0.5, 1.0, 2.0 and 10.0. It is observed that the initial interface between the two vapor bubbles gradually vanishes, and the vapor and liquid densities are adjusted to achieve the energy-stable states. The temperature of the system fluctuates in time. The temperature first drops to about 0.876 at time $t = 1.0$, then it raises to 0.898 uniformly at time $t = 10.0$. The Maxwell states at $\theta = 0.898$ are $\rho_v = 0.1403$ and $\rho_l = 0.5546$. Figure 7 (f) shows that the density at $t = 10.0$ is very close to the Maxwell states. Since we applied periodic boundary conditions, the dissipation relation is

$$
\begin{aligned}
&\int_\Omega \frac{H(\rho^h_{n+1}, \theta^h_{n+1}) - H(\rho^h_n, \theta^h_n)}{\Delta t_n} d\mathbf{x} \\
=& -\int_\Omega \frac{1}{\theta^h_{n+\frac{1}{2}}} \boldsymbol{\tau}^h_{n+\frac{1}{2}} : \nabla \mathbf{u}^h_{n+\frac{1}{2}} d\mathbf{x} - \int_\Omega \frac{\kappa |\nabla \theta^h_{n+\frac{1}{2}}|^2}{\left(\theta^h_{n+\frac{1}{2}}\right)^2} d\mathbf{x} \\
&- \int_\Omega \frac{1}{\theta^h_{n+\frac{1}{2}} \Delta t_n} \frac{\llbracket \rho^h_n \rrbracket^4}{24} \frac{\partial^3 \nu_{loc}}{\partial \rho^3} (\rho^h_{n+\xi_1}, \theta^h_{n+\frac{1}{2}}) d\mathbf{x} + \int_\Omega \frac{1}{\theta^h_{n+\frac{1}{2}} \Delta t_n} \frac{\llbracket \theta^h_n \rrbracket^4}{24} \frac{\partial^3 H}{\partial \theta^3} (\rho^h_{n+\frac{1}{2}}, \theta^h_{n+\xi_2}) d\mathbf{x} \\
\leq& 0. \qquad (179)
\end{aligned}
$$

The discrete mathematical entropy is plotted against time in Figure 9 (a). It can be observed that $H(\rho^h_n, \theta^h_n)$ monotonically decreases with respect to time, which confirms the theoretical estimate given in Theorem 6. In Figure 9 (b), a detailed view of the discrete mathematical entropy in the vicinity of $t = 2.49$ is provided. It can be observed that the differences between the numerical solutions and the overkill solution decrease with reductions of time step sizes. To verify the time accuracy estimate, overkill solutions were first computed with $\Delta t = 1.0 \times 10^{-5}$. Then the computations were repeated with larger time steps $\Delta t = 5.0 \times 10^{-2}$, 1.0×10^{-2}, 5.0×10^{-3}, 1.0×10^{-3} and 5.0×10^{-4}. The errors at time $t = 1.0$ are listed in Table 2. It can be seen that the numerical solutions converge optimally in time to the overkill solutions. This again corroborates the theoretical estimates given in Theorem 7.

Table 2: Coalescence of two bubbles for the one-dimensional thermal Navier-Stokes-Korteweg equations: Temporal errors in L^2-norm at time $t = 1.0$.

Δt	5.0×10^{-2}	1.0×10^{-2}	5.0×10^{-3}	1.0×10^{-3}	5.0×10^{-4}
$\|Y_1 - Y_1^h\|_{L^2(\Omega)}$	8.40×10^{-5}	4.02×10^{-6}	1.02×10^{-6}	4.14×10^{-8}	1.04×10^{-8}
order	-	1.94	1.98	1.99	1.99
$\|Y_2 - Y_2^h\|_{L^2(\Omega)}$	2.69×10^{-4}	6.57×10^{-6}	1.64×10^{-6}	6.54×10^{-8}	1.64×10^{-8}
order	-	2.02	2.00	2.00	2.00
$\|Y_3 - Y_3^h\|_{L^2(\Omega)}$	2.70×10^{-5}	1.50×10^{-6}	3.83×10^{-7}	1.56×10^{-8}	3.93×10^{-9}
order	-	1.92	1.97	1.99	1.99

5 Applications

In this section, we investigate the van der Waals fluid model by performing simulations with the numerical algorithm developed in Section 3.

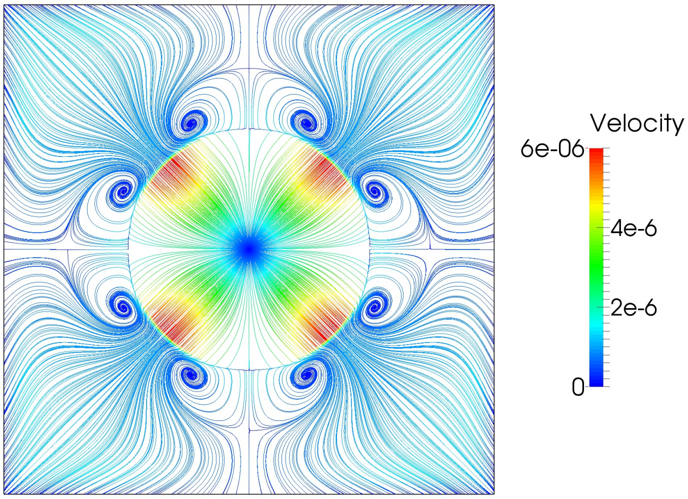

Figure 10: Velocity streamlines near a single bubble at time $t = 15.0$: $\theta_{bc} = 0.85$.

5.1 Evaporation and condensation

In this example, we numerically investigate the dynamics of a single vapor bubble in the presence of temperature increase or decrease on the boundary. In this study, the computational domain is restricted to a unit square $\Omega = (0, 1)^2$. The center of the vapor bubble is located at the center of the domain, i.e., $C_1 = (0.5, 0.5)$; the radius of the bubble is $R_1 = 0.25$. A hyperbolic tangent function is utilized to give the initial density profile:

$$\rho_0(\mathbf{x}) = 0.3545 + 0.2479 \tanh\left(\frac{d_1(\mathbf{x}) - R_1}{2} \sqrt{\mathrm{We}} \right), \tag{180}$$

$$d_1(\mathbf{x}) = |\mathbf{x} - C_1|. \tag{181}$$

The initial velocity is set to be zero. The initial temperature is given by

$$\begin{aligned} \theta_0(\mathbf{x}) &= 0.85, \quad \text{if } \mathbf{x} \in \Omega, \\ \theta_0(\mathbf{x}) &= \theta_{bc}, \quad \text{if } \mathbf{x} \in \partial\Omega. \end{aligned}$$

The boundary conditions for this problem are

$$\begin{aligned} \nabla \rho \cdot \mathbf{n} &= 0, \quad \text{on } \partial\Omega \times (0, T), \\ \mathbf{u} &= \mathbf{0}, \quad \text{on } \partial\Omega \times (0, T), \\ \theta &= \theta_{bc}, \quad \text{on } \partial\Omega \times (0, T). \end{aligned}$$

It is known that the hyperbolic tangent function is only an approximation of the steady state solution. In the function (180), the liquid density is 0.6024 and the vapor density is 0.1066, which are very close to the Maxwell states at temperature $\theta = 0.85$. Hence, there will be a low-intensity velocity field generated near the interfacial region to adjust the interface profile. The phenomenon occurring near the interface is commonly referred to as the parasitic currents [36], and a snapshot of the parasitic currents at time $t = 15.0$ is depicted in Figure 10. If $\theta_{bc} \neq 0.85$, as time evolves, thermal diffusion will drive the temperature inside Ω to θ_{bc}. This change of temperature directly leads to the change of the Maxwell states, which is observed as condensation or evaporation of the bubble. If $\theta_{bc} > 0.85$, the liquid-vapor density ratio will become smaller; if $\theta_{bc} < 0.85$, the liquid-vapor density ratio will become larger.

In Table 3, the Maxwell states at different temperatures are listed. With these values, the radius of the vapor bubble at the new stable configuration can be estimated by using the mass conservation relation. Assuming the interfacial region has measure zero, then the total mass in Ω is

$$0.1066 \times 0.25^2 \pi + 0.6024 \times (1.0 - 0.25^2 \pi) = 0.6024 - 0.031\pi. \tag{182}$$

If the Maxwell-state liquid and vapor densities at the temperature θ are denoted as ρ_l^θ and ρ_v^θ, the new radius of the vapor bubble R_{st} can be determined by the mass conservation relation

$$\rho_v^\theta \times R_{st}^2 \pi + \rho_l^\theta \times (1.0 - R_{st}^2 \pi) = 0.6024 - 0.031\pi, \tag{183}$$

if ρ_l^θ and ρ_v^θ satisfy $\rho_v^\theta \leq 0.6024 - 0.031\pi \leq \rho_l^\theta$. If $\rho_l^\theta < 0.6024 - 0.031\pi$, the steady state will be a uniform liquid state with density $0.6024 - 0.031\pi$; if $0.6024 - 0.031\pi \leq \rho_v^\theta$, the steady state will be a uniform vapor state with density $0.6024 - 0.031\pi$. The solutions of R_{st} for $\theta = 0.95$, 0.90, 0.85, 0.80, and 0.75 are listed in Table 3.

θ	0.95	0.90	0.85	0.80	0.75
ρ_v	0.1930	0.1419	0.1066	0.0799	0.0591
ρ_l	0.4872	0.5524	0.6024	0.6442	0.6808
R_{st}	-	0.1916	0.2500	0.2802	0.3000

Table 3: The liquid and vapor densities at the Maxwell states of the van der Waals fluid model at different temperatures. The values are rounded to four decimal places. R_{st} represents the steady-state vapor bubble radius with the given initial density profile (180)-(181) in the sharp interface limit. When $\theta = 0.95$, a uniform liquid state with density $\rho = 0.5050$ will form at the steady state.

In the numerical simulations, the dimensionless numbers are taken as $\mathrm{Re} = 1.451 \times 10^3$, $\mathrm{We} = 5.263 \times 10^5$, and $\gamma = 1.333$; the dimensionless thermal conductivity is $\kappa = 1.378 \times 10^{-3}$. The external body force $\mathbf{b}$ and the heat source r are fixed to be zero. The spatial mesh is comprised of 512^2 quadratic NURBS elements. The simulation is integrated up to $T = 2.0 \times 10^2$ with time step size $\Delta t = 1.0 \times 10^{-3}$. In Figure 11, the density profiles at time $t = 200.0$ are depicted for $\theta_{bc} = 0.75$, 0.80, 0.85, 0.90, and 0.95. The solution for $\theta_{bc} = 0.95$ at $t = 200.0$ forms a uniform liquid state. In Figure 12, the density fields are sampled over a straight line $y = 0.5$ and plotted as a single variable function of x. Given the density data over the straight line, we may introduce two points $0 \leq \hat{x}_1 \leq \hat{x}_2 \leq 1$, such that $\rho(\hat{x}_1) = \rho(\hat{x}_2) = (\rho_v + \rho_l)/2$. In other words, $\hat{x}_1$ and $\hat{x}_2$ are located at the centers of the diffuse interfaces over the line $y = 0.5$. Then the bubble radius of the numerical solution can be defined as $\hat{R}_{st} := |\hat{x}_1 - \hat{x}_2|/2$. In Table 4, the values of R_{st} and $\hat{R}_{st}$ are listed. It can be observed that the numerical results and the theoretical estimates of the radii matched well. From $\theta_{bc} = 0.90$ to $\theta_{bc} = 0.75$, the radius of the bubble increases with the decrease of the boundary temperature.

To quantify the width of the diffuse interface at a specific temperature, we introduce two more points $0 \leq \tilde{x}_1 \leq \tilde{x}_2 \leq 0.5$, such that $\rho(\tilde{x}_1) = \rho_l - 5\%(\rho_l - \rho_v)$ and $\rho(\tilde{x}_2) = \rho_v + 5\%(\rho_l - \rho_v)$.

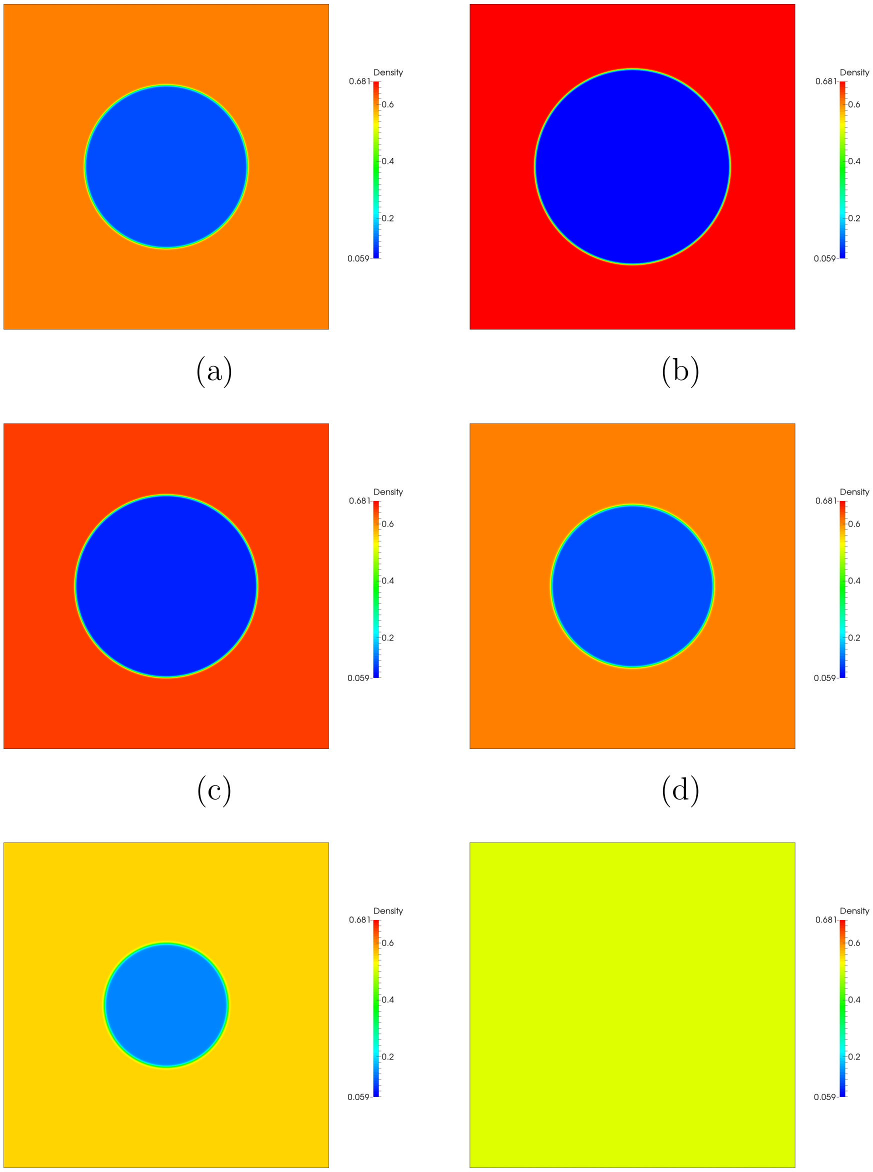

(a) (b)

(c) (d)

(e) (f)

Figure 11: Density profiles of a single bubble under different temperature boundary conditions: (a) Initial condition, (b) $\theta_{bc} = 0.75$, (c) $\theta_{bc} = 0.80$, (d) $\theta_{bc} = 0.85$, (e) $\theta_{bc} = 0.90$, (f) $\theta_{bc} = 0.95$.

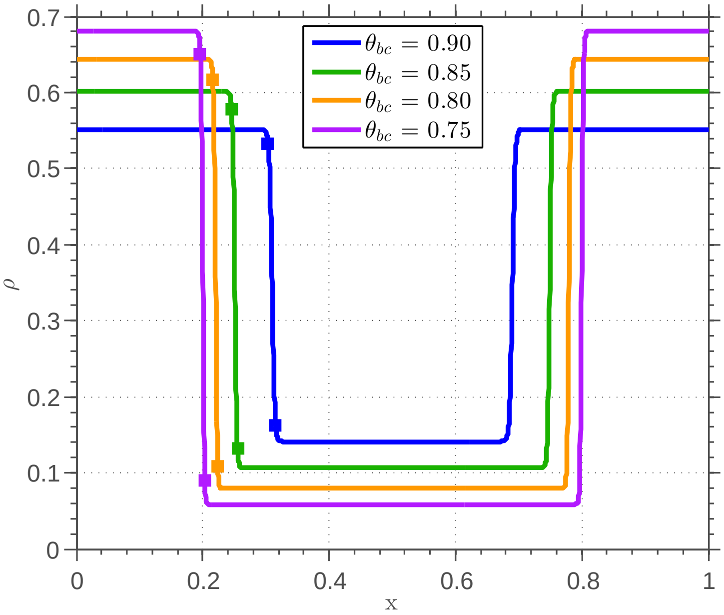

Figure 12: Plots of the density fields sampled over the straight line $y = 0.5$ for different temperature boundary conditions. The colored squares delimits the region $(\tilde{x}_1, \tilde{x}_2)$.

θ	0.90	0.85	0.80	0.75
R_{st}	0.1916	0.2500	0.2802	0.3000
$\hat{R}_{st}$	0.1902	0.2492	0.2798	0.2998

Table 4: The theoretical estimates of the bubble radius R_{st} and the numerical results of the bubble radius $\hat{R}_{st}$.

θ_{bc}	0.90	0.85	0.80	0.75
$\tilde{W}$	0.0123	0.0100	0.0083	0.0070

Table 5: The interface width $\tilde{W}$ of the numerical solutions at different temperatures. The values are rounded to four decimal places.

Within the region $(\tilde{x}_1, \tilde{x}_2)$, the density field varies 90% of the total variation between the liquid state and the vapor state. With those two points given, we may define the interface width as $\tilde{W} := \tilde{x}_2 - \tilde{x}_1$. The widths $\tilde{W}$ are listed in Table 5. The interface width increases with the increase of the temperature. So far, there has been few results on the estimate of the interface width for the van der Waals fluid. Invoking the least square method, we can obtain polynomial functions that best fit the given data, which may serve as empirical formulas for the diffuse-interface width estimate. The linear polynomial that best fits the data in the least square sense is $\tilde{W} = 0.0354\theta_{bc} - 0.0198$. The corresponding quadratic polynomial is $\tilde{W} = 0.1010\theta_{bc}^2 - 0.1313\theta_{bc} + 0.0487$. Both polynomials are plotted in Figure 13.

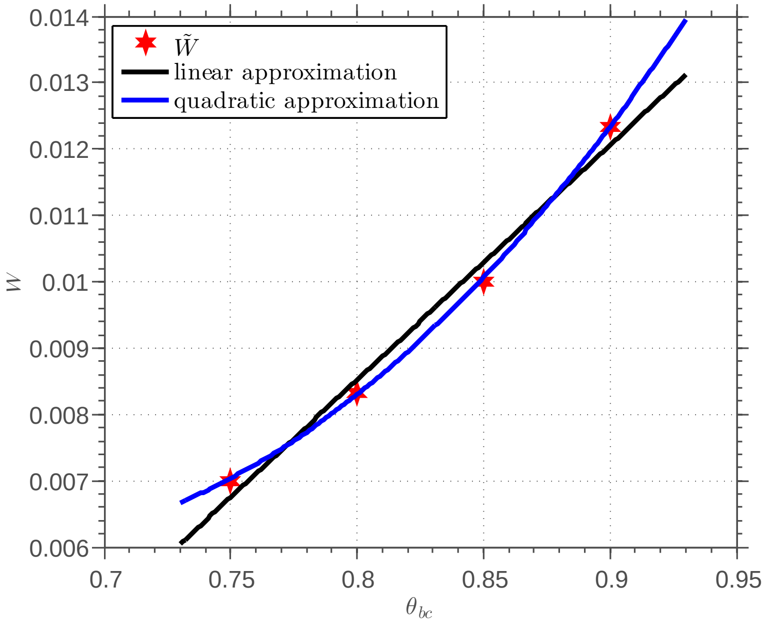

Figure 13: The values of the interface width $\tilde{W}$ at different temperatures are plotted as red hexagrams. These values are fitted by linear and quadratic polynomials. The linear polynomial is plotted as a black solid line; the quadratic polynomial is plotted as a blue solid line.

5.2 Interface motion induced by a temperature gradient

It has long been observed that an externally imposed temperature gradient may induce the motion of fluid interfaces. For multicomponent flows, this phenomenon is ascribed to the imbalance of surface tension, which is in turn caused by differences in temperature [61]. This effect is referred to as the thermocapillarity and is critical in understanding many complicated physical phenomena, such as boiling [48] and welding [49]. In the seminal paper of Young et al. [73], the surface tension is modeled as a function of the temperature. This theory was coupled with multiphase flow solvers to simulate the thermocapillary motion [1, 30, 37, 68]. However, the interface motion for a single-component fluid under a temperature gradient has rarely been studied. Recently, a mathematical model for the interface motion was constructed based on the van der Waals theory [51, 53]. In these works, the Korteweg stress includes an extra term involving temperature gradient and the interstitial working flux $\mathbf{\Pi}$ was ignored. Hence the models they considered are totally different from the model we derived. In this section, we investigate the interface motion of a single vapor bubble under a temperature gradient in two- and three-dimensions with zero gravity. It is worth emphasizing that, in our simulations, the capillarity coefficient λ remains a constant independent of the temperature.

5.2.1 Two-dimensional bubble motion in a temperature gradient

In this example, the computational domain is a two-dimensional square $\Omega = (0,1)^2$. The boundary of Ω is partitioned into three non-overlapping subdivisions:

$$\begin{aligned}
&\partial\Omega = \Gamma_v \cup \Gamma_t \cup \Gamma_b,\\
&\Gamma_v := \partial\Omega \cap \left\{ \left\{ \mathbf{x} \in \mathbb{R}^2 | x = 0 \right\} \cup \left\{ \mathbf{x} \in \mathbb{R}^2 | x = 1 \right\} \right\},\\
&\Gamma_b := \partial\Omega \cap \left\{ \mathbf{x} \in \mathbb{R}^2 | y = 0 \right\},\\
&\Gamma_t := \partial\Omega \cap \left\{ \mathbf{x} \in \mathbb{R}^2 | y = 1 \right\}.
\end{aligned}$$

The initial density is given by

$$\begin{aligned}
&\rho_0(\mathbf{x}) = 0.35 + 0.25 \tanh\left(\frac{d_1(\mathbf{x}) - 0.2}{2} \sqrt{\mathrm{We}} \right),\\
&d_1(\mathbf{x}) = |\mathbf{x} - C_1|,
\end{aligned}$$

wherein the center of the static vapor bubble is $C_1 = (0.5, 0.5)$. The initial velocity is fixed to be zero and the initial temperature is

$$\begin{aligned}
&\theta_0(\mathbf{x}) = 0.85 \quad \mathbf{x} \in \Omega \cup \Gamma_v \cup \Gamma_b,\\
&\theta_0(\mathbf{x}) = 0.87 \quad \mathbf{x} \in \Gamma_t.
\end{aligned}$$

The boundary conditions for this problem are

$$\nabla\rho \cdot \mathbf{n} = 0, \qquad \text{on } \partial\Omega \times (0,T),$$

$$
\begin{aligned}
\mathbf{u} &= \mathbf{0}, && \text{on } \partial\Omega \times (0,T), \\
\theta &= 0.85, && \text{on } \Gamma_b \times (0,T), \\
\theta &= 0.87, && \text{on } \Gamma_t \times (0,T), \\
-\mathbf{q}\cdot\mathbf{n} &= 0, && \text{on } \Gamma_v \times (0,T).
\end{aligned}
$$

The dimensionless numbers and the dimensionless thermal conductivity are chosen as

$$
\begin{aligned}
\mathrm{Re} &= 1.738 \times 10^4, \\
\mathrm{We} &= 3.277 \times 10^6, \\
\gamma &= 1.333, \\
\kappa &= 3.453 \times 10^{-3}.
\end{aligned}
$$

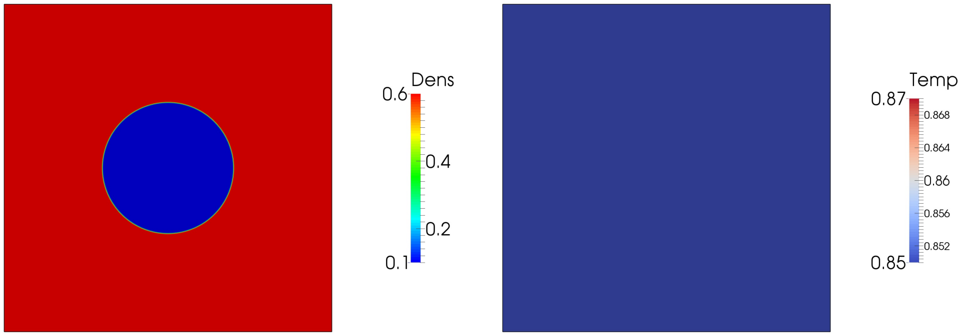

(a) (b)

Figure 14: The motion of a single bubble in a two-dimensional square: Initial conditions for density (a) and temperature (b).

The spatial discretization is comprised of 1024^2 quadratic NURBS. The time integration is performed with a fixed step size $\Delta t = 5.0 \times 10^{-4}$ up to the final time $T = 500.0$. In Figure 14, the initial density and temperature profiles are illustrated. In Figures 15-16, the density, temperature, and velocity fields are depicted at various time steps. It is noted that there is a velocity field generated immediately after the simulation starts. The velocity drives the vapor bubble toward the positive thermal gradient direction. Eventually, the vapor bubble attaches to the heated wall boundary and forms a hemispheric shape, as is shown in Figure 16 (b). It can be observed that, in the liquid phase, there is a temperature gradient generated between the heated top boundary and the cooled bottom boundary. Inside the vapor bubble, the temperature distribution remains homogeneous throughout the whole

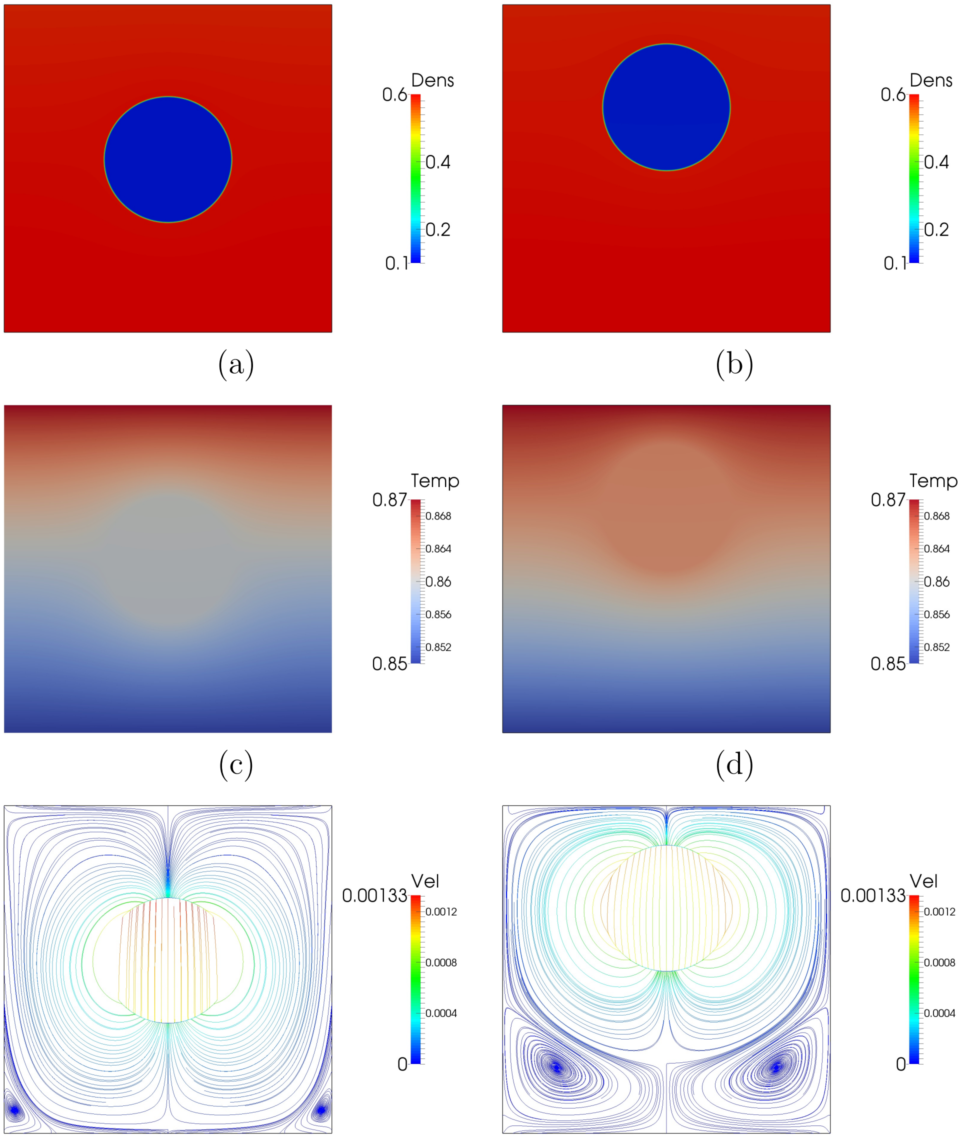

(a) (b) (c) (d) (e) (f)

Figure 15: The motion of a single bubble in a two-dimensional square: Solutions at $t = 50.0$ (left column) and $t = 200.0$ (right column). The first row depicts the density profiles; the second row depicts the temperature profiles; the third row visualizes the velocity streamlines.

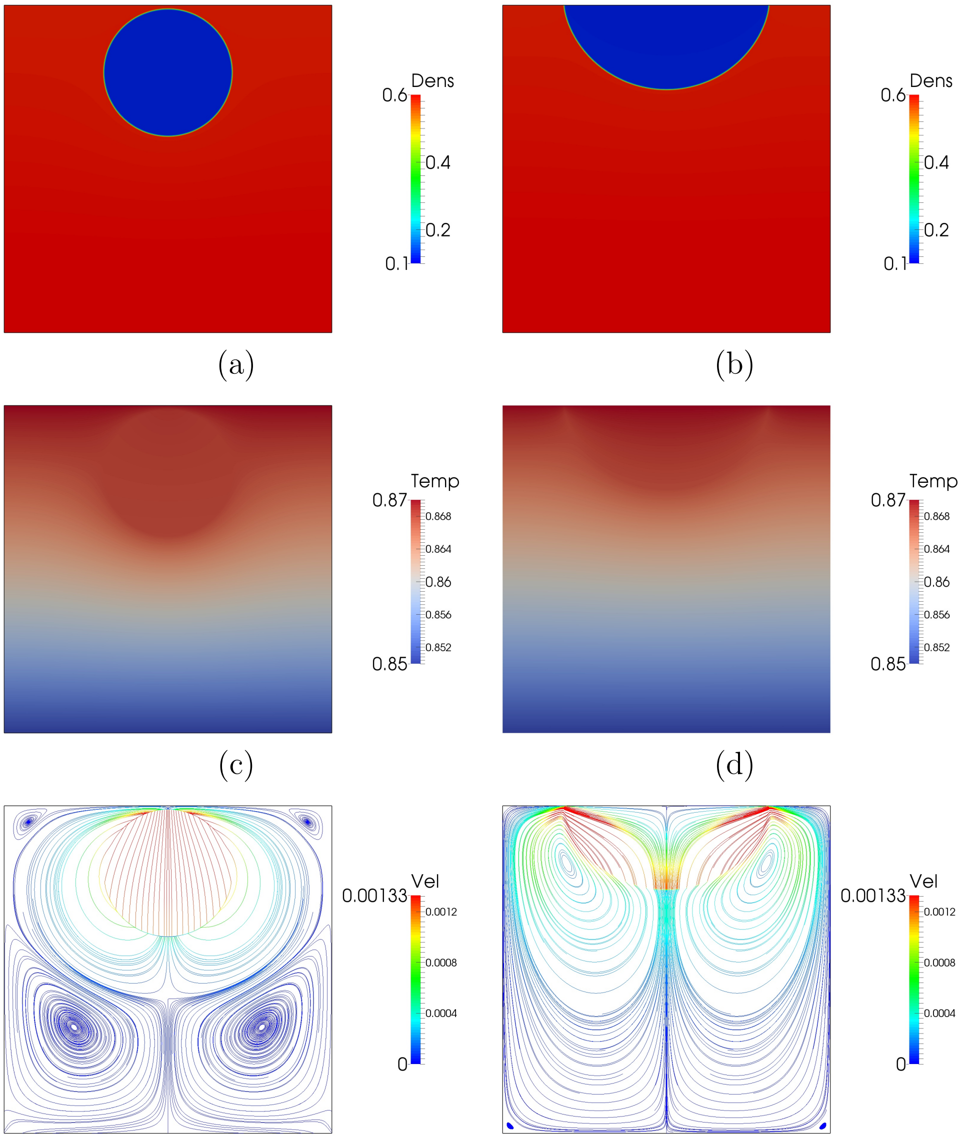

(a) (b) (c) (d) (e) (f)

Figure 16: The motion of a single bubble in a two-dimensional square: Solutions at $t = 300.0$ (left column) and $t = 500.0$ (right column). The first row depicts the density profiles; the second row depicts the temperature profiles; the third row visualizes the velocity streamlines.

process. The homogeneous temperature inside the vapor bubble was analyzed in [51] and was attributed to the latent heat diffusion.

5.2.2 Three-dimensional bubble motion in a temperature gradient

As a second example, a three-dimensional numerical simulation is performed. The computation domain is $\Omega = (0, 0.5) \times (0, 0.5) \times (0, 1)$. The boundary of Ω is partitioned into three non-overlapping subdivisions:

$$\begin{aligned}
&\partial\Omega = \Gamma_t \cup \Gamma_b \cup \Gamma_v, \\
&\Gamma_b := \partial\Omega \cap \left\{\mathbf{x} \in \mathbb{R}^2 | z = 0\right\}, \\
&\Gamma_t := \partial\Omega \cap \left\{\mathbf{x} \in \mathbb{R}^2 | z = 1\right\}, \\
&\Gamma_v := \partial\Omega \cap \Big\{\left\{\mathbf{x} \in \mathbb{R}^2 | x = 0\right\} \cup \left\{\mathbf{x} \in \mathbb{R}^2 | x = 0.5\right\} \\
&\qquad\qquad \cup \left\{\mathbf{x} \in \mathbb{R}^2 | y = 0\right\} \cup \left\{\mathbf{x} \in \mathbb{R}^2 | y = 0.5\right\}\Big\}.
\end{aligned}$$

The center of the vapor bubble is initially located at $C_1 = (0.25, 0.25, 0.3)$, and the bubble radius is 0.2. The initial density and velocity are

$$\begin{aligned}
&\rho_0(\mathbf{x}) = 0.35 + 0.25 \tanh\left(\frac{d_1(\mathbf{x}) - 0.2}{2}\sqrt{\mathrm{We}}\right), \\
&d_1(\mathbf{x}) = |\mathbf{x} - C_1|, \\
&\mathbf{u}_0(\mathbf{x}) = \mathbf{0}.
\end{aligned}$$

The initial temperature is

$$\begin{aligned}
&\theta_0(\mathbf{x}) = 0.85, \quad \mathbf{x} \in \Omega \cup \Gamma_v \cup \Gamma_b, \\
&\theta_0(\mathbf{x}) = 0.87, \quad \mathbf{x} \in \Gamma_t.
\end{aligned}$$

The boundary conditions for this problem are

$$\begin{aligned}
&\nabla\rho \cdot \mathbf{n} = 0, && \text{on } \partial\Omega \times (0, T), \\
&\mathbf{u} = \mathbf{0}, && \text{on } \partial\Omega \times (0, T), \\
&\theta = 0.85, && \text{on } \Gamma_b \times (0, T), \\
&\theta = 0.87, && \text{on } \Gamma_t \times (0, T), \\
&-\mathbf{q} \cdot \mathbf{n} = 0, && \text{on } \Gamma_v \times (0, T).
\end{aligned}$$

The dimensionless numbers and the dimensionless thermal conductivity are taken as

$$\begin{aligned}\mathrm{Re} &= 3.570 \times 10^3,\\ \mathrm{We} &= 1.383 \times 10^5,\\ \gamma &= 1.333,\\ \kappa &= 1.681 \times 10^{-2}.\end{aligned}$$

The spatial mesh for this problem is comprised of $128 \times 128 \times 256$ quadratic NURBS elements. The time integration is performed up to the final time $T = 200$ with a fixed time step size of $\Delta t = 1.0 \times 10^{-3}$. Figures 17-19 present snapshots of density isosurfaces, velocity streamlines, and temperature contours at various slices. As soon as the simulation starts, there is a temperature gradient generated in the liquid phase; the temperature field inside the vapor bubble remains nearly homogeneous. Similarly to the two-dimensional case, there is a velocity field generated instantaneously after the top boundary is heated. The initial vapor bubble is then driven by the velocity toward the heated boundary. At about $t = 160$, the vapor bubble touches the top heated boundary. At $t = 200$, a vapor layer is formed, which separates the heated wall boundary from the bulk liquid phase. The velocity magnitude at $t = 200$ is uniformly small. The solutions shown in Figure 19 (c) and (d) can be regarded to be very close to the steady state solutions.

5.3 Boiling

Boiling is a thermally induced phase transition process in which new liquid-vapor interfaces are generated in a bulk liquid region [15, 55]. The new interfaces may form from discrete cavities on heated surfaces, which is called nucleate boiling, or from a stable superheated vapor layer, which is referred to as film boiling. Nucleate boiling is characterized by isolated bubble generation and is the most efficient mode in heat transfer. If the surface temperature increases, bubbles on the surface tend to move horizontally and merge together to form a vapor layer. Beyond a certain critical surface temperature, a stable vapor film may eventually form between the heated solid surface and the bulk liquid phase, and vapor bubbles detach from the layer periodically. Film boiling is quite dangerous and should be avoided in most industrial facilities because of the heat accumulated in the vapor film. Boiling has been extensively employed in energy conversion facilities, such as power generators, cooling systems for electronic devices, and petroleum refineries. Despite its importance in industry, the fundamental mechanism of boiling is still not well understood, as was acknowledged by physicists [2, 52] and engineers [16, 38]. To date, knowledge about boiling is mainly obtained

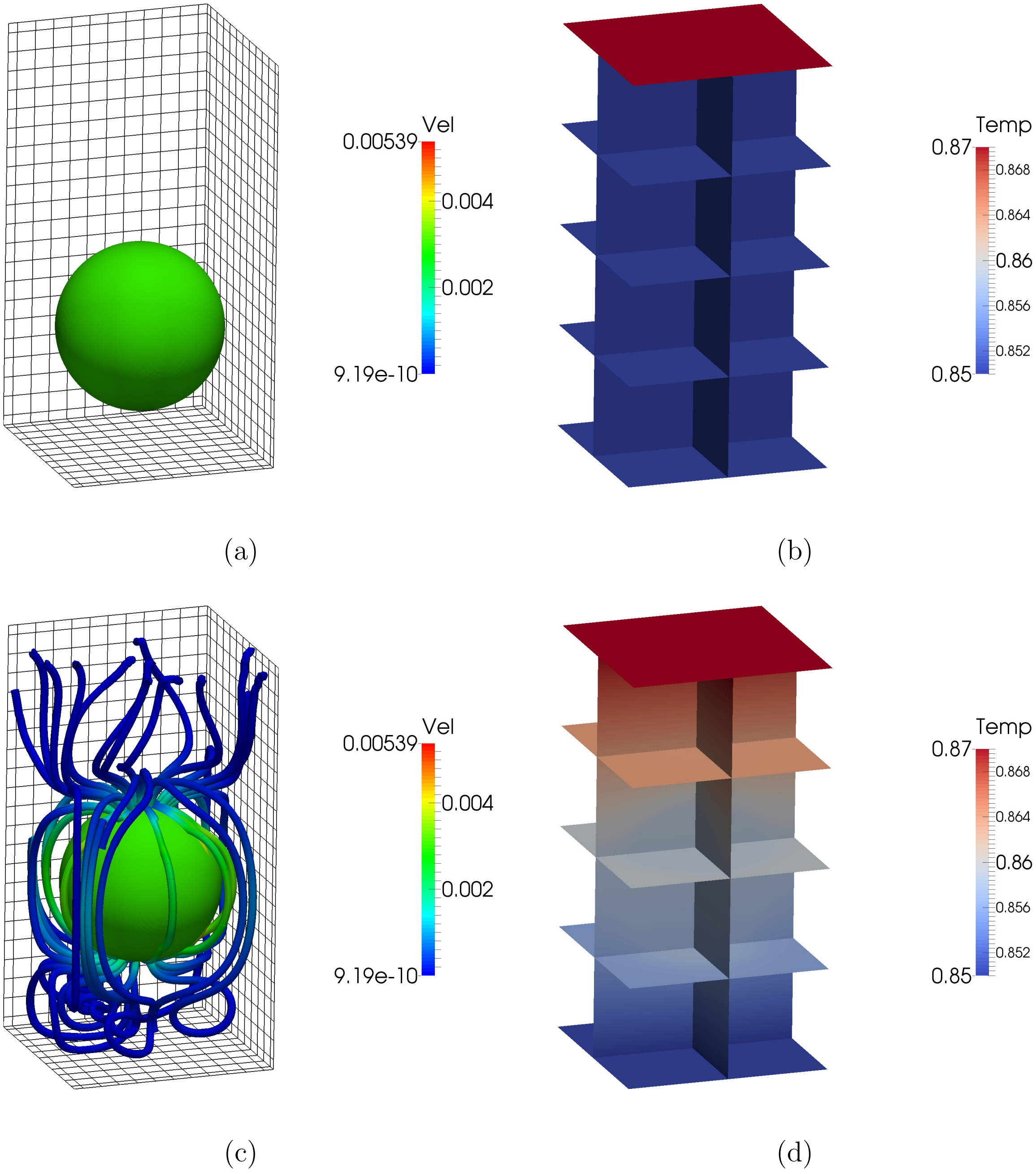

(a) (b) (c) (d)

Figure 17: Three-dimensional motion of a single bubble: (a) density isosurface at $t = 0.0$, (b) temperature on various slices at $t = 0.0$, (c) density isosurface and streamlines at $t = 40.0$, (b) temperature on various slices at $t = 40.0$.

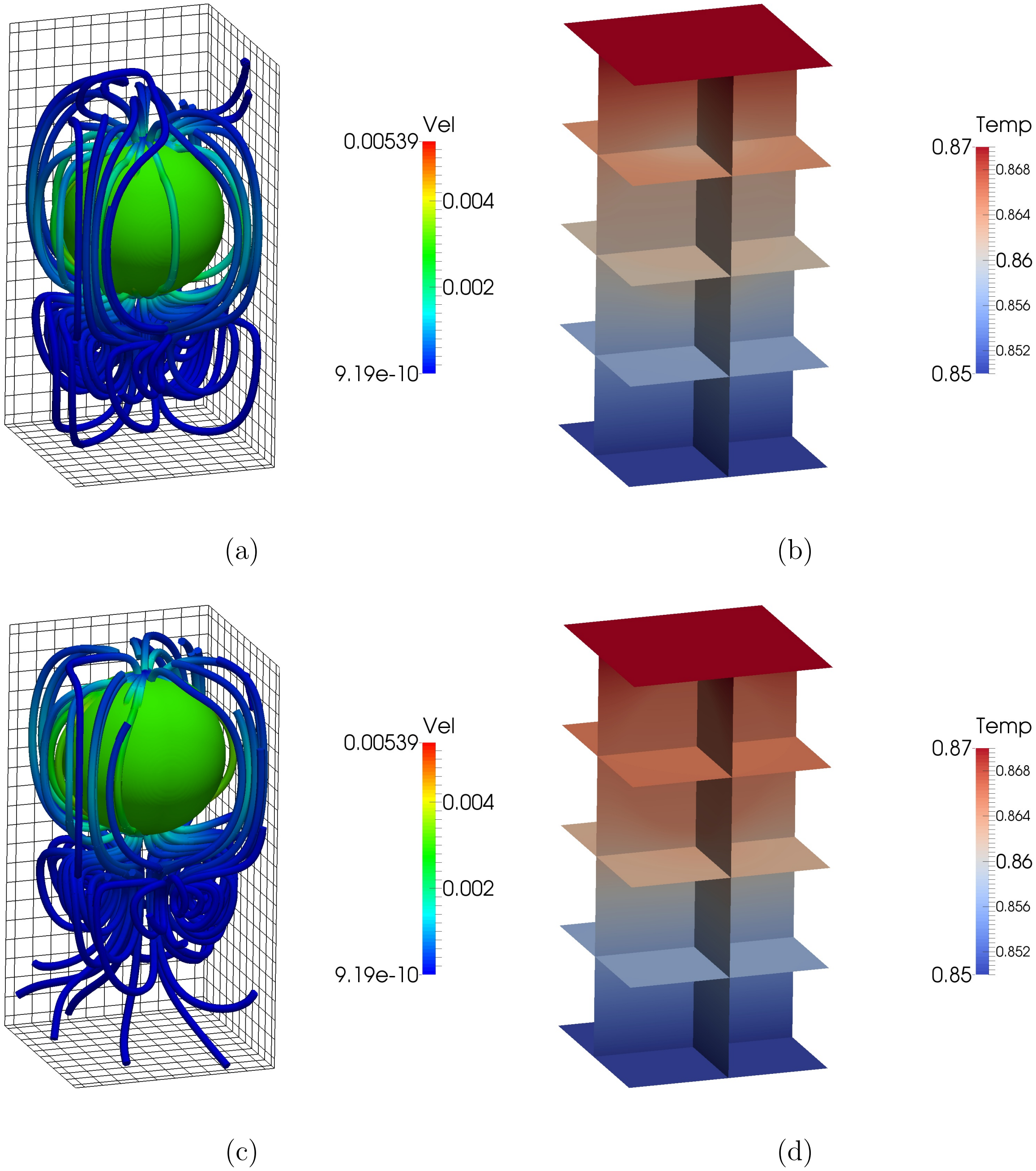

(a) (b)

(c) (d)

Figure 18: Three-dimensional motion of a single bubble: (a) density isosurface and streamlines at $t = 80.0$, (b) temperature on various slices at $t = 80.0$, (c) density isosurface and streamlines at $t = 120.0$, (b) temperature on various slices at $t = 120.0$.

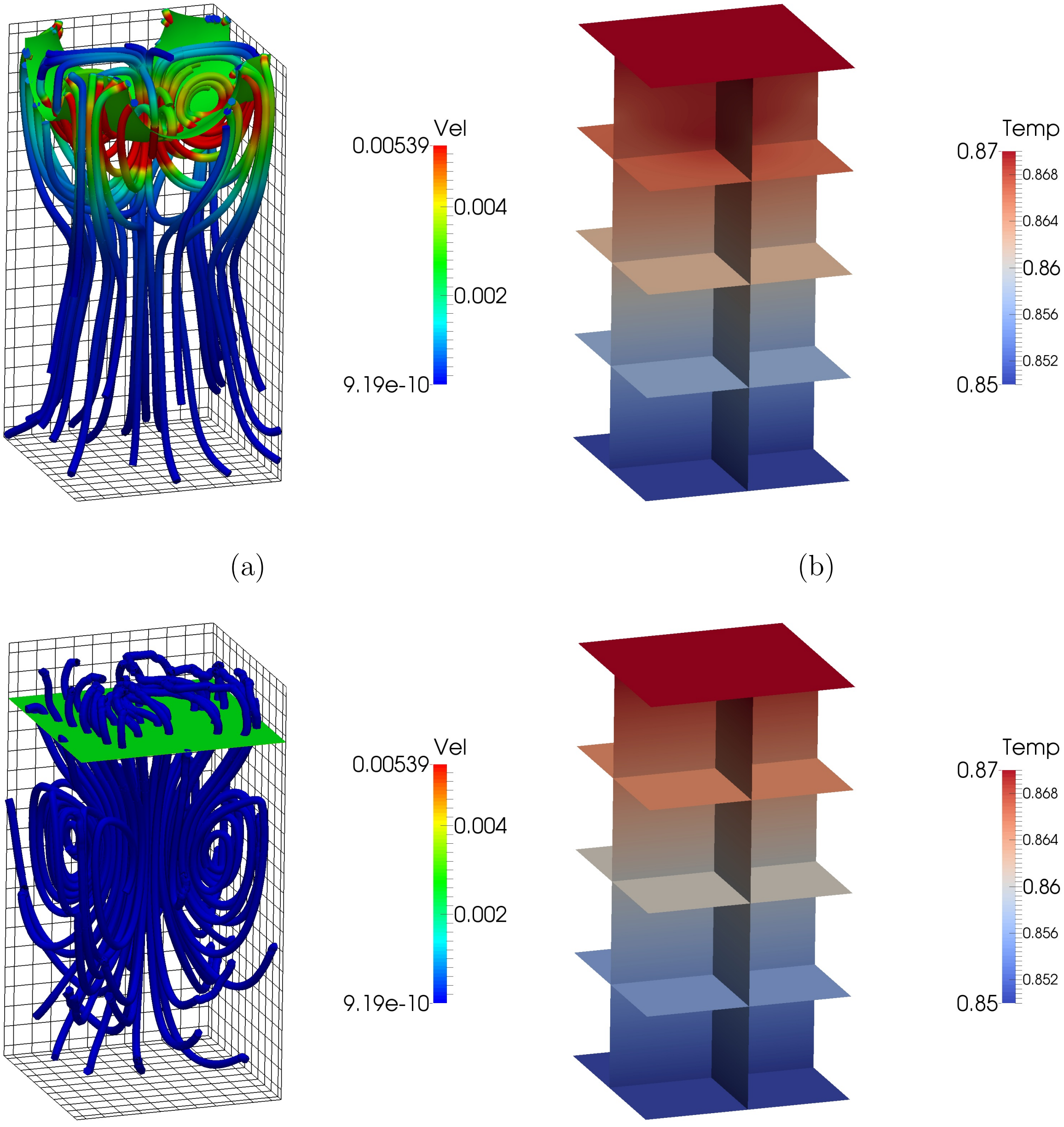

(a) (b)

(c) (d)

Figure 19: Three-dimensional motion of a single bubble: (a) density isosurface and streamlines at $t = 160.0$, (b) temperature on various slices at $t = 160.0$, (c) density and streamlines isosurface at $t = 200.0$, (b) temperature on various slices at $t = 200.0$.

by correlating experimental data to empirical formulas. In view of its disparity of spatiotemporal scales and the elusive nature of many subprocesses, a predictive model for boiling is highly important for engineering designs.

There have been a few but growing numerical studies of boiling in the past years. Film boiling is regarded as most amenable to modeling, since its governing mechanism is principally the Rayleigh-Taylor instability. A multiphase solver that can simulate the Rayleigh-Taylor instability should be capable of simulating film boiling. Existing numerical simulations have been carried out by the level set method [64], the front tracking method [38], and the volume-of-fluid method [71]. Those simulations all started with a preexisting perturbed flat interface as the initial condition. In other words, none of those methods captured the film generation process. On the other side, very few simulations of nucleate boiling have been performed because more physical mechanisms are involved in this phenomenon. A credible nucleate boiling solver is expected to be capable of describing the creation of new interfaces near the nucleation sites, handling the Rayleigh-Taylor instability and the Rayleigh-Bénard instability, and tracking the moving interfaces of bubbles and free surfaces. In [65], the authors have studied the nucleate boiling by specifically designing a model for the region near the nucleate cavities. This approach destroys the conservation structure and relies on empirical data, including the bubble release rate, the nucleation site density, etc. In this work, we simulate boiling flows in two and three dimensions, using the Navier-Stokes-Korteweg equations. To obtain successful boiling simulations, there are several additional modeling considerations. First, the transport parameters are chosen to be density dependent in order to differentiate the properties of the liquid and vapor phases. Specifically, the dimensionless viscosity $\bar{\mu}$ and the thermal conductivity κ are larger in the liquid region than in the vapor region. In our simulations, these two parameters are taken as

$$\begin{aligned} \bar{\mu} &= C_{\mu}^{boil}\rho, \\ \kappa &= C_{\kappa}^{boil}\rho, \end{aligned}$$

with C_{μ}^{boil} and C_{κ}^{boil} being constants independent of ρ. Second, the gravity effect should be taken into account to generate the buoyant effect. The dimensionless body force $\mathbf{b}$ is chosen as

$$\mathbf{b} = (0; 0; -0.025)^T ,$$

for the three-dimensional case and

$$\mathbf{b} = (0; -0.025)^T ,$$

for the two-dimensional case. Third, the ninety-degree contact angle boundary condition is used for the density variable and the slip boundary condition is applied to the velocity. To specify the boundary condition for the temperature, the boundary $\partial\Omega$ is divided into three non-overlapping parts:

$$\begin{aligned}
\partial\Omega &= \Gamma_t \cup \Gamma_b \cup \Gamma_v, \\
\Gamma_t &= \{\mathbf{x} \in \partial\Omega | \mathbf{n}(\mathbf{x}) \cdot \mathbf{b} < 0\}, \\
\Gamma_b &= \{\mathbf{x} \in \partial\Omega | \mathbf{n}(\mathbf{x}) \cdot \mathbf{b} > 0\}, \\
\Gamma_v &= \{\mathbf{x} \in \partial\Omega | \mathbf{n}(\mathbf{x}) \cdot \mathbf{b} = 0\}.
\end{aligned}$$

With the above partition, the boundary condition for θ is

$$\begin{aligned}
\theta &= \theta_h, \quad \text{on } \Gamma_b \times (0,T), \\
\theta &= \theta_c, \quad \text{on } \Gamma_t \times (0,T), \\
-\mathbf{q} \cdot \mathbf{n} &= 0, \quad \text{on } \Gamma_v \times (0,T).
\end{aligned}$$

In the numerical calculations, the Dirichlet boundary conditions for θ on Γ_b and Γ_t should be transformed to the Dirichlet boundary conditions for the entropy variable Y_5 as

$$\begin{aligned}
Y_5 = Y_{5,h} &= -\frac{1}{\theta_h}, \quad \text{on } \Gamma_b \times (0,T), \\
Y_5 = Y_{5,c} &= -\frac{1}{\theta_c}, \quad \text{on } \Gamma_t \times (0,T).
\end{aligned}$$

Throughout, the Dirichlet data are chosen as $\theta_h = 0.950$ and $\theta_c = 0.775$. In real situations, the temperature on the solid surface cannot be evenly distributed due to surface unevenness. This effect is modeled by adding perturbations to the Dirichlet data:

$$\begin{aligned}
Y_{5,h} &= -\frac{1}{0.950} + \delta_{Y_{5,h}}(\mathbf{x}), \\
Y_{5,c} &= -\frac{1}{0.775} + \delta_{Y_{5,c}}(\mathbf{x}),
\end{aligned}$$

wherein $\delta_{Y_{5,h}}(\mathbf{x})$ and $\delta_{Y_{5,c}}(\mathbf{x})$ are scalar perturbation functions that mimic the uneven temperature distribution on the solid surface. As for the initial conditions, the initial density and temperature are given by hyperbolic tangent functions; the initial velocity is zero. The detailed formulations of the initial conditions are given in subsequent sections. These conditions represent a static free surface, with liquid in the bottom region and vapor in the top region. It is worth emphasizing that the initial liquid and vapor densities are uniform with no perturbations. In contrast to existing boiling models, there is no artificial manipulation used to serve as boiling onset in this model. The following results will show that the vapor bubble or the vapor film may form automatically without preexisting nuclei simply due to local temperature variations. Another appealing property of this model is that nucleate boiling and film boiling can be simulated within a unified framework by proper selection of dimensionless parameters. These features may be credited to the thermodynamically consistent nature of the model and the algorithm. It is expected that this new methodology may lead to a predictive tool for boiling.

The rest of this section is organized as follows. In Section 5.3.1, we perform a mesh sensitivity test. In Sections 5.3.2 and 5.3.3, two-dimensional nucleate boiling and two-dimensional film boiling are numerically studied. A three-dimensional boiling simulation is investigated in Section 5.3.4.

5.3.1 Two-dimensional mesh sensitivity test

Before we start simulating practical examples, a mesh sensitivity test is performed to examine the mesh independence of the solution. The simulation domain is $\Omega = (0,1) \times (0,0.5)$. The material parameters are chosen as

$$\begin{aligned} \mathrm{We} &= 2.103 \times 10^{6}, \\ \gamma &= 1.333, \\ C_{\mu}^{boil} &= 2.298 \times 10^{-4}, \\ C_{\kappa}^{boil} &= 3.448 \times 10^{-5}. \end{aligned}$$

The initial conditions for this problem are

$$\begin{aligned} \rho_0(\mathbf{x}) &= 0.3660 - 0.2971 \tanh\left(\frac{x_2 - 0.35}{2}\sqrt{\mathrm{We}}\right), \\ \mathbf{u}_0(\mathbf{x}) &= \mathbf{0}, \\ \theta_0(\mathbf{x}) &= 0.775. \end{aligned}$$

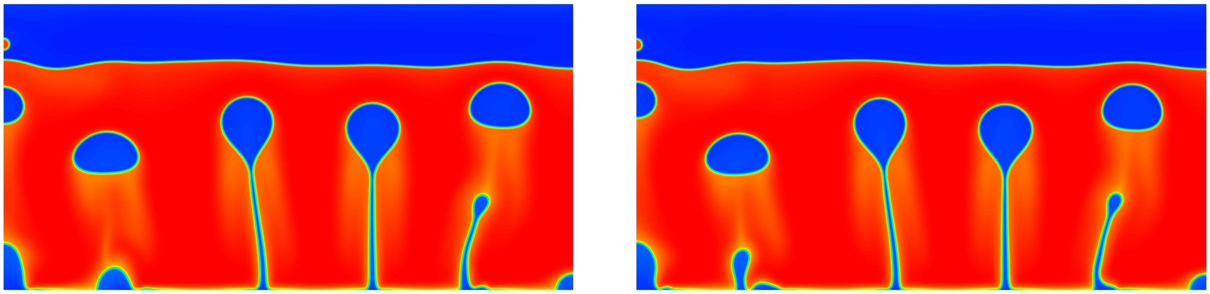

(a) 800 × 400 quadratic NURBS elements (b) 1024 × 512 quadratic NURBS elements

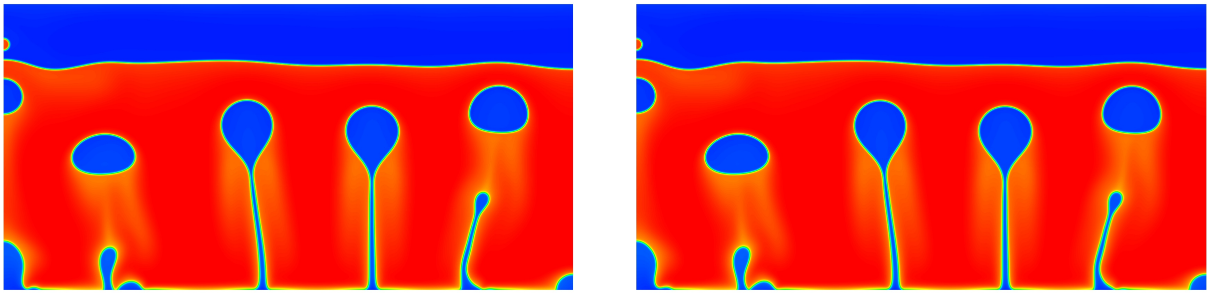

(c) 2048 × 1024 quadratic NURBS elements (d) 4096 × 2048 quadratic NURBS elements

Figure 20: Density profiles of the mesh sensitivity test at $t = 35.0$.

The perturbation for the temperature on the boundary $\delta_{Y_{5,h}}(\mathbf{x})$ and $\delta_{Y_{5,c}}(\mathbf{x})$ are

$$\delta_{Y_{5,h}}(\mathbf{x}) = 5.0 \times 10^{-2} \sin(10\pi x),$$
$$\delta_{Y_{5,c}}(\mathbf{x}) = 5.0 \times 10^{-3} \sin(10\pi x).$$

The problem is integrated up to $T = 35.0$ with time step size $\Delta t = 1.0 \times 10^{-4}$. We use four different spatial meshes: 800×400, 1024×512, 2048×1024, and 4096×2048 quadratic NURBS elements. The density profiles at $t = 35$ are depicted in Figure 20. As can be seen, the density profiles are similar for all four meshes. In the coarsest mesh, the shape of the second bubble attached to the bottom (from left to right) is significantly different from those in the finer meshes. The solutions shown in Figure 20 (c) and (d) are almost indistinguishable. Therefore, in the following two-dimensional calculations, we used 2048×1024 quadratic NURBS elements to save computation time.

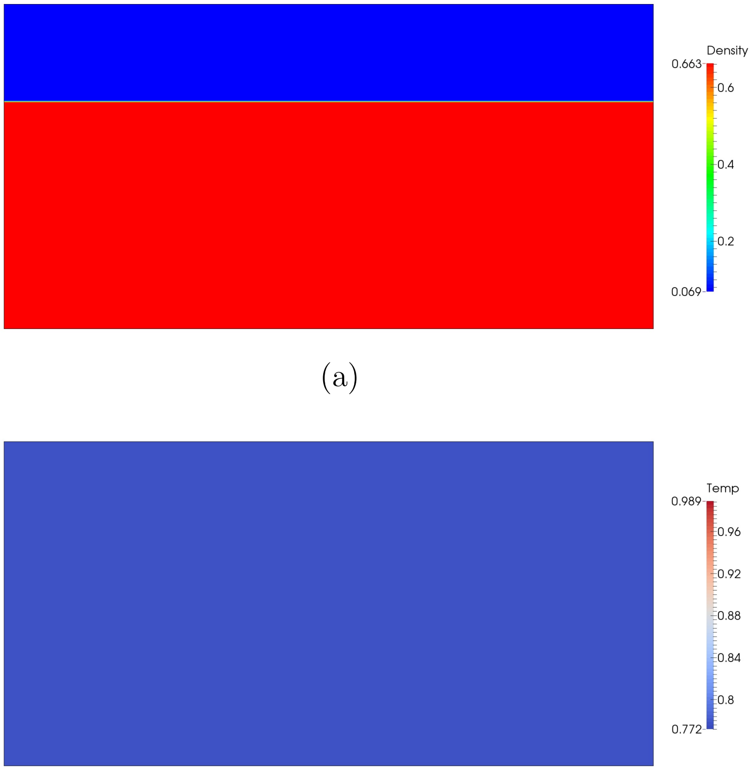

(a)

(b)

Figure 21: Initial conditions of the two-dimensional boiling simulation: (a) density, (b) temperature.

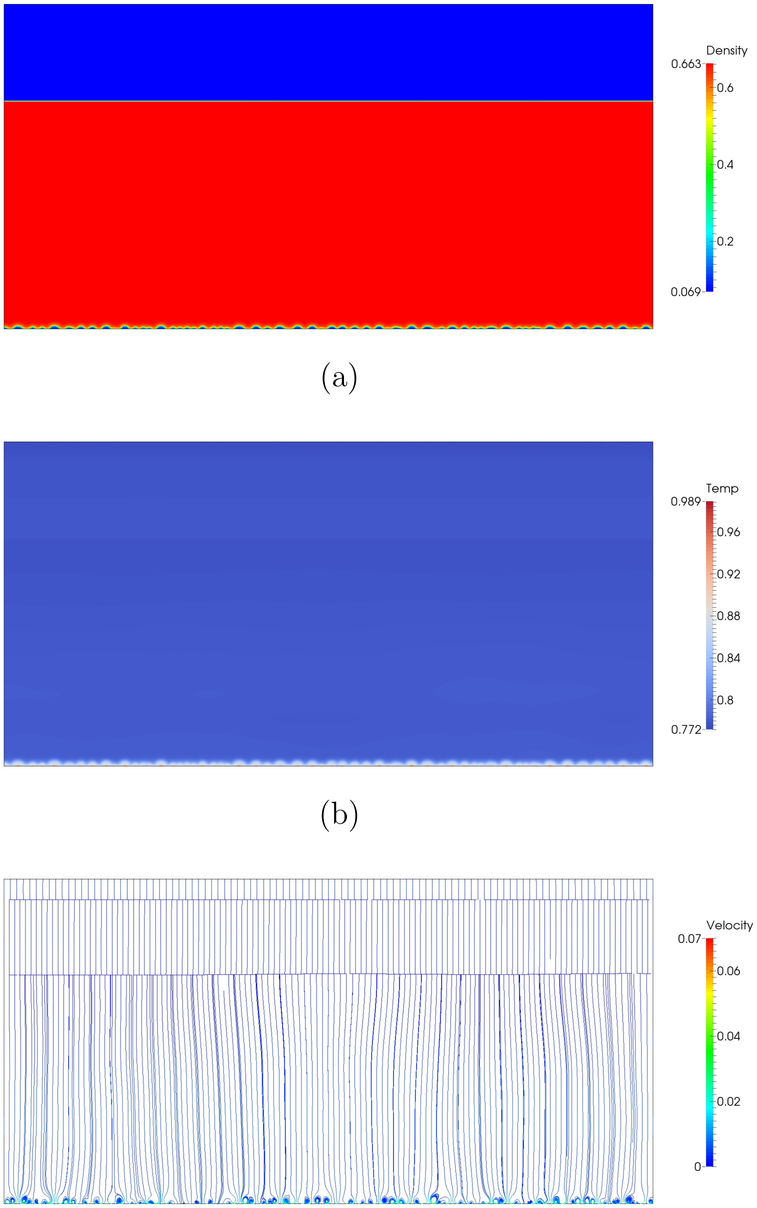

(a)

(b)

(c)

Figure 22: Solutions of the two-dimensional nucleate boiling simulation at $t = 1.25$: (a) density, (b) temperature, (c) velocity streamlines.

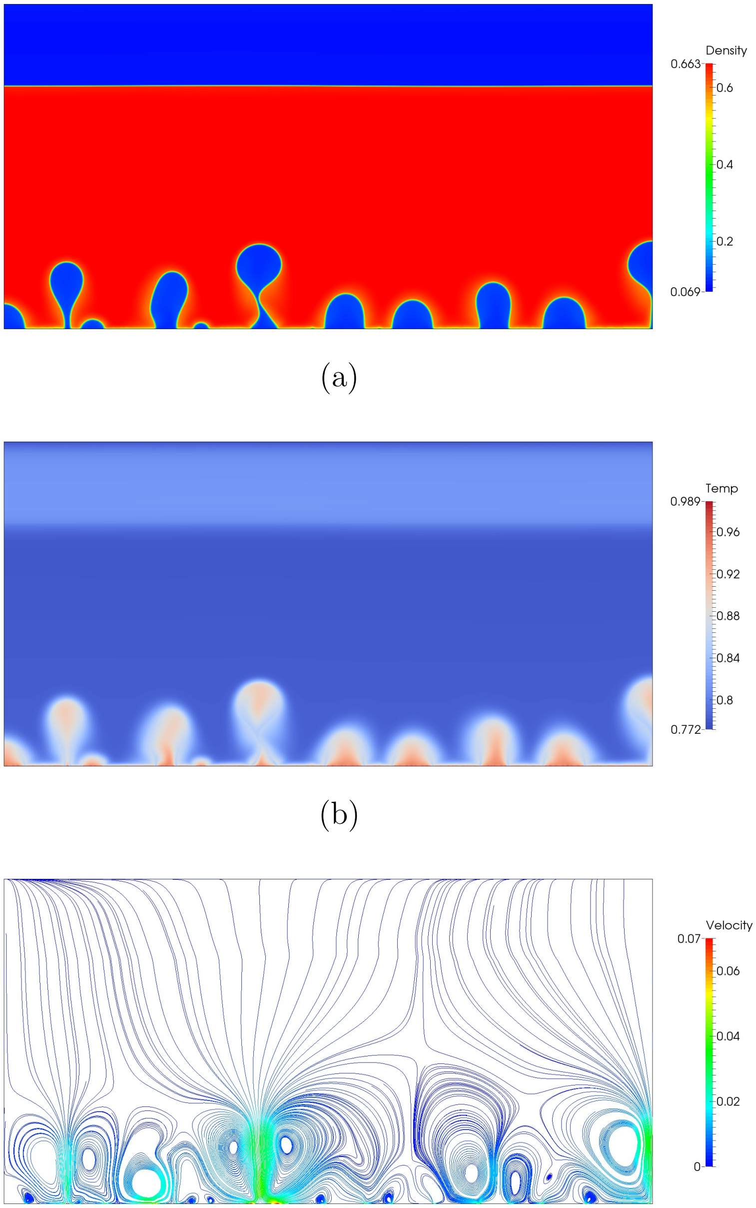

(a)

(b)

(c)

Figure 23: Solutions of the two-dimensional nucleate boiling simulation at $t = 18.75$: (a) density, (b) temperature, (c) velocity streamlines.

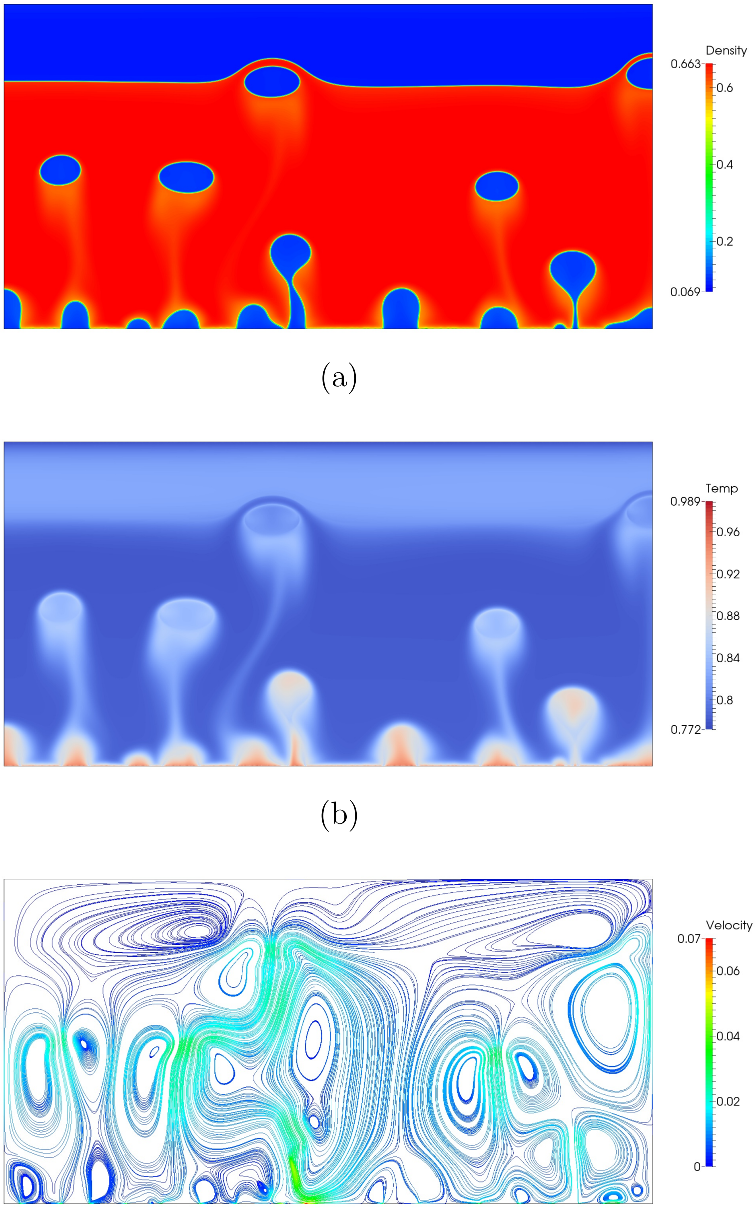

(a)

(b)

(c)

Figure 24: Solutions of the two-dimensional nucleate boiling simulation at $t = 31.25$: (a) density, (b) temperature, (c) velocity streamlines.

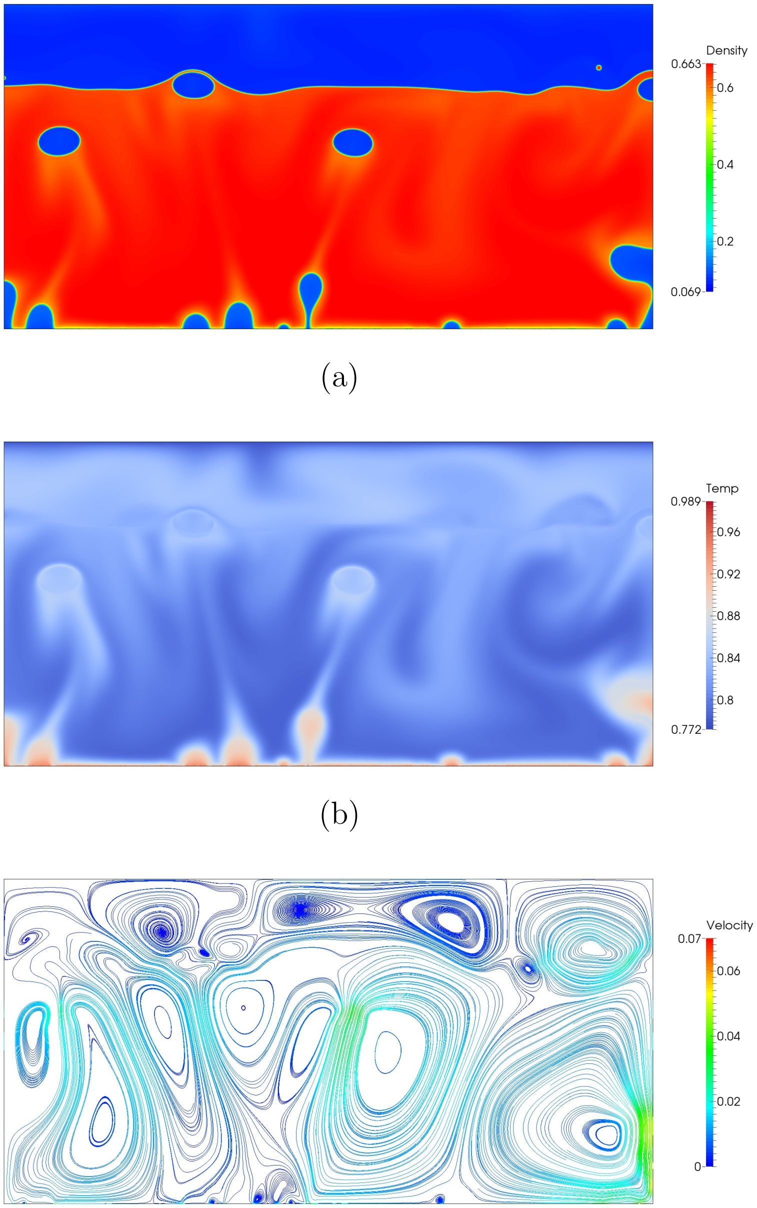

(a)

(b)

(c)

Figure 25: Solutions of the two-dimensional nucleate boiling simulation at $t = 62.5$: (a) density, (b) temperature, (c) velocity streamlines.

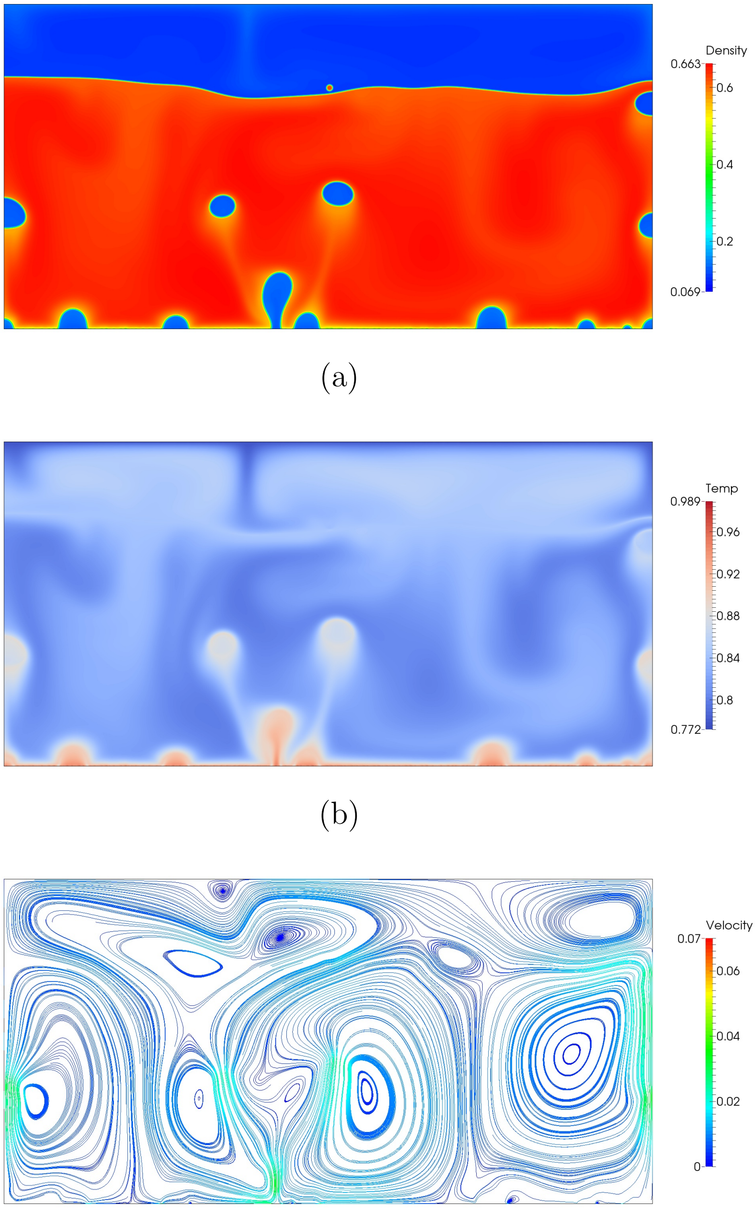

(a)

(b)

(c)

Figure 26: Solutions of the two-dimensional nucleate boiling simulation at $t = 100.0$: (a) density, (b) temperature, (c) velocity streamlines.

5.3.2 Two-dimensional nucleate boiling

In this example, we simulate boiling flows in a two-dimensional rectangular domain $\Omega = (0,1) \times (0,0.5)$. The material parameters are chosen as

$$\begin{aligned}\mathrm{We} &= 8.401 \times 10^6,\\ \gamma &= 1.333,\\ C_\mu^{boil} &= 1.150 \times 10^{-4},\\ C_\kappa^{boil} &= 1.725 \times 10^{-5}.\end{aligned}$$

The initial conditions for this problem are

$$\rho_0(\mathbf{x}) = 0.3660 - 0.2971 \tanh\left(\frac{x_2 - 0.35}{2}\sqrt{\mathrm{We}}\right), \tag{184}$$

$$\mathbf{u}_0(\mathbf{x}) = \mathbf{0}, \tag{185}$$

$$\theta_0(\mathbf{x}) = 0.775. \tag{186}$$

In Figure 21, the initial conditions for density and temperature have been illustrated. The perturbation for the temperature on the boundary $\delta_{Y_{5,h}}(\mathbf{x})$ and $\delta_{Y_{5,c}}(\mathbf{x})$ are uniform random distributions and satisfy

$$\begin{aligned}\delta_{Y_{5,h}}(\mathbf{x}) &\in [-5.0 \times 10^{-2}, 5.0 \times 10^{-2}],\\ \delta_{Y_{5,c}}(\mathbf{x}) &\in [-5.0 \times 10^{-3}, 5.0 \times 10^{-3}].\end{aligned}$$

The spatial mesh consists of 2048 × 1024 quadratic NURBS elements. The problem is integrated up to the final time $T = 1.0 \times 10^2$ with time step fixed as $\Delta t = 5.0 \times 10^{-4}$.

In Figures 22-26, snapshots of the density, temperature, and velocity streamlines are depicted. In Figure 22, it can be observed that tiny vapor bubbles are generated at discrete sites of the heated wall surface during the initial times. These small bubbles grow in size, and some bubbles merge together to form larger bubbles, as is shown in Figure 23. The increase of bubble size leads to the increase of buoyancy. Beyond a certain critical point, the bubbles get detached from the bottom boundary and rise upward. At about $t = 18.75$, the first three bubbles get detached from the bottom. More bubbles are generated on the bottom surface in the mean time. Figures 24 and 25 show the moments when two bubbles are about to reach the free surface. Interestingly, from Figures 25 and 26, small droplets can be observed as a result of the breakage of the liquid film when the vapor bubbles reach the free surface. There are 30 bubbles formed in the time interval of $0 < t < 100$.

5.3.3 Two-dimensional film boiling

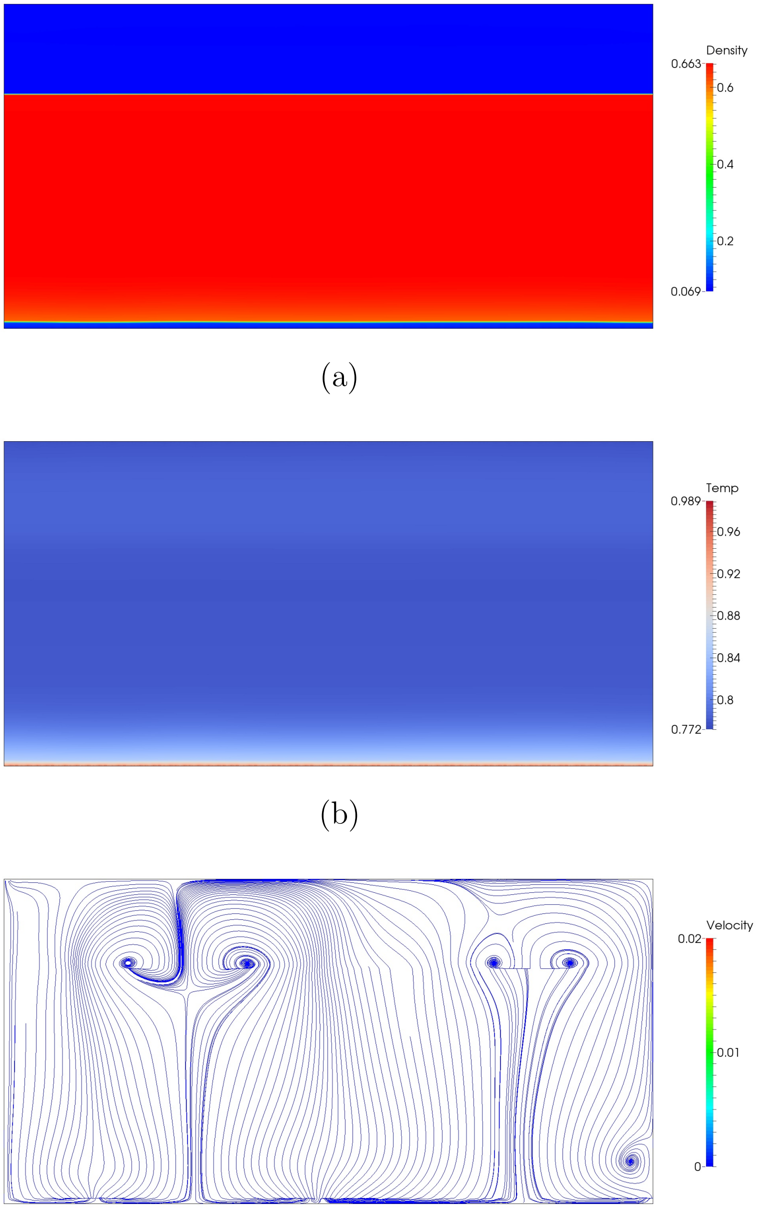

(a)

(b)

(c)

Figure 27: Solutions of the two-dimensional film boiling simulation at $t = 100.0$: (a) density, (b) temperature, (c) velocity streamlines.

In the third example, the same two-dimensional problem considered in the preceding section is simulated again with a different parameter C_μ^{boil}. Here, the parameter C_μ^{boil} is chosen to be 4.600×10^{-4}, which is four times larger than that of the previous example. Since the fluid motion in this example is slower, the simulation is integrated in time up

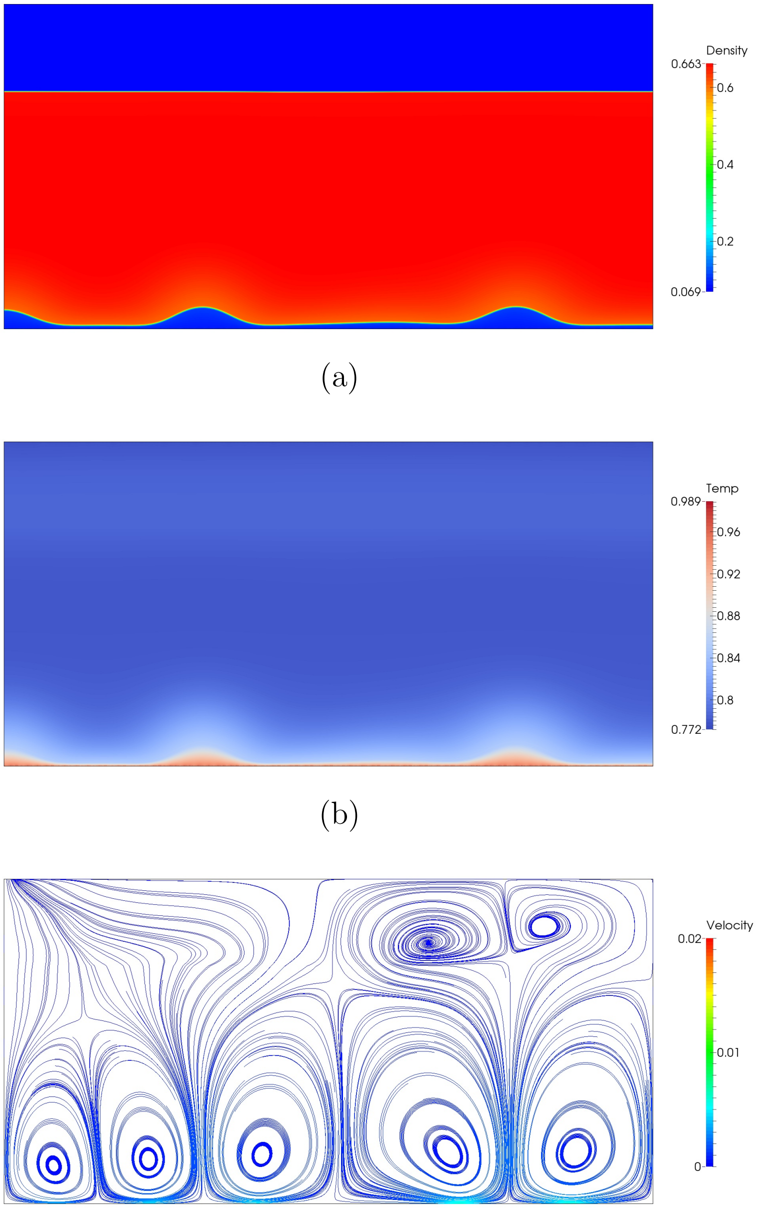

(a)

(b)

(c)

Figure 28: Solutions of the two-dimensional film boiling simulation at $t = 175.0$: (a) density, (b) temperature, (c) velocity streamlines.

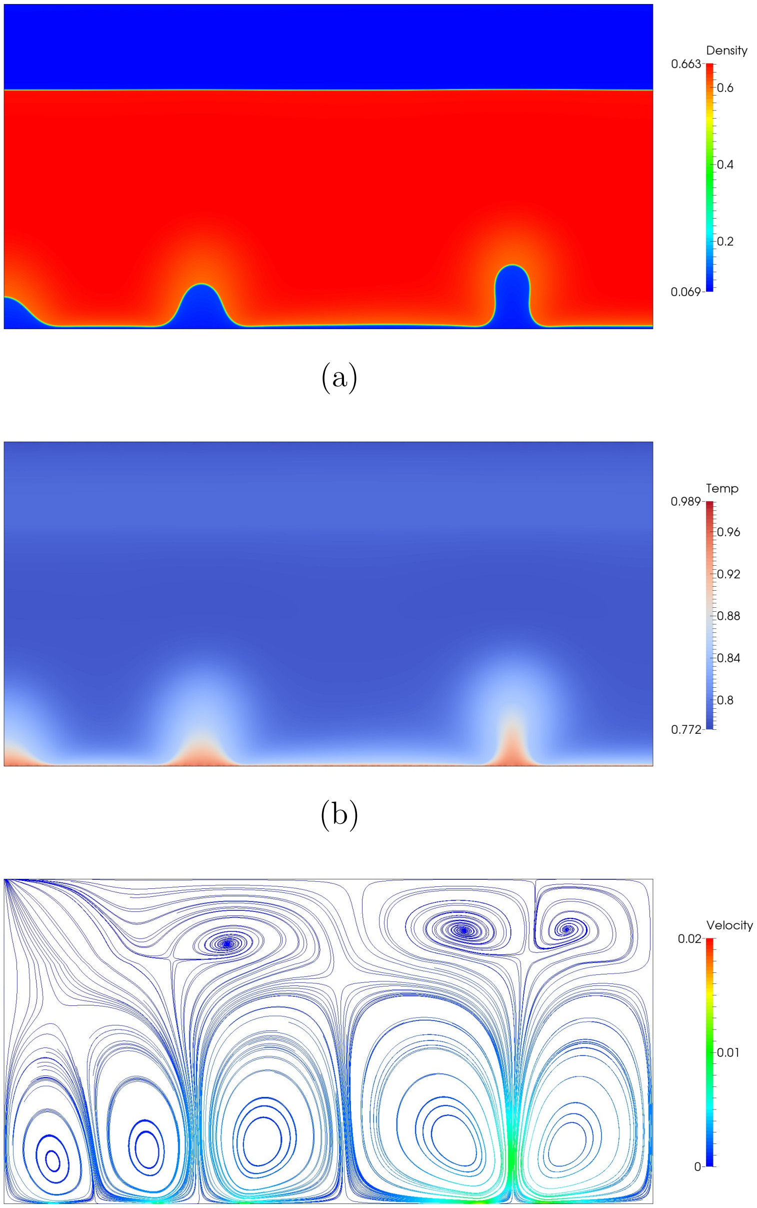

(a)

(b)

(c)

Figure 29: Solutions of the two-dimensional film boiling simulation at $t = 200.0$: (a) density, (b) temperature, (c) velocity streamlines.

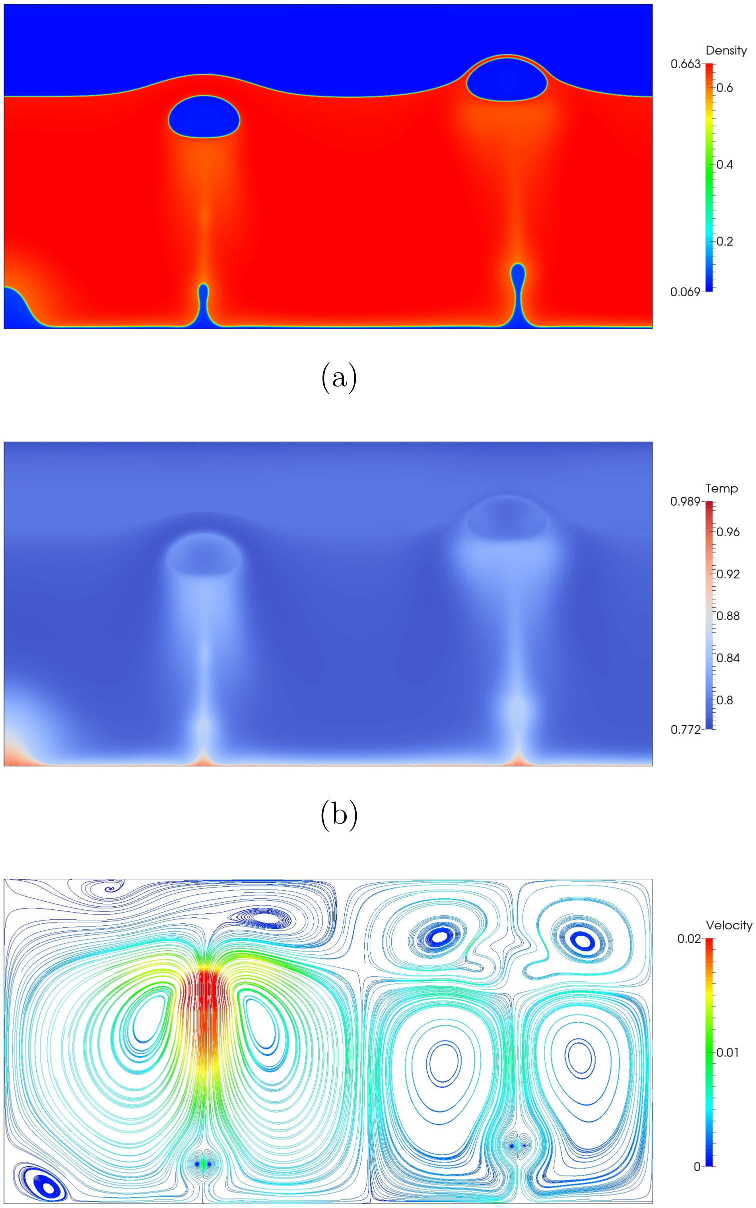

(a)

(b)

(c)

Figure 30: Solutions of the two-dimensional film boiling simulation at $t = 225.0$: (a) density, (b) temperature, (c) velocity streamlines.

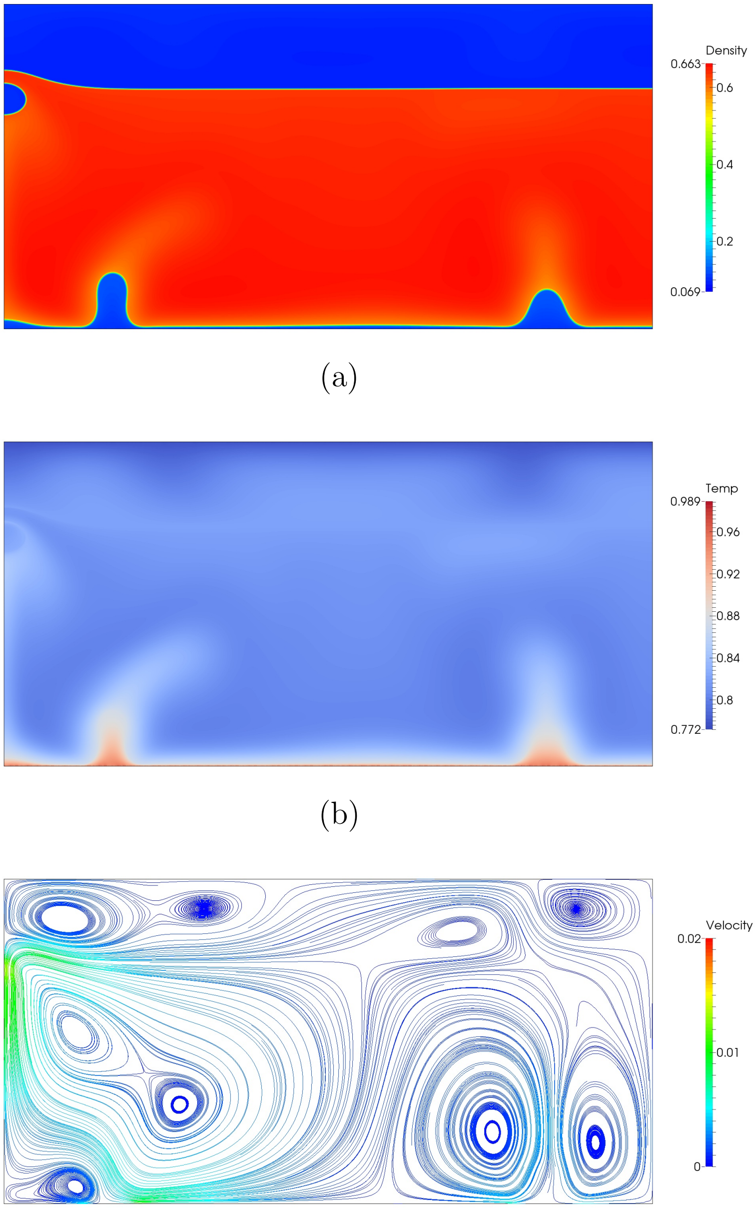

(a)

(b)

(c)

Figure 31: Solutions of the two-dimensional film boiling simulation at $t = 500.0$: (a) density, (b) temperature, (c) velocity streamlines.

to $T = 5.0 \times 10^2$. All the other conditions are identical to those of the previous case. In Figures 27-31, snapshots of the density, temperature, and velocity streamlines at different time steps are presented. Once the simulation starts, a thin vapor film is gradually generated at the bottom during the early stage of the simulation (see Figure 27). As time evolves, the interface becomes unstable and there are mushroom-shaped vapor bubbles formed, as are shown in Figures 28 and 29. From $t = 200.0$ to $t = 225.0$, the first two vapor bubbles pinch off from the vapor film and rise upward in ellipsoidal shapes. As the bubbles get released from the vapor film, two stems are left on the vapor film, which serve as onsets of new bubbles. This process repeats itself periodically. Till the final time $t = 500.0$, there are totally seven bubbles detached from the vapor film. The average bubble release rate for this film boiling problem is much less than that of the nucleate boiling counterpart.

5.3.4 Three-dimensional boiling

As the last example, we simulate the Navier-Stokes-Korteweg equations in a three-dimensional domain $\Omega = (0,1) \times (0,0.5) \times (0,0.25)$. The material properties are chosen as

$$\begin{aligned} \mathrm{We} &= 6.533 \times 10^5, \\ \gamma &= 1.333, \\ C_\mu^{boil} &= 1.289 \times 10^{-4}, \\ C_\kappa^{boil} &= 7.732 \times 10^{-5}. \end{aligned}$$

The initial conditions for this three-dimensional problem are similar to those of the two-dimensional problem, except the free surface is defined by $x_3 = 0.15$:

$$\begin{aligned} \rho_0(\mathbf{x}) &= 0.33565 - 0.26675 \tanh\left(\frac{x_3 - 0.15}{2}\sqrt{\mathrm{We}}\right), \\ \mathbf{u}_0(\mathbf{x}) &= \mathbf{0}, \\ Y_{5,0}(\mathbf{x}) &= -1.2334 - 0.0569 \tanh\left(\frac{x_3 - 0.15}{2}\sqrt{\mathrm{We}}\right). \end{aligned}$$

The perturbation for the temperature on the boundary $\delta_{Y_{5,h}}(\mathbf{x})$ and $\delta_{Y_{5,c}}(\mathbf{x})$ are uniform random distributions and satisfy

$$\begin{aligned} \delta_{Y_{5,h}}(\mathbf{x}) &\in [-5.0 \times 10^{-2}, 5.0 \times 10^{-2}], \\ \delta_{Y_{5,c}}(\mathbf{x}) &\in [-5.0 \times 10^{-3}, 5.0 \times 10^{-3}]. \end{aligned}$$

The spatial mesh consists of $600 \times 300 \times 150$ quadratic NURBS elements. The problem is integrated in time up to $T = 20.0$ with a fixed time step size $\Delta t = 2.0 \times 10^{-3}$.

Remark 18. *The initial condition for* Y_5 *is in fact a hyperbolic tangent interpolation of* $\theta = 0.85$ *for* $x_2 < 0.15$ *and* $\theta = 0.775$ *for* $x_2 > 0.15$.

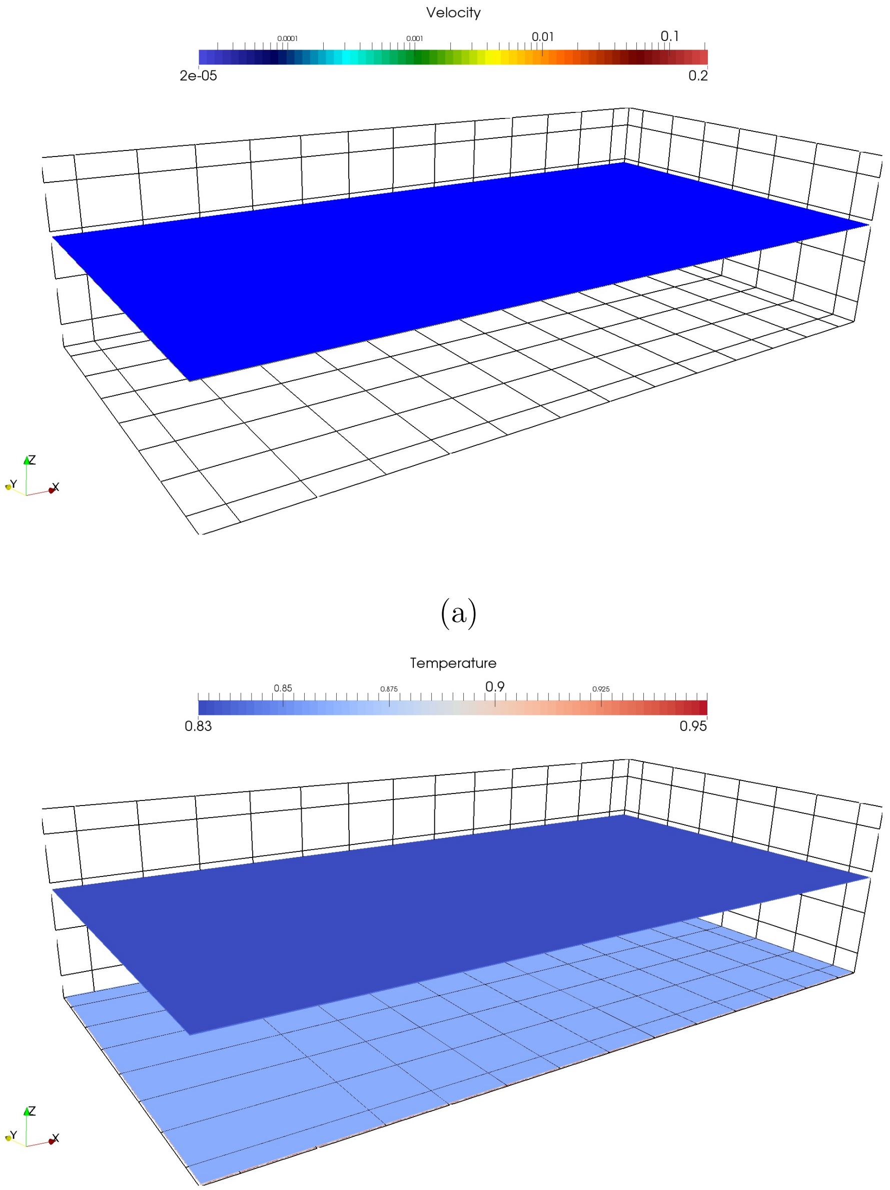

(a)

(b)

Figure 32: Initial conditions of the three-dimensional boiling: (a) density isosurfaces, (b) temperature isosurfaces.

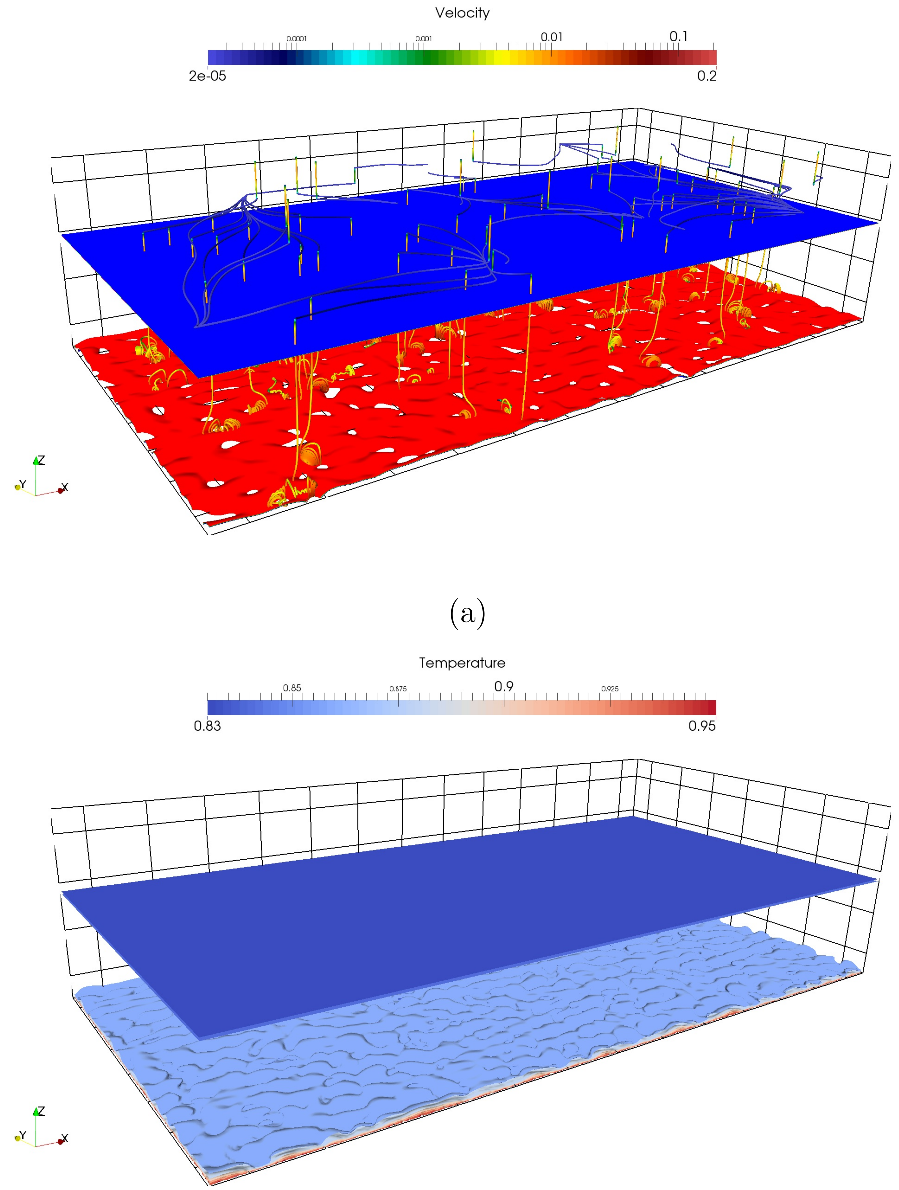

(a)

(b)

Figure 33: Solutions of the three-dimensional boiling at time $t = 0.6$: (a) density isosurfaces and velocity streamlines, (b) temperature isosurfaces.

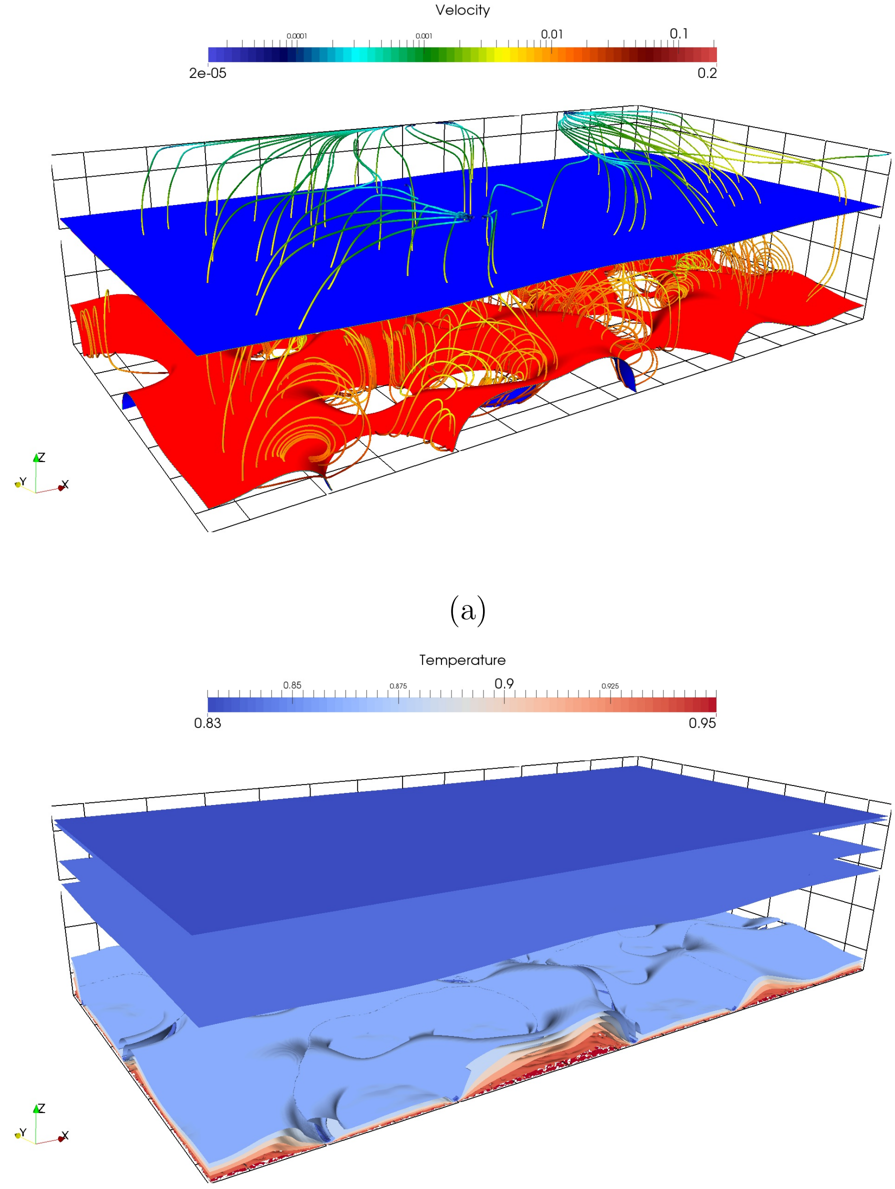

(a)

(b)

Figure 34: Solutions of the three-dimensional boiling at time $t = 5.0$: (a) density isosurfaces and velocity streamlines, (b) temperature isosurfaces.

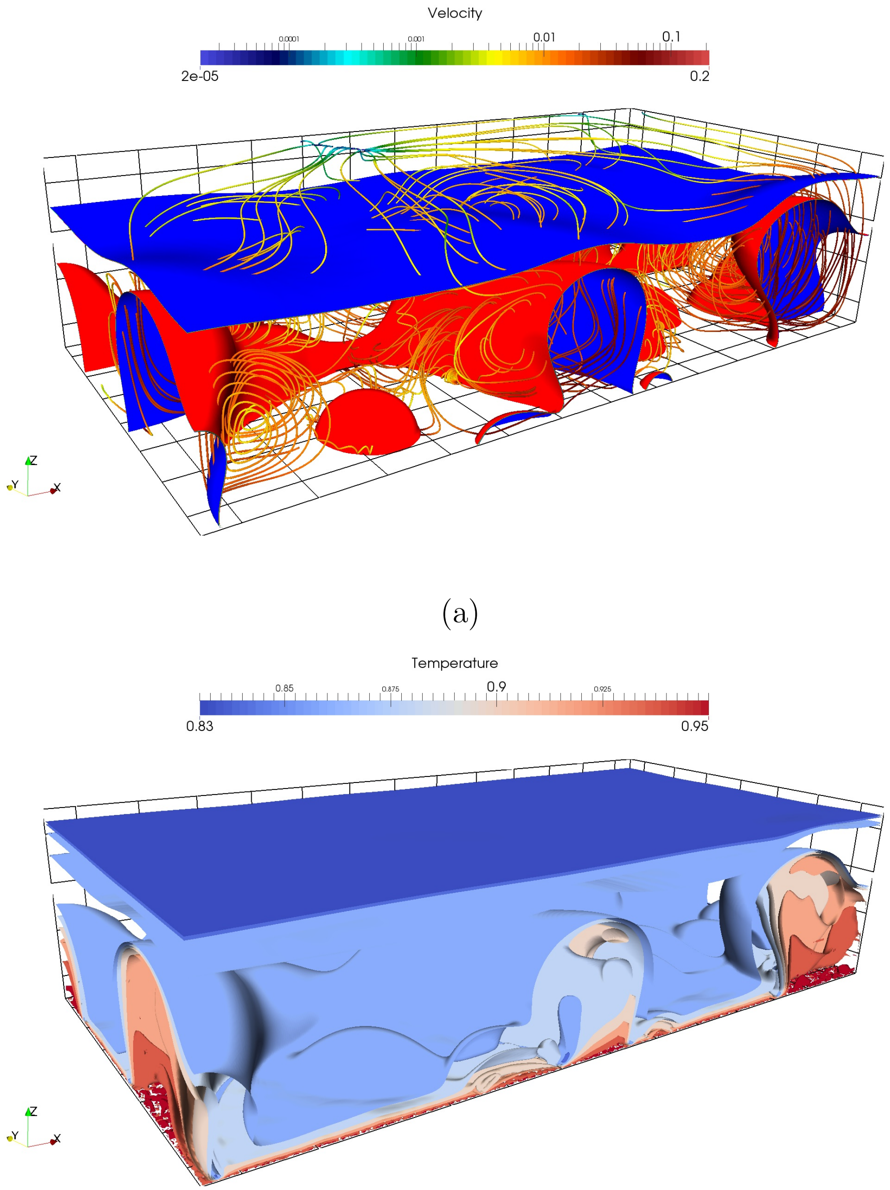

(a)

(b)

Figure 35: Solutions of the three-dimensional boiling at time $t = 11.0$: (a) density isosurfaces and velocity streamlines, (b) temperature isosurfaces.

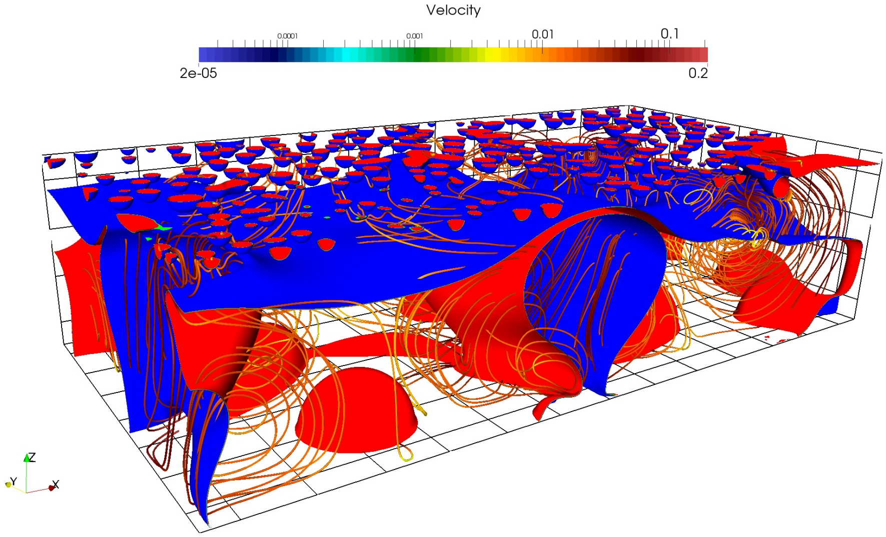

(a)

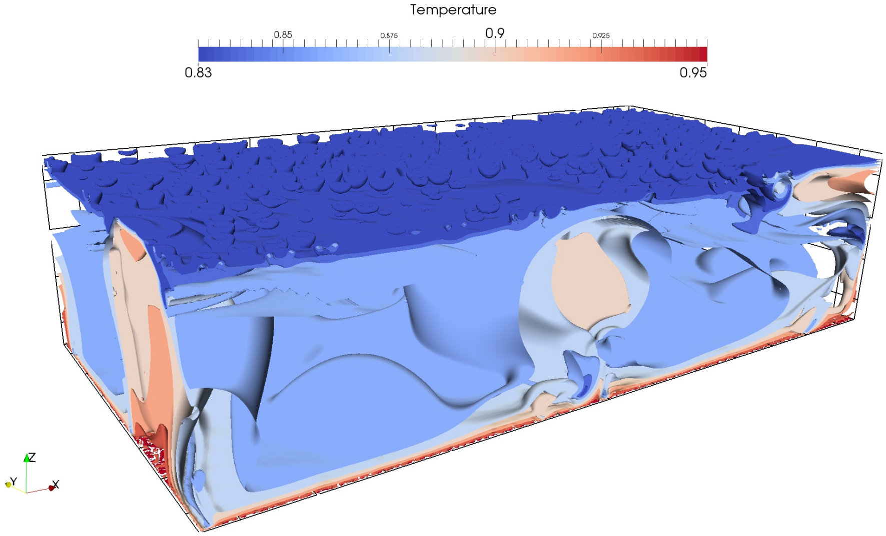

(b)

Figure 36: Solutions of the three-dimensional boiling at time $t = 14.0$: (a) density isosurfaces and velocity streamlines, (b) temperature isosurfaces.

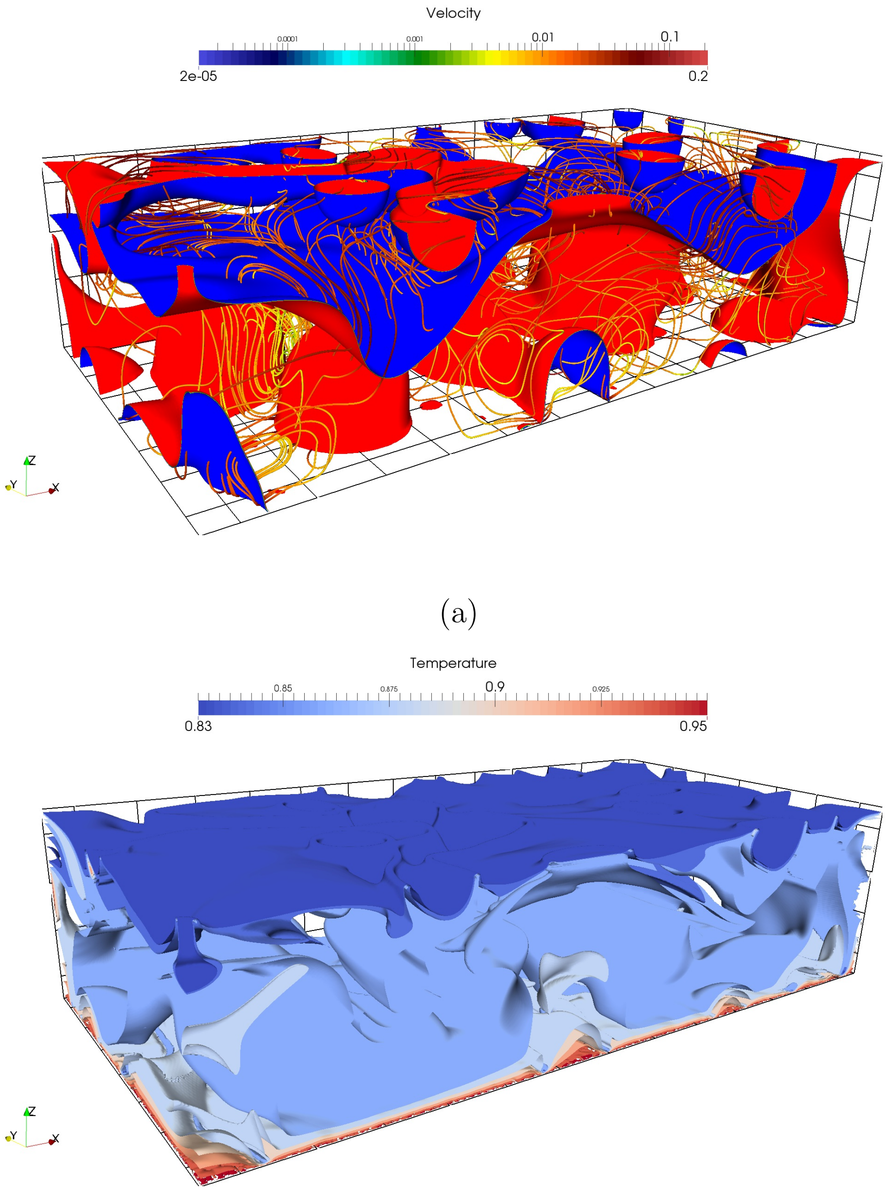

(a)

(b)

Figure 37: Solutions of the three-dimensional boiling at time $t = 20.0$: (a) density isosurfaces and velocity streamlines, (b) temperature isosurfaces.

In Figures 32-37, snapshots of density isosurfaces, velocity streamlines, and temperature isosurfaces are presented at times $t = 0.0$, 0.6, 5.0, 11.0, 14.0 and 20.0. At the initial stage, there is an unstable vapor film formed over the heated wall surface (see Figure 33). This film soon separates into isolated vapor bubbles located at random sites on the bottom surface (see Figures 34 and 35). With the growth of the bubbles, the thermal energy is conducted through the vapor region. Since the simulation domain is very shallow in the vertical direction, these bubbles reach the free surface before they get fully detached from the bottom. When these high-temperature vapor bubbles reach the cooled top surface, they condense into liquid droplets instantaneously (see Figure 36). At $t = 20.0$, a second round of vapor bubbles is clearly generated on the bottom and the liquid droplets on the top surface get merged together. There is a complex Rayleigh-Bénard mixing structure for the temperature field, as is shown in Figure 37.

6 Conclusions and future work

In this work, we presented a comprehensive suite of theoretical and numerical methodologies for the study of liquid-vapor two-phase flows. The contributions are elaborated as follows.

A continuum mechanic modeling framework for multiphase flows has been constructed. In its derivation, the microforce theory [27] is adopted with the objective of accommodating non-local effects. This modeling framework enjoys several appealing properties. First, all constitutive relations are represented in terms of a thermodynamic potential. Therefore, the modeling work is reduced to the design of a proper form of the thermodynamic potential. Second, the framework automatically satisfies the second law of thermodynamics. Third, some previously mysterious modeling terms find rational mechanics explanations as a result of the Coleman-Noll procedure. For example, the "interstitial working flux" [17] is the power expenditure of the microstress. Within this framework, the Navier-Stokes-Korteweg equations and the compressible Navier-Stokes equations are recovered by proper choices of the Helmholtz free energy functional.

A thermodynamically consistent numerical scheme for the Navier-Stokes-Korteweg equations is constructed. For the van der Waals fluid model, the definition of entropy variables is generalized to the functional setting to overcome the difficulty induced by the non-convexity of the entropy function. Interestingly, the functional entropy variables for the van der Waals fluid are formally identical to those of the perfect gas model. The difference is that the entropy variables are not obtainable by merely an algebraic change-of-variables, but rather they are mappings from the conservation variables to their dual spaces. In the strong form, in order to obtain conservation variables from the entropy variables, one need to solve a partial differential equation. An alternative statement of the strong form problem is devised such that the equation for the entropy variable conjugate to density is weakly enforced. In doing so, the weak problem is guaranteed to be entropy dissipative, as is shown in Theorem 4. In addition to the spatial discretization, new time integration schemes are developed based on a family of new quadrature rules [44]. In contrast to the traditional temporal schemes [63], the new time integration schemes do not require convexity of the entropy function. Essentially, the new schemes can be viewed as second-order modifications to the mid-point rule. The modifications are designed so that the temporal approximation is provably entropy dissipative. The theoretical convergence estimates have been numerically verified by comparing solutions with manufactured solutions and overkill solutions.

The new model and the new algorithm have been applied to investigate a variety of problems, including evaporation, condensation, bubble motion under a temperature gradient, and nucleate and film boiling. The advantage of the diffuse-interface method is demonstrated by the two and three-dimensional boiling simulations. Our approach enjoys several desirable properties. First, the dependency on empirical knowledge and assumptions are significantly reduced. In contrast, existing boiling models rely heavily on empirical data and sometimes introduce artificial modeling terms. Second, our approach provides a unified modeling framework for both nucleate boiling and film boiling. We believe our methodology may provide a predictive tool for a wide spectrum of the boiling phenomena.

There are several promising research directions for future work. The Navier-Stokes-Korteweg equations are believed to be applicable to simulating cavitating flows, the liquid-vapor phase transition induced by pressure variations. A potential challenge for such a simulation is a proper design of open boundary conditions. The van der Waals model can be further improved to give more accurate material descriptions. Recently, new models have been introduced [62], and we anticipate that applying these new equation-of-state may lead to better results in comparison with the van der Waals model. On the computation side, the anisotropic structure of the solutions makes mesh-adaptive isogeometric analysis techniques [57, 60] highly desirable.

Acknowledgements

This work was partially supported by the Office of Naval Research under contract number N00014-08-1-0992. Ju Liu was partially supported by the National Initiative for Modeling and Simulation (NIMS) fellowship. Hector Gomez was partially supported by the J. Tinsley Oden Faculty Fellowship Research Program at the Institute for Computational Engineering and Sciences, by the European Research Council through the FP7 Ideas Starting Grant

Program (Contract # 307201), and by Ministerio de Economía y Competitividad (Contract # DPI-2013-44406-R).

The authors also acknowledge the Texas Advanced Computing Center (TACC) at The University of Texas at Austin for providing HPC, visualization, and data storage resources that have contributed to the obtained research results reported within this paper.

References

[1] L.K. Antanovskii. A phase field model of capillarity. *Physics of Fluids*, 7:747–753, 1995.

[2] A. Badillo. Quantitative phase-field modeling for boiling phenomena. *Physical Review E*, 86:041603, 2012.

[3] T. Barth. On the role of involutions in the discontinuous galerkin discretization of maxwell and magnetohydrodynamic systems. In *Compatible spatial discretizations*, pages 69–88. Springer New York, 2006.

[4] Y. Bazilevs, V.M. Calo, J.A. Cottrell, J.A. Evans, T.J.R. Hughes, S. Lipton, M.A. Scott, and T.W. Sederberg. Isogeometric analysis using T-splines. *Computer Methods in Applied Mechanics and Engineering*, 199:229–263, 2010.

[5] Y. Bazilevs and T.J.R. Hughes. Weak imposition of Dirichlet boundary conditions in fluid mechanics. *Computers & Fluids*, 36:12–26, 2007.

[6] J.A. Beattie and O.C. Bridgeman. A New Equation of State for Fluids. I. Application to Gaseous Ethyl Ether and Carbon Dioxide. *Journal of the American Chemical Society*, 49:1665–1667, 1927.

[7] M. Benedict, G.B. Webb, and L.C. Rubin. An Empirical Equation for Thermodynamic Properties of Light Hydrocarbons and Their Mixtures I. Methane, Ethane, Propane and n-Butane. *Journal of Chemical Physics*, 8:334–345, 1940.

[8] S.W. Bova and G.F. Carey. An entropy variable formulation and applications for the two-dimensional shallow water equations. *International Journal for Numerical Methods in Fluids*, 23:29–46, 1996.

[9] J.W. Cahn and J.E. Hilliard. Free energy of a non-uniform system. I. Interfacial free energy. *The Journal of Chemical Physics*, 28:258–267, 1958.

[10] F. Chalot, T.J.R. Hughes, and F. Shakib. Symmetrization of conservation laws with entropy for high-temperature hypersonic computations. *Computing Systems in Engineering*, 1:495–521, 1990.

[11] B.D. Coleman and W. Noll. The thermodynamics of elastic materials with heat conduction and viscosity. *Archive for Rational Mechanics and Analysis*, 13:167–178, 1963.

[12] J.A. Cottrell, T.J.R. Hughes, and Y. Bazilevs. *Isogeometric Analysis: Toward Integration of CAD and FEA*. Wiley, 2009.

[13] L. Dedè, M.J. Borden, and T.J.R. Hughes. Isogeometric analysis for topology optimization with a phase field model. *Archives of Computational Methods in Engineering*, 19:1–39, 2012.

[14] L. Dedè, C. Jäggli, and A. Quarteroni. Isogeometric numerical dispersion analysis for two-dimensional elastic wave propagation. *Computer Methods in Applied Mechanics and Engineering*, 284:320–348, 2015.

[15] V.K. Dhir. Boiling heat transfer. *Annual Review of Fluid Mechanics*, 30:365–401, 1998.

[16] V.K. Dhir, G.R. Warrier, and E. Aktinol. Numerical Simulation of Pool Boiling: A Review. *Journal of Heat Transfer*, 135:1–17, 2013.

[17] J.E. Dunn and J. Serrin. On the thermomechanics of interstitial working. *Archive for Rational Mechanics and Analysis*, 88:95–133, 1985.

[18] J.A. Evans, Y. Bazilevs, I. Babuska, and T.J.R. Hughes. n-widths, sup-infs and optimality ratios for the k-version of the isogeometric finite element method. *Computer Methods in Applied Mechanics and Engineering*, 198:1726–1741, 2009.

[19] J.A. Evans and T.J.R. Hughes. Isogeometric divergence-conforming B-splines for the Darcy-Stokes-Brinkman equations. *Mathematical Models and Methods in Applied Sciences*, 23:671–741, 2013.

[20] J.A. Evans and T.J.R. Hughes. Isogeometric divergence-conforming B-splines for the steady Navier-Stokes equations. *Mathematical Models and Methods in Applied Sciences*, 23:1421–1478, 2013.

[21] J.A. Evans and T.J.R. Hughes. Isogeometric divergence-conforming B-splines for the unsteady Navier-Stokes equations. *Journal of Computational Physics*, 241:141–167, 2013.

[22] H. Gomez, V.M. Calo, Y. Bazilevs, and T.J.R. Hughes. Isogeometric analysis of the Cahn-Hilliard phase-field model. *Computer Methods in Applied Mechanics and Engineering*, 197:4333–4352, 2008.

[23] H. Gomez, L. Cueto-Felgueroso, and R. Juanes. Three-dimensional simulation of unstable gravity-driven infiltration of water into a porous medium. *Journal of Computational Physics*, 238:217–239, 2013.

[24] H. Gomez and T.J.R. Hughes. Provably unconditionally stable, second-order time-accurate, mixed variational methods for phase-field models. *Journal of Computational Physics*, 230(13):5310–5327, 2011.

[25] H. Gomez, T.J.R. Hughes, X. Nogueira, and V.M. Calo. Isogeometric anslysis of the isothermal Navier-Stokes-Korteweg equations. *Computer Methods in Applied Mechanics and Engineering*, 199:1828–1840, 2010.

[26] H. Gomez, A. Reali, and G. Sangalli. Accurate, efficient, and (iso) geometrically flexible collocation methods for phase-field models. *Journal of Computational Physics*, 262:153–171, 2014.

[27] M.E. Gurtin. Generalized Ginzburg-Landau and Cahn-Hilliard equations based on a microforce balance. *Physica D: Nonlinear Phenomena*, 92:178–192, 1996.

[28] M.E. Gurtin. On the plasticity of single crystals: free energy, microforces, plastic-strain gradients. *Journal of the Mechanics and Physics of Solids*, 48:898–1036, 2000.

[29] M.E. Gurtin, E. Fried, and L. Anand. *The Mechanics and Thermodynamics of Continua.* Cambridge University Press, 2009.

[30] H. Haj-Hariri, Q. Shi, and A. Borhan. Thermocapillary motion of deformable drops at finite Reynolds and Marangoni numbers. *Physics of Fluids*, 9:845–855, 1997.

[31] C.W. Hirt and B.D. Nichols. Volume of fluid (VOF) method for the dynamics of free boundaries. *Journal of Computational Physics*, 39:201–225, 1981.

[32] T.J.R. Hughes. *The Finite Element Method: Linear Static and Dynamic Finite Element Analysis.* Prentice Hall, Englewood Cliffs, NJ, 1987.

[33] T.J.R. Hughes, J.A. Cottrell, and Y. Bazilevs. Isogeometric analysis: CAD, finite elements, NURBS, exact geometry and mesh refinement. *Computer Methods in Applied Mechanics and Engineering*, 194:4135–4195, 2005.

[34] T.J.R. Hughes, L.P. Franca, and M. Mallet. A new finite element formulation for computational fluid dynamics: I. Symmetric forms of the compressible Euler and Navier-Stokes equations and the second law of thermodynamics. *Computer Methods in Applied Mechanics and Engineering*, 54(2):223–234, 1986.

[35] T.J.R. Hughes, G. Scovazzi, and T.E. Tezduyar. Stabilized Methods for Compressible Flows. *Journal of Scientific Computing*, 43:343–368, 2010.

[36] D. Jamet, D. Torres, and J.U. Brackbill. On the theory and computation of surface tension: The elimination of parasitic currents through energy conservation in the second-gradient method. *Journal of Computational Physics*, 182:262–276, 2002.

[37] D. Jasnow and J. Vinals. Coarse-grained description of thermo-capillary flow. *Physics of Fluids*, 8:660–669, 1996.

[38] D. Juric and G. Tryggvason. Computations of boiling flows. *International Journal of Multiphase Flow*, 24:387–410, 1998.

[39] D.J. Korteweg. Sur la forme que prennent les équations du mouvement des fluides si l'on tient compte des forces capillaires causées par des variations de densité considérables mais continues et sur la théorie de la capillarité dans l'hypothèse d'une variation continue de la densité. *Arch. Néerl.*, 6(2):1–24, 1901.

[40] G. Kuiper. *Cavitation inception on ship propeller models*. PhD thesis, Delft University of Technology, 1981.

[41] S. Lipton, J.A. Evans, Y. Bazilevs, T. Elguedj, and T.J.R. Hughes. Robustness of isogeometric structural discretizations under severe mesh distortion. *Computer Methods in Applied Mechanics and Engineering*, 199:357–373, 2010.

[42] J. Liu. *Thermodynamically Consistent Modeling and Simulation of Multiphase Flows*. PhD thesis, The University of Texas at Austin, 2014.

[43] J. Liu, L. Dedè, J.A. Evans, M.J. Borden, and T.J.R. Hughes. Isogeometric Analysis of the Advective Cahn-Hilliard Equation: Spinodal Decomposition Under Shear Flow. *Journal of Computational Physics*, 242:321–350, 2013.

[44] J. Liu, H. Gomez, J.A. Evans, T.J.R. Hughes, and C.M. Landis. Functional Entropy Variables: A New Methodology for Deriving Thermodynamically Consistent Algorithms for Complex Fluids, with Particular Reference to the Isothermal Navier-Stokes-Korteweg Equations. *Journal of Computational Physics*, 248:47–86, 2013.

[45] J. Lowengrub and L. Truskinovsky. Quasi-incompressible Cahn-Hilliard fluids and topological transitions. *Proceedings of the Royal Society A*, 454:2617–2654, 1998.

[46] M. Maraldi, G.N. Wells, and L. Molari. Phase field model for coupled displacive and diffusive microstructural processes under thermal loading. *Journal of the Mechanics and Physics of Solids*, 59:1596–1612, 2011.

[47] J.E. Marsden and T.J.R. Hughes. *Mathematical foundations of elasticity*. Dover, New York, 1994.

[48] J.L. McGrew, F.L. Bamford, and T.R. Rehm. Marangoni Flow: An Additional Mechanism in Boiling Heat Transfer. *Science*, 153:1106–1107, 1966.

[49] K.C. Mills, B.J. Keene, R.F. Brooks, and A. Shirali. Marangoni effects in welding. *Philosophical Transactions of the Royal Society of London A*, 356:911–925, 1998.

[50] National Institute of Standards and Technology. Thermophysical Properties of Fluid Systems. http://webbook.nist.gov/chemistry/fluid/, 2012. [Online; accessed 15-July-2012].

[51] A. Onuki. Dynamic van der Waals Theory of Two-Phase Fluids in Heat Flow. *Physical Review Letters*, 94:054501, 2005.

[52] A. Onuki. Dynamic van der Waals theory. *Physical Review E*, 75:036304, 2007.

[53] A. Onuki and K. Kanatani. Droplet motion with phase change in a temperature gradient. *Physical Review E*, 72:066304, 2005.

[54] S. Osher and J.A. Sethian. Fronts propagating with curvature-dependent speed: Algorithms based on Hamilton-Jacobi formulations. *Journal of Computational Physics*, 79:12–49, 1988.

[55] W.M. Rohsenow. Boiling. *Annual Review of Fluid Mechanics*, 3:211–236, 1971.

[56] D. Schillinger, M.J. Borden, and H.K. Stolarski. Isogeometric collocation for phase-field fracture models. *Computer Methods in Applied Mechanics and Engineering*, 284:583–610, 2015.

[57] D. Schillinger, L. Dedè, M.A. Scott, J.A. Evans, M.J. Borden, E. Rank, and T.J.R. Hughes. An isogeometric design-through-analysis methodology based on adaptive hierarchical refinement of NURBS, immersed boundary methods, and T-spline CAD surfaces. *Computer Methods in Applied Mechanics and Engineering*, 249-252:116–150, 2012.

[58] D. Schillinger, J.A. Evans, A. Reali, M.A. Scott, and T.J.R. Hughes. Isogeometric collocation: Cost comparison with Galerkin methods and extension to adaptive hierarchical NURBS discretizations. *Computer Methods in Applied Mechanics and Engineering*, 267:170–232, 2013.

[59] Daniel V. Schroeder. *An introduction to thermal physics.* Robin J. Heyden, 2000.

[60] M.A. Scott, X Li, T.W. Sederberg, and T.J.R. Hughes. Local refinement of analysis-suitable T-splines. *Computer Methods in Applied Mechanics and Engineering*, 213:206–222, 2012.

[61] L.E. Scriven and C.V. Sternling. The Marangoni effects. *Nature*, 187:186–188, 1960.

[62] J. Serrin. The Area Rule for Simple Fluid Phase Transitions. *Journal of Elasticity*, 90:129–159, 2008.

[63] F. Shakib, T.J.R. Hughes, and Z. Johan. A new finite element formulation for computational fluid dynamics: X. The compressible Euler and Navier-Stokes equations. *Computer Methods in Applied Mechanics and Engineering*, 89:141–219, 1991.

[64] G. Son and V.K. Dhir. Numerical Simulation of Saturated Film Boiling on a Horizontal Surface. *Journal of Heat Transfer*, 119:525–533, 1997.

[65] G. Son and V.K. Dhir. Numerical simulation of nucleate boiling on a horizontal surface at high heat fluxes. *International Journal of Heat and Mass Transfer*, 51:2566–2582, 2008.

[66] Y. Su and C.M. Landis. Continuum Thermodynamics of Ferroelectric Domain Evolution: Theory, Finite Element Implementation, and Application to Domain Wall Pinning. *Journal of the Mechanics and Physics of Solids*, 55:280–305, 2007.

[67] C. Truesdell and W. Noll. *The Non-Linear Field Theories of Mechanics.* Springer, 1965.

[68] G. Tryggvason, B. Bunner, A. Esmaeeli, D. Juric, N. Al-Rawahi, W. Tauber, J. Han, S. Nas, and Y.J. Jan. A Front-Tracking Method for the Computations of Multiphase Flow. *Journal of Computational Physics*, 169:708–759, 2001.

[69] J.D. van der Waals. The thermodynamic theory of capillarity under the hypothesis of a continuous variation of density. *Journal of Statistical Physics*, 20:200–244, 1979.

[70] G. Vilanova, I. Colominas, and H. Gomez. Coupling of discrete random walks and continuous modeling for three-dimensional tumor-induced angiogenesis. *Computational Mechanics*, 53:449–464, 2014.

[71] S.W.J. Welch and J. Wilson. A Volume of Fluid Based Method for Fluid Flows with Phase Change. *Journal of Computational Physics*, 160:662–682, 2000.

[72] Z.A Wilson, M.J. Borden, and C.M. Landis. A phase-field model for fracture in piezoelectric ceramics. *International Journal of Fracture*, 183:135–153, 2013.

[73] N.O. Young, J.S. Goldstein, and M.J. Block. The motion of bubbles in a vertical temperature gradient. *Journal of Fluid Mechanics*, 6:350–356, 1959.